

REPORT DOCUMENTATION PAGE			Form Approved OMB No. 0704-0188	
<small>Public reporting burden for this collection of information is estimated to average 1 hour per response, including the time for reviewing instructions, searching existing data sources, gathering and maintaining the data needed, and completing and reviewing the collection of information. Send comments regarding this burden estimate or any other aspect of this collection of information, including suggestions for reducing this burden, to Washington Headquarters Services, Directorate for Information Operations and Reports, 1215 Jefferson Davis Highway, Suite 1204, Arlington, VA 22202-4302, and to the Office of Management and Budget, Paperwork Reduction Project (0704-0188), Washington, DC 20503.</small>				
1. AGENCY USE ONLY (Leave blank)		2. REPORT DATE 6.Dec.00		3. REPORT TYPE AND DATES COVERED THESIS
4. TITLE AND SUBTITLE REAL TIME, AUTONOMOUS,PRECISE ORBIT DETERMINATION USING THE GLOBAL POSTIONING SYSTEM			5. FUNDING NUMBERS	
6. AUTHOR(S) MAJ GOLDSTEIN DAVID B				
7. PERFORMING ORGANIZATION NAME(S) AND ADDRESS(ES) UNIVERSITY OF COLORADO AT BOULDER			8. PERFORMING ORGANIZATION REPORT NUMBER CY00462	
9. SPONSORING/MONITORING AGENCY NAME(S) AND ADDRESS(ES) THE DEPARTMENT OF THE AIR FORCE AFIT/CIA, BLDG 125 2950 P STREET WPAFB OH 45433			10. SPONSORING/MONITORING AGENCY REPORT NUMBER	
11. SUPPLEMENTARY NOTES				
12a. DISTRIBUTION AVAILABILITY STATEMENT Unlimited distribution In Accordance With AFI 35-205/AFIT Sup 1			12b. DISTRIBUTION CODE	
13. ABSTRACT (Maximum 200 words)				
14. SUBJECT TERMS			15. NUMBER OF PAGES 188	
			16. PRICE CODE	
17. SECURITY CLASSIFICATION OF REPORT		18. SECURITY CLASSIFICATION OF THIS PAGE		19. SECURITY CLASSIFICATION OF ABSTRACT
				20. LIMITATION OF ABSTRACT

Goldstein, David Ben (Ph.D., Aerospace Engineering Sciences)

Real-time, Autonomous, Precise Satellite Orbit Determination Using the Global Positioning System

Thesis Directed by Professor George H. Born

In an effort to estimate precise satellite ephemeris in real-time on board a satellite, the Goddard Space Flight Center (GSFC) created the GPS Enhanced Orbit Determination Experiment (GEODE) flight navigation software. This dissertation offers alternative methods and improvements to GEODE to increase on board autonomy and real-time total position accuracy and precision without increasing computational burden.

First, GEODE is modified to include a Gravity Acceleration Approximation Function (GAAF) to replace the traditional spherical harmonic representation of the gravity field. Next, an ionospheric correction method called Differenced Range Versus Integrated Doppler (DRVID) is applied to correct for ionospheric errors in the GPS measurements used in GEODE. Then, Dynamic Model Compensation (DMC) is added to estimate unmodeled and/or mismodeled forces in the dynamic model and to provide an alternative process noise variance-covariance formulation. Finally, a Genetic Algorithm (GA) is implemented in the form of Genetic Model Compensation (GMC) to optimize DMC forcing noise parameters.

Application of GAAF, DRVID and DMC improved GEODE's position estimates by 28.3% when applied to GPS/MET data collected in the presence of Selective Availability (SA), 17.5% when SA is removed from the GPS/MET data and 10.8% on SA free TOPEX data. Position estimates with RSS errors below 1 meter are now achieved using SA free TOPEX data. DRVID causes an increase in computational burden while GAAF and DMC reduce computational burden. The net effect of applying GAAF, DRVID and DMC is an improvement in GEODE's accuracy/precision without an increase in computational burden.

DTIC QUALITY INSPECTED 4

20001215 137

Goldstein, David Ben (Ph.D., Aerospace Engineering Sciences)

Real-time, Autonomous, Precise Satellite Orbit Determination Using the Global Positioning System

Thesis Directed by Professor George H. Born

In an effort to estimate precise satellite ephemeris in real-time on board a satellite, the Goddard Space Flight Center (GSFC) created the GPS Enhanced Orbit Determination Experiment (GEODE) flight navigation software. This dissertation offers alternative methods and improvements to GEODE to increase on board autonomy and real-time total position accuracy and precision without increasing computational burden.

First, GEODE is modified to include a Gravity Acceleration Approximation Function (GAAF) to replace the traditional spherical harmonic representation of the gravity field. Next, an ionospheric correction method called Differenced Range Versus Integrated Doppler (DRVID) is applied to correct for ionospheric errors in the GPS measurements used in GEODE. Then, Dynamic Model Compensation (DMC) is added to estimate unmodeled and/or mismodeled forces in the dynamic model and to provide an alternative process noise variance-covariance formulation. Finally, a Genetic Algorithm (GA) is implemented in the form of Genetic Model Compensation (GMC) to optimize DMC forcing noise parameters.

Application of GAAF, DRVID and DMC improved GEODE's position estimates by 28.3% when applied to GPS/MET data collected in the presence of Selective Availability (SA), 17.5% when SA is removed from the GPS/MET data and 10.8% on SA free TOPEX data. Position estimates with RSS errors below 1 meter are now achieved using SA free TOPEX data. DRVID causes an increase in computational burden while GAAF and DMC reduce computational burden. The net effect of applying GAAF, DRVID and DMC is an improvement in GEODE's accuracy/precision without an increase in computational burden.

REAL-TIME, AUTONOMOUS PRECISE
SATELLITE ORBIT DETERMINATION
USING
THE GLOBAL POSITIONING SYSTEM

by

David Ben Goldstein

B.S., United States Air Force Academy, 1988

M.S., University of Houston, 1994

A thesis submitted to the
Faculty of the Graduate School of the
University of Colorado in partial fulfillment
of the requirement for the degree of Doctor of Philosophy
Department of Aerospace Engineering Sciences

2000

This thesis entitled:

Real-time, Autonomous, Precise Satellite Orbit Determination

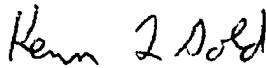
Using the Global Positioning System

written by David Ben Goldstein

has been approved for the Department of Aerospace Engineering Sciences by

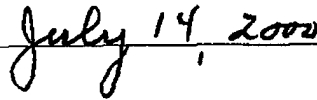


George H. Born, Chairperson of Supervisory Committee



Kenn L. Gold, Second Reader

Date



The signatories have examined the final copy of this thesis, and we find that both the content and the form meet acceptable presentation standards of scholarly work in the above mentioned discipline.

Goldstein, David Ben (Ph.D., Aerospace Engineering Sciences)

Real-time, Autonomous, Precise Satellite Orbit Determination Using the Global Positioning System

Thesis Directed by Professor George H. Born

The desire for autonomously generated, rapidly available, and highly accurate satellite ephemeris is growing with the proliferation of constellations of satellites and the cost and overhead of ground tracking resources. Autonomous Orbit Determination (OD) may be done on the ground in a post-processing mode or in real-time on board a satellite and may be accomplished days, hours or immediately after observations are processed.

The Global Positioning System (GPS) is now widely used as an alternative to ground tracking resources to supply observation data for satellite positioning and navigation. GPS is accurate, inexpensive, provides continuous coverage, and is an excellent choice for autonomous systems. In an effort to estimate precise satellite ephemeris in real-time on board a satellite, the Goddard Space Flight Center (GSFC) created the GPS Enhanced OD Experiment (GEODE) flight navigation software. This dissertation offers alternative methods and improvements to GEODE to increase on board autonomy and real-time total position accuracy and precision without increasing computational burden.

First, GEODE is modified to include a Gravity Acceleration Approximation Function (GAAF) to replace the traditional spherical harmonic representation of the gravity field. Next, an ionospheric correction method called Differenced Range Versus Integrated Doppler (DRVID) is applied to correct for ionospheric errors in the

GPS measurements used in GEODE. Then, Dynamic Model Compensation (DMC) is added to estimate unmodeled and/or mismodeled forces in the dynamic model and to provide an alternative process noise variance-covariance formulation. Finally, a Genetic Algorithm (GA) is implemented in the form of Genetic Model Compensation (GMC) to optimize DMC forcing noise parameters.

Application of GAAF, DRVID and DMC improved GEODE's position estimates by 28.3% when applied to GPS/MET data collected in the presence of Selective Availability (SA), 17.5% when SA is removed from the GPS/MET data and 10.8% on SA free TOPEX data. Position estimates with RSS errors below 1 meter are now achieved using SA free TOPEX data. DRVID causes an increase in computational burden while GAAF and DMC reduce computational burden. The net effect of applying GAAF, DRVID and DMC is an improvement in GEODE's accuracy/precision without an increase in computational burden.

ACKNOWLEDGMENTS

Words can't explain how grateful I am to the many people who directly and indirectly contributed to this work. First of all I would like to thank the Air Force and specifically the Astronautics Department at the United States Air Force Academy for giving me this amazing opportunity. The Air Force has been incredibly good to me. There are also many talented and wonderful Air Force officers who have I have had the privilege of serving with who continue to inspire and encouraged me. Thank you.

I am also blessed to have a tremendous thesis committee. Together they have taught me more than I ever dreamed possible. Dr. Peter Bender, thank you for taking the time out of your busy schedule to be a part of my committee and for your insight and encouragement. Dr. Dan Kubitscheck, thank you for your friendship and expertise in evaluating my work and for the work you performed to aid my research. Your advice and suggestions taught me a lot and made my work better. Dr. Kenn Gold, I also very much appreciate your friendship, encouragement and support. You are wise beyond your years and a true friend. Dr. Penny Axelrad, you know more about GPS than anyone else I know. Thank you for all you've taught me and for your wonderful insight and advice. Dr. Born, you inspired me to learn everything I can about satellite orbit determination. I have thoroughly enjoyed working with you on every project. Your support and confidence in me and have made all the difference. I can't imagine these last three years without you. I am going to miss you most! Along with my

committee I also need to thank Dr. David Cruickshank for his direct contribution to my work. I wouldn't have accomplished the things I have without the time he spent with me and work he performed on my behalf.

Thanks to GSFC for the opportunity to use GEODE and especially for providing source code. Thank you Scott Mitchell and Ball Aerospace Corporation for your support and guidance through this process. Thank you Dr. Bruce Haines at JPL for all the wonderful data you provided. Thank you Dr. Bill Schreiner and Doug Hunt at UCAR for the GPS/MET data and POE.

I have made many wonderful friends at CU, too many to mention. Thank you Kira for your friendship and MS Word template help. You saved me days of work. To Dallas, all the Mikes, and everyone in CCAR, thank you for your friendship, knowledge and support. I also owe a dept of gratitude to all the Stat OD students I had the pleasure of working with...you taught me more than you know.

My parents have always been a great source of strength and encouragement in my life. Thanks Mom and Dad for your love and for teaching me how to work. I wouldn't be where I am today without you. Know that I love you and appreciate all you've done for me, more than I can ever express. Thank you Carol for your love and encouragement through the years and thank you especially for the time your spent proof reading my dissertation. I am also blessed with wonderful extended family. Thank you Steve and Debbie for your never ending love and support for me and my family and for always being there for me. Thank you John and Lindy for

your example and encouragement. You too have always been there for me, I can't imagine what life you have been like without you.

To Angel and Zachary, my constant source of laughter and joy. You make life so much fun, thank you for always helping me keep a proper perspective. To Julie-ann, thank you for the wonderful care you take of me and the kids. I am so blessed by God to have you as my wife. Know that I could not have finished without you, thank you for your love, understanding and for the hundreds of little notes of encouragement you wrote me.

Finally I thank God for blessing me in so many ways. Thank you God for the many times I called out to You and how You always answered. You have been my ever present source of strength and wisdom and I owe You everything. You always keep Your promises. To me, life is not worth living without You.

My soul finds rest in God alone; my salvation comes from
him. He alone is my rock and my salvation; he is my
fortress, I will never be shaken. Psalm 62:1-2 (NIV)

DEDICATION

I dedicate this work to my sweet bride Julie-ann, to Angel and Zachary and to the One who makes all this work possible.

When I consider Your heavens, the work of Your fingers,
the moon and the stars, which You have set in place...

Psalm 8:3 (NIV)

I am amazed!

TABLE OF CONTENTS

Acknowledgments	v
Dedication	viii
Table of Contents	ix
List of Figures	xiv
List of Tables.....	xvii
Chapter 1	1
Introduction.....	1
1.1 Dissertation Objectives.....	1
1.2 Motivation	1
1.3 Post-processing Systems	4
1.3.1 JPL's GOA II.....	4
1.3.2 NRL's OCEAN.....	5
1.3.3 VMSI's MicroCosm®	7
1.4 Real-time Systems	8
1.4.1 JPL's Real-time GIPSY (RTG)	8
1.4.2 The University of Nottingham's Study.....	9
1.5 Post-processing / Real-time Comparison	10
1.5.1 Error Sources in Real-time	10
1.6 Dissertation Summary	13
Chapter 2	15

	x
GEODE and GPS/MET	15
2.1 GPS/MET	15
2.2 GEODE	18
2.2.1 UDU ^T Factorized Covariance	21
2.2.2 Process Noise	23
2.2.3 Dual Frequency GPS Observations	25
2.2.3.1 Ionospheric Correction	25
2.2.3.2 Interfrequency Bias	28
2.2.4 Height Of Ray Path (HORP) Editing	31
2.2.5 Polar Motion and Δ UT1	33
2.2.5.1 Polar Motion	34
2.2.5.2 Δ UT1	36
2.2.6 All in View Versus Cyclic	37
2.2.7 Antenna Phase Center Offset From Satellite Center of Gravity (CG) 39	
2.2.8 Lagrange Interpolation of Precise GPS Ephemerides	40
2.2.8.1 Broadcast Versus Precise GPS Ephemerides	41
2.2.8.2 GEODE Interpolation Versus Precise GPS Ephemerides	42
2.2.8.3 Lagrange Interpolation Versus Precise GPS Ephemerides	44
2.2.8.4 Precise Ephemerides Interpolation Conclusions and Lagrange Algorithm	46
2.2.8.5 GEODE Results Using Precise GPS Ephemerides	48
2.2.9 JPL High-Rate GPS Clock Estimates	49
2.2.9.1 JPL High-Rate GPS Clock Estimate Challenges	49
2.2.9.2 Application of JPL High Rate GPS Clock Estimates	52
2.3 SA Free T/P Data	53

	xi
2.4 Summary.....	56
Chapter 3	57
Earth Gravity.....	57
3.1 Model Size Integration Results and Computational Burden Estimates.....	58
3.2 GEODE Results and Computational Burden Changes with Various Gravity Model Truncations	61
3.3 Gravitational Acceleration Approximation Function (GAAF).....	65
3.3.1 Method of Pseudocenters.....	66
3.3.2 Benefits of Pseudocenter Formulation Without the C2,0 (J2) Term	68
3.3.3 Polynomial Representation of Pseudocenter as a Function of Height	69
3.3.4 Pseudocenter Interpolation on a Sphere of Common Height	70
3.3.5 GAAF Storage Requirements	71
3.3.6 Integration With GAAF.....	72
3.4 GAAF in GEODE.....	83
3.5 JGM-3 and EGM-96 Gravity Models.....	84
3.6 Summary.....	84
Chapter 4	86
Ionosphere.....	86
4.1 Differenced Range Versus Integrated Doppler (DRVID)	86
4.2 DRVID Development.....	91
4.2.1 Estimation of the Integer Ambiguity N_i	93
4.2.2 Calculation of $\Delta\rho_{ion}$ Using $\Delta\rho_{P1}$ and $\Delta\rho_{L1}$	95
4.2.2.1 Model Bias DRVID	96
4.2.2.2 Zero Bias DRVID	97
4.3 DRVID in GEODE.....	104

	xii
4.3.1 DRVID in GEODE Results	109
4.4 Summary.....	110
Chapter 5	112
Dynamic Model Compensation (DMC)	112
5.1 Dynamic Model Compensation (DMC)	113
5.2 XYZ DMC.....	118
5.2.1 XYZ DMC State Transition Matrix.....	119
5.2.2 XYZ DMC Process Noise Covariance	122
5.3 Radial, In-track, Cross-track (RIC) DMC	124
5.3.1 RIC DMC State Transition Matrix	126
5.3.2 RIC DMC Process Noise Covariance.....	127
5.4 Single Satellite Range and Range Rate Simulation (Simulation 1).....	132
5.4.1 Simulation 1 No Process Noise	133
5.4.2 Simulation 1 GEODE Process Noise.....	134
5.4.3 Simulation 1 XYZ DMC	135
5.4.4 Simulation 1 RIC DMC.....	136
5.5 Multi-satellite Range Simulation (Simulation 2).....	137
5.6 Simulation Conclusions.....	140
5.7 XYZ DMC in GEODE	141
5.7.1 XYZ DMC Tuning	141
5.7.2 XYZ DMC GEODE Accuracy/Precision Results	143
5.7.3 XYZ DMC GEODE Computational Burden Results	145
5.8 RIC DMC in GEODE.....	145
5.8.1 RIC DMC GEODE Results	146
5.9 Summary.....	147

	xiii
Chapter 6	149
Genetic Model Compensation (GMC)	149
6.1 The Genetic Algorithm (GA)	150
6.1.1 Reproduction	151
6.1.2 Crossover	151
6.1.3 Mutation	152
6.1.4 GA Application	152
6.2 GMC Algorithm	153
6.3 GMC in GEODE	157
6.3.1 Implementation	158
6.3.2 GMC Tuning	158
6.3.3 GMC in GEODE Results	159
6.4 Summary	168
Chapter 7	169
Summary, Contributions, Future Work, and Conclusion	169
7.1 Summary	169
7.2 Research Contributions	177
7.3 Recommendations for Future Work	177
7.3.1 GAAF Coefficient Estimation	177
7.3.2 GMC RIC Extension	178
7.3.3 Automated DMC Tuning With the Genetic Algorithm	178
7.3.4 GPS Point Solution Measurement	179
7.4 Conclusion	180
References	182

LIST OF FIGURES

<i>Number</i>	<i>Page</i>
Figure 2.1 – Occultation Description	16
Figure 2.2 – OrbView-1 and GPS/MET	17
Figure 2.3 – OrbView-1 Satellite	17
Figure 2.4 - GEODE GPS/MET Position Error in Mean of J2000 Rotated to RIC Statistics Are Calculated Based On Converges Estimates Only	21
Figure 2.5 – GPS/MET Dual Frequency Ionospheric Delay Corrections	28
Figure 2.6 – GPS/MET Single Frequency Results	30
Figure 2.7 – GPS/MET Dual Frequency Results	31
Figure 2.8 – HORP Editing	32
Figure 2.9 - Polar Motion Plot	35
Figure 2.10 - Broadcast vs. Precise Ephemeris PRN01 2 Feb1997	42
Figure 2.11 - GEODE Interpolator with 5-Minute Interval Ephemeris	43
Figure 2.12 – GEODE Interpolator with 15-Minute Interval Ephemeris	44
Figure 2.13 - Lagrange with 30-Minute Interval and 12th Order Interpolation	45
Figure 2.14 - Lagrange with 30-Minute Interval and 17th Order Interpolation	46
Figure 2.15 – High Rate Clock Corrections for PRN 4 on 3 Feb 1997	50
Figure 2.16 – Broadcast vs. High Rate Clock Biases for PRN 2	51
Figure 2.17 – Broadcast vs. High Rate Clock Biases for PRN 9	52
Figure 2.18 – GEODE SA Free T/P Results	54
Figure 2.19 – T/P Measurement Residuals	55
Figure 2.20 – GPS/MET with High Rate GPS Clock Estimates - Measurement Residuals ...	55

Figure 3.1 - Acceleration Accuracy Comparison of Various Size Gravity Models at Various Altitudes	59
Figure 3.2 - JGM-2 / EGM-96 3D Position Error RSS Comparison.....	65
Figure 3.3 - Six-Point Bi-Variate Interpolation Scheme	70
Figure 3.4 - GEODE / STK Integration Comparison	73
Figure 3.5 - GEODE / STK Difference Comparison.....	74
Figure 3.6 - Linear Nature of Pseudocenters.....	78
Figure 3.7 - GPS/MET Polynomial Fit RMS Error.....	80
Figure 3.8 - GPS/MET GAAF and 30x30 Integration Compared to 70x70	83
Figure 4.1 - PRN01 GPS/MET Elevation Plot.....	99
Figure 4.2 - PRN16 GPS/MET Elevation Plot.....	99
Figure 4.3 - PRN29 GPS/MET Elevation Plot.....	100
Figure 4.4 - PRN14 GPS/MET Elevation Plot.....	100
Figure 4.5 - PRN10 GPS/MET Elevation Plot.....	101
Figure 4.6 - Dual Frequency Ionospheric Correction at GPS Tracking Arc Start.....	102
Figure 4.7 - PRN 22 Zero Bias DRVID, Dual Frequency Comparison.....	103
Figure 4.8 - PRN 23 Zero Bias DRVID, Dual Frequency Comparison.....	104
Figure 4.9 - DRVID Elevation Angle Example	105
Figure 4.10 - 4 Feb 1997 GPS/MET DRVID Dual Frequency Comparison.....	106
Figure 4.11 - PRN01 GPS/MET DRVID in GEODE	107
Figure 4.12 - PRN16 GPS/MET DRVID in GEODE	107
Figure 4.13 - PRN05 GPS/MET DRVID in GEODE	108
Figure 4.14 - PRN27 GPS/MET DRVID in GEODE	108
Figure 5.1 - Particle Moving at Constant Velocity.....	113
Figure 5.2 - Simulation 1 No Process Noise Results.....	133
Figure 5.3 - Simulation 1 GEODE Process Noise Results	134

	xvi
Figure 5.4 – Track Simulation 1 XYZ DMC Results	135
Figure 5.5 – Simulation 1 RIC DMC Results	136
Figure 5.6 – Simulation 2 No Process Noise Results.....	138
Figure 5.7 - Simulation 2 GEODE Process Noise Results.....	139
Figure 5.8 - Simulation 2 XYZ DMC Results	139
Figure 5.9 – Simulation 2 RIC DMC Results	140
Figure 6.1 – GMC Algorithm.....	157
Figure 6.2 – GPS/MET High Rate GPS Clock GMC/DMC Comparison.....	162
Figure 6.3 – GPS/MET Mean DMC Parameters from GMC.....	164
Figure 6.4 - TOPEX GMC/DMC Comparison	166
Figure 6.5 – TOPEX Mean DMC Parameters from GMC.....	167
Figure 7.1 – GA for DMC Tuning	179

LIST OF TABLES

<i>Number</i>	<i>Page</i>
Table 1.1 – OCEAN OD Results	7
Table 1.2 – Post-processing/Real-time Comparison	10
Table 2.1 – GEODE GPS/MET Single Versus Dual Frequency Error Results	29
Table 2.2 - GEODE GPS/MET Single Versus Dual Frequency Measurement Residuals	30
Table 2.3 – GEODE GPS/MET Varying α_{\max} Results.....	33
Table 2.4 – GEODE GPS/MET Results With and Without Polar Motion.....	36
Table 2.5 – GEODE GPS/MET Results With and Without $\Delta UT1$	37
Table 2.6 – GEODE GPS/MET ALL vs. CYCLIC Comparison.....	38
Table 2.7 – GEODE GPS/MET Min Sampling Frequency Tuning Results	39
Table 2.8 – GEODE GPS/MET Antenna Phase Center Mapping Results.....	40
Table 2.9 - Statistics of Results.....	46
Table 2.10 – GEODE GPS/MET Results Using Precise GPS Ephemeris	48
Table 2.11 – GEODE T/P Results Using Precise GPS Ephemeris	48
Table 2.12 – GEODE GPS/MET SA Off Results Comparison	53
Table 2.13 – SA Free T/P Results with GEODE	56
Table 3.1 - Computational Burden and Accuracy of Various Truncations of the EGM-96 Gravity Model.....	60
Table 3.2 – Initial Conditions of Propagation With EGM-96 70x70 Gravity Model	61
Table 3.3 – Earth Gravity JGM-2 State Noise Correlation Times	63
Table 3.4 – GEODE GPS/MET JGM-2 Comparison	63

Table 3.5 – Earth Gravity EGM-96 State Noise Correlation Times	64
Table 3.6 – GEODE GPS/MET EGM-96 Comparison.....	64
Table 3.7 – Original GPS/MET GAAF Storage Requirements For 3 Coefficients	72
Table 3.8 – Test Pseudocenters.....	77
Table 3.9 – Example GPS/MET GAAF Coefficients and RMS for y1	79
Table 3.10 – GPS/MET GAAF and 30x30 Integration Compared to 70x70.....	82
Table 3.11 – GEODE GPS/MET Gravity Model Results Comparison	84
Table 4.1 – Error Between DRVID Methods and Dual Frequency	97
Table 4.2 – GEODE With Ionospheric Correction for GPS/MET.....	109
Table 4.3 – GEODE With Ionospheric Correction for T/P.....	110
Table 5.1 – Summary of Results with 3 TrackSats and 1 m Noise on Range.....	137
Table 5.2 - Summary of Results with 4 TrakSats and 50 m Noise on Range	140
Table 5.3 – GPS/MET XYZ DMC Parameter Tuning.....	142
Table 5.4 – GPS/MET XYZ DMC “Optimal” Parameters	142
Table 5.5 – GPS/MET With High Rate GPS Clocks XYZ DMC “Optimal” Parameters.....	143
Table 5.6 - GEODE Results With and Without XYZ DMC.....	143
Table 5.7 - GEODE Results With and Without XYZ DMC Using High Rate Clock Estimates to Correct for SA	144
Table 5.8 - SA Free TOPEX Results With and Without XYZ DMC	144
Table 5.9 – GPS/MET RIC DMC Parameter Tuning	146
Table 5.10 – GPS/MET RIC DMC “Optimal” Parameters.....	146
Table 5.11 - GEODE Results With and Without RIC DMC	147
Table 6.1 – GMC Design Space Bracketing	159
Table 6.2 - GEODE GMC Results Comparison Using High Rate Clock Estimates to Correct for SA.....	163
Table 6.3 - SA Free TOPEX GMC Results	165

	xix
Table 7.1 – Chapter 2 through Chapter 4 Results Summary	175
Table 7.2 – Chapter 5 and Chapter 6 Results Summary	176

CHAPTER 1

Introduction

1.1 Dissertation Objectives

The objectives of this research are to further evaluate and improve Goddard Space Flight Center's (GSFC's) Global Positioning System (GPS) Enhanced Orbit Determination Experiment (GEODE) [1] software. GEODE is evaluated with various processing scheme changes with the understanding that it will be employed for real-time satellite Orbit Determination (OD), on board a satellite. Improvements to GEODE are sought in terms of enhanced autonomy, improved accuracy/precision and reduced computational burden. The goal of this research is to autonomously process GPS pseudoranges, in real-time, to produce orbit estimates with better than 1-meter total position (3D) Root Sum Square (RSS) error for Low Earth Orbit (LEO) satellites. The estimates produced by GEODE are compared to Precise Orbit Ephemeris (POE) generated by GSFC and the Jet Propulsion Laboratory (JPL).

1.2 Motivation

The topic of accurate, autonomous real-time satellite OD is receiving significant attention [2-8] and with GPS Selective Availability (SA) being turned

off on 2 May 2000, it will receive even more attention in the near future. Mission planners want very accurate (tens of cm to tens of meters) position, velocity and/or attitude information in real-time, while minimizing the work required to achieve these results (better, faster, cheaper). Several trends driving autonomy, timing, and accuracy requirements are planned deployment of constellations of satellites, the desire for real-time geodetic measurements, challenging Earth resource science objectives and a movement toward reducing dependence on ground-based tracking assets [9]. It is even becoming desirable to perform OD in real-time, on board an Earth orbiting satellite, where accurate position, velocity and attitude information are made available for other satellite instruments [4].

An obvious choice for providing observations for an autonomous OD scheme is the Global Positioning System (GPS). GPS provides unprecedented observability to LEO satellites providing continuous, all-weather observations without user intervention. The limitation in using GPS for precise OD used to be the accuracy of the measurements. The User Equivalent Range Error (UERE) as published by the GPS Joint Program Office (JPO) was 33.3 meters (1σ) using the GPS Standard Positioning Service (SPS) [10]. SPS GPS measurement errors were dominated by errors due to SA but SA has now been turned off (as of 2 May 2000). Now GPS measurement errors are dominated by the ionosphere, troposphere, GPS satellite ephemerides, multi-path, and receiver noise. The effect the measurement errors have on satellite OD has been minimized, if not

completely removed, by post-processing the GPS measurements using sophisticated filters and data gathered from globally distributed receiving stations.

Therefore, the distinction between post-processing (or processing in near real-time) and real-time is very important when discussing the accuracy attained using GPS measurements for satellite OD. Post-processing (also near real-time) implies providing solutions at least several hours, usually more, after observations are taken. Real-time implies calculating solutions within minutes, seconds or even a fraction of a second after observations are made. Herein, real-time OD will be defined as completing the calculations required to perform the OD measurement update prior to acquiring the next measurement. The main differences between these two types of systems are that post-processing systems usually corrected for SA, use very sophisticated ionospheric models, use high fidelity gravity models and use very accurate GPS satellite ephemerides rather than those broadcast. Each of these "differences" require a prohibitive computational burden for a real-time system or unacceptable interaction for true autonomy. Obviously, since SA has been turned off, post-processing systems no longer correct for it. Autonomy defined here, implies minimal or no interaction with external resources, except the acquisition of measurements and the collection of information in the GPS navigation message. The next two sections of this chapter outline several state-of-the-art post-processing and real-time software suites to distinguish the differences between these two types of systems.

1.3 Post-processing Systems

There are several software packages designed to calculate precise satellite ephemeris using GPS observations by post-processing (on the ground) or in near real-time. Several examples are the Jet Propulsion Laboratory's (JPL) GPS-Inferred Positioning System (GIPSY)/OASIS II (GOA II) [11], the Naval Research Laboratory's (NRL) Orbit/Covariance Estimation and Analysis Software (OCEAN) [12], Van Martin System Inc.'s (VMSI) MicroCosm®, GEODYN, Utopia, etc. GOA II, OCEAN and MicroCosm® are described here.

1.3.1 JPL's GOA II

GOA II is a collection of Fortran programs and C-shell or Perl encapsulating scripts created by JPL. Most of the following features of GOA II were extracted from [13]:

- batch-sequential and filter-smoother
- network processing of globally distributed GPS receiver data to eliminate SA using white noise clock estimation with one reference clock [14]
- simultaneous estimation of GPS satellite orbits (generation of precise GPS Ephemeris (GPSE))
- orbit integration using spherical harmonic gravity field expansion (JGM-2 70x70 or JGM-3 70x70), the effects of the sun, moon, and planets, plus non-gravitational forces to account for atmospheric drag and solar radiation pressure
- modeling of the known dynamics of the Earth, including solid Earth tides, precession, nutation, polar motion, pole tides, and ocean loading
- ionospheric group range delay and phase advance estimation based on Bent or IRI95 ionosphere models
- wet and dry tropospheric delay modeling including ray bending and Earth curvature, and the stochastic estimation of mapped zenith delays and clock biases as random walk or Gauss-Markov process noise

- estimation of unmodeled or mismodeled forces using the Reduced Dynamic Technique (RDT) [15]

GPS satellite orbits computed using GOA II have a radial RMS in the 7-10 cm range. Comparison of The Ocean Topography Experiment (TOPEX)/Poseidon (T/P) orbits derived from GPS data collected on board the T/P satellite compared with orbits produced by other sources (e.g., Doris and Satellite Laser Ranging (SLR) analyzed by other institutions) have shown 2-3 cm radial RMS and 15 cm 3D RSS [13]. JPL has determined operational GPS orbits for T/P for many years with typical latency of 11-17 hours after the last GPS data point is received on board the satellite. In comparison, GSFC definitive orbits based on Doris and SLR data are delivered with a latency of about 40 days. The definitive GSFC orbits and JPL orbits generated with GOA II have an RMS difference of less than 4 cm radially [16]. JPL has automated GOA II to produce orbits with sub-10 cm radial RMS accuracy with about 10-hour latency but recent improvements in JPL's processing system might soon reduce this to around 1-hour latency. JPL anticipates OD accuracy at the 1 cm level (1σ radially) will be demonstrated in the not too distant future [16]. In this dissertation GEODE T/P position estimates will be compared against JPL GOA II POE.

1.3.2 NRL's OCEAN

OCEAN is a precise satellite OD software system created by the Astrodynamics and Space Applications Office of the Naval Center for Space

Technology at the NRL. The OCEAN suite contains a batch weighted least squares estimation technique and an extended Kalman filter and backwards smoother to process various range, Doppler and angle observations. It can process GPS data or SLR data. The previous information and the following features were extracted from [12].

- Choice of Earth gravity models including JGM-2 or EGM96
- Jaccia 1971 atmospheric drag model
- Solar radiation pressure using vehicle macro-modeling
- Sun, Moon and planetary third body accelerations
- Models solid Earth and Ocean tide accelerations
- Processes externally available precise or broadcast GPS ephemerides
- Capable of processing multiple satellites and ground stations simultaneously
- Differential correction using ground station receiver data
- Estimation of unmodeled or mismodeled (empirical) accelerations

OCEAN was used to process T/P data from 18 November 1993 when all GPS satellites had Anti-Spoofing (AS) off but only 17 of 24 satellites had SA off. AS is the encryption of the GPS P-code to keep adversaries from “spoofing” a Precise Positioning System (PPS) capable receiver [17]. Turning AS off essentially allows a dual frequency receiver, without decryption capabilities, to receive carrier phase and pseudorange measurements on both the L1 and L2 channels. Only the data from the 17 SA off satellites were processed. The results compared to JPL’s T/P POE with precise GPSE are shown below in Table 1.1.

Table 1.1 – OCEAN OD Results

RMS	Precise GPSE (simulated post-processing)
Radial	0.10 m
Along-track	0.31 m
Cross-track	0.16 m
Total	0.37 m

Again, the GPS data in this study are SA and AS free.

1.3.3 VMST's MicroCosm®

MicroCosm® is a satellite orbit and geodetic parameter estimation software suite developed by VMST. MicroCosm® improves upon and fully implements the NASA GEODYN II, version 8609, precision orbit and geodetic parameter determination software system. The following details concerning MicroCosm® were extracted from [18]:

- Bayesian least squares batch processor
- automatic carrier phase cycle slip detection and removal
- network processing of globally distributed GPS receiver data to eliminate SA using single, double or triple differencing
- simultaneous estimation of geodetic parameters
- orbit integration using spherical harmonic gravity field expansion (JGM-2 70x70 or JGM-3 70x70), the effects of the sun, moon, and planets, plus non-gravitational forces to account for atmospheric drag and solar radiation pressure
- modeling of the known dynamics of the Earth, including solid Earth tides, precession, nutation, polar motion, pole tides, and ocean loading
- estimation of zenith tropospheric parameters for each IGS ground station
- estimation of radial, in-track and cross-track empirical accelerations

MicroCosm® was used to perform orbit determination for the GPS/Meteorology (GPS/MET) experiment using GPS carrier phase observations. Internal and external orbit overlap comparisons show MicroCosm® is capable of estimating GPS/MET orbits at the 30 cm 3D RSS level [19]. In this dissertation, GEODE GPS/MET position estimates will be compared against MicroCosm® generated GPS/MET orbits.

1.4 Real-time Systems

There are also several real-time software suites available. Examples are JPL's Real-time GIPSY, the Microcosm Autonomous Navigation System (MANS) [20], the Brazilian National Institute of Space Research's (INPE's) ORBesT [21] and GSFC's GEODE [22]. Also, the University of Nottingham's Institute of Engineering Surveying & Space Geodesy (IESSG) developed another unnamed system [2]. There is currently no published information on space qualified (actually flown in space) precise, real-time OD software. Real-time GIPSY and the University of Nottingham's system are discussed below; GEODE is discussed in Chapter 2.

1.4.1 JPL's Real-time GIPSY (RTG)

RTG is an ANSI C version of GOA-II created by JPL to accommodate high data rates (1 Hz) and improve portability to systems other than UNIX. JPL's goal is to incorporate all the precise models from GOA-II, make it suitable for

imbedded systems such as GPS receivers and make it capable of real-time processing [16]. Compiler options in RTG allow it to be scaled to meet various processor load requirements [16]. To provide the best accuracy, RTG will be used in conjunction with a global Wide Area Augmentation System (WAAS) or a Wide Area Differential GPS (WADGPS) system. Without WAAS or WADGPS RTG has shown 3D RSS values in the 4-6 meter range when used to process T/P data with broadcast GPS ephemeris and SA on [16].

1.4.2 The University of Nottingham's Study

In a study for the UK Defense and Evaluation Research Agency (DERA), The Institute of Engineering Surveying & Space Geodesy (IESSG) at the University of Nottingham developed an extended Kalman filter, using Reduced Dynamic Tracking (RDT), to generate real-time satellite position estimates with radial RMS error of 1.08 m 1σ and a 3D RSS error of 3.95 m 1σ [2]. IESSG used real and simulated Standard Positioning System (SPS) data from T/P. They reported the filter converged after approximately five hours [23]. They used a JGM-2 45x45 gravity field, a simple drag model (due to T/P's relatively high orbit), and broadcast GPS ephemerides. The application required approximately 500 kb of computer memory and the code could produce solutions within one minute of recording an observation. A trade study between microprocessors was also performed finding a military standard 1750A microprocessor (8086 equivalent) to be more than capable of producing the solutions each minute [2].

1.5 Post-processing / Real-time Comparison

A comparison of the characteristics common to post-processing and real-time systems is shown below in Table 1.2. Details of research outlined in this dissertation to close the gap between post-processing and real-time systems are presented next.

Table 1.2 – Post-processing/Real-time Comparison

Area of Concern	Post-processing	Real-time
SA Treatment	Differential Correction	Broadcast DGPS
GPSE Used	Precise	Broadcast
Gravity Model	JGM-2 70x70, JGM-3 70x70 or EGM-96 300x300	Truncated Models (45x45 largest, usually 30x30)
Drag Model	Complex	Simple
Radiation Pressure Model	Complex	Simple or Not at All
Ionospheric Model	Bent, IRI95, PRISM	None
Observations Used	Pseudorange, Integrated Doppler	Pseudorange
Filter Type	Usually Batch or Sequential	Extended Kalman Filter
Empirical Force Estimation	Usually RDT	None

1.5.1 Error Sources in Real-time

SA was the U.S. Air Force's intentional degradation of GPS measurement accuracy. SA was formally implemented on 25 March 1990 and turned off on 2 May 2000. SA is accomplished through the dithering of GPS satellite clocks [10]. The usual method for dealing with SA is to collect data at geographically separated locations with known position and use single or double differencing to remove SA errors. Fortunately, SA is no longer a factor in real-time satellite OD as there is currently no real-time method to reduce its contribution to degrading OD accuracy.

Another error source that is difficult to deal with in real-time is error in the knowledge of the GPS satellite's position. Currently the method used to calculate GPS satellite position, in real-time, is to evaluate a series of equations using information broadcast by each GPS satellite. In Zumberge [24] the RMS errors between the broadcast and precise GPS ephemeris for the period 1 July 1993 – 22 Oct 1993 are reported as 1.2 m radial, 3.2 m cross-track and 4.5 m along-track. The total 3D RSS error is therefore 5.7 m. Depending on the type of GPS data utilized (including or not including SA and/or AS), the difference in accuracy between the broadcast and precise ephemerides has been reported to be a significant source of error in determining the orbit of a satellite using GPS observations [12, 25-27]. To mitigate the errors in broadcast GPS ephemerides, precise ephemerides are often used. There are two methods of obtaining the precise ephemerides: solving for the GPS orbits simultaneously with the user satellite state and fixing the GPS ephemerides to an independent determination, such as the International GPS Service for Geodynamics (IGS) [28]. Both of these methods require significant overhead and are therefore not implemented in real-time systems. However, predicted GPS ephemerides are available and in certain circumstances could be uplinked daily to a satellite. Chapter 2 presents a comparison of real-time satellite OD error results using broadcast and precise GPS ephemerides.

The model used to predict the acceleration due to the Earth's gravity can be a significant error source in real-time systems. Therefore, a tradeoff study is

performed in Chapter 3 to determine the effect of using various truncated gravity models. In addition a gravity acceleration approximation method is introduced to recover the accuracy of large models while reducing computational burden.

Measurement errors due to the ionosphere can also affect satellite OD accuracy. Chapter 4 presents details concerning the magnitude of errors due to ionospheric path delay seen by the GPS/MET satellite and an innovative method of removing these errors when a single frequency GPS receiver is used. The technique presented is known as Differenced Range Verses Integrated Doppler (DRVID) [29].

Due to limited space environment knowledge, computational burden restrictions and the desire for autonomy, all the forces acting on a satellite cannot be modeled. Therefore, Dynamic Model Compensation (DMC) is presented in Chapter 5 to not only estimate unmodeled and mismodeled forces as part of the filter state but also to simultaneously provide a method of formulating the filter process noise variance-covariance.

One challenge with DMC is tuning of the time correlation coefficient and the process noise standard deviation. Chapter 6 presents a Genetic Algorithm (GA) in the form of Genetic Model Compensation (GMC) [9]. GMC adaptively tunes the constants used in DMC.

1.6 Dissertation Summary

There are significant differences between the satellite OD accuracy attainable in a post-processing scenario as compared to in real-time. The purpose of the research presented in this dissertation is to offer suggested improvements to GSFC's GEODE software suite to enhance autonomy, improve accuracy and reduce computational burden.

Chapter 1 provides a definition of the term real-time and a review of state-of-the-art post-processing and real-time software suites and their differences. Chapter 2 discusses details of GEODE and the spacecraft and data used to evaluate GEODE's performance. Chapter 3 deals with the accuracy and computational burden of the gravitational model used in GEODE and suggests a promising method to significantly reduce the computational burden. This gravitational approximation sacrifices computer memory but not accuracy. Chapter 4 describes the errors due to the ionosphere in GPS measurements and suggests a method to estimate and remove ionospheric error using a technique called Differenced Range Versus Integrated Doppler (DRVID) [29-32]. Chapter 5 presents a derivation of an XYZ and a Radial, In-track, Cross-track (RIC) version of Dynamic Model Compensation (DMC) [9], results of two simulations implementing RIC DMC and the improvements to GEODE through the use of DMC. Chapter 6 details an extension of DMC by the use of a Genetic Algorithm (GA) to adaptively tune the time correlation coefficient (τ) and

standard deviation of the DMC forcing noise (σ) [9]. Finally, Chapter 7 provides conclusions and suggestions for future work.

CHAPTER 2

GEODE and GPS/MET

This chapter provides an overview of the OrbView-1 satellite (formerly known as MicroLab-1) carrying the GPS/MET experiment and information concerning the GPS measurements collected by GPS/MET. Details are provided on GEODE and results presented concerning the optimization of inputs to GEODE. Finally, a Lagrange scheme is introduced to interpolate precise GPS ephemerides and a method presented for removing the effects of SA from GPS/MET data collected 2–10 Feb 1997.

2.1 GPS/MET

OrbView-1 was launched on a standard Pegasus rocket from Vandenberg AFB, CA, on 3 April 1995 into a 747 x 732 km orbit with an inclination of 70.0°. The primary payload on board OrbView-1 is the Optical Transient Detector (OTD) used in imaging lightning strikes. OTD has a 10-km resolution, a 1,300-km swath width, and is managed by the NASA Marshall Space Flight Center [33]. GPS/MET is a secondary payload on board the OrbView-1 satellite built by Orbital Sciences Corporation (OSC). The GPS/MET experiment relies on an active limb sounding technique using radio occultation observations taken

by the on board GPS receiver. Figure 2.1 shows a diagram of the occultation of a GPS signal by the Earth's atmosphere.

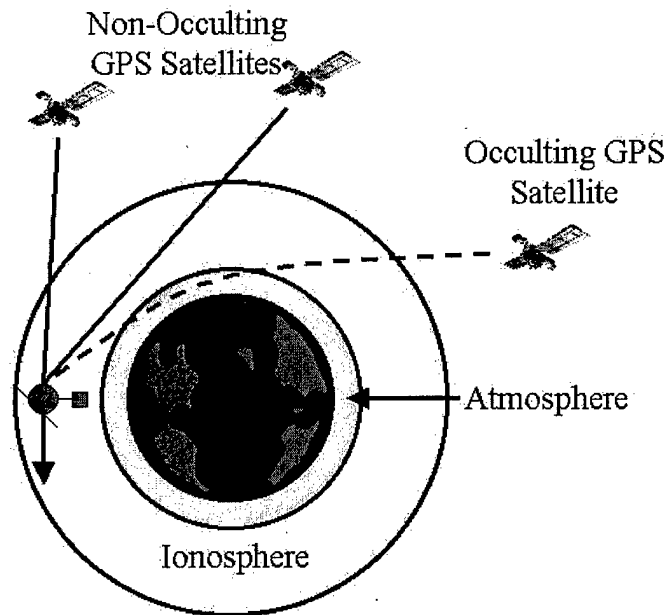


Figure 2.1 – Occultation Description

The GPS/MET receiver is a JPL modified TurboRogue with a microstrip patch antenna [19]. The occultation data is used for recovery of accurate refractivity, pressure, temperature and moisture profiles of the atmosphere [34]. Optimal occultation tracking is performed when the GPS/MET antenna is pointing in the anti-velocity direction, therefore, a fixed yaw steering configuration is implemented. OrbView-1 is gravity-gradient stabilized and attitude is maintained using three torque rods, six Sun sensors, two Earth sensors and a magnetometer mounted on the gravity boom. Attitude accuracy of $5\text{-}10^\circ$ is maintained. The GPS/MET antenna phase center is offset from the OrbView-1 satellite's center of gravity (CG) by

-0.507 m in the x direction
0.039 m in the y direction
-0.178 m in the z direction [19]

See Figure 2.2 for a diagram and Figure 2.3 for a photo of OrbView-1.

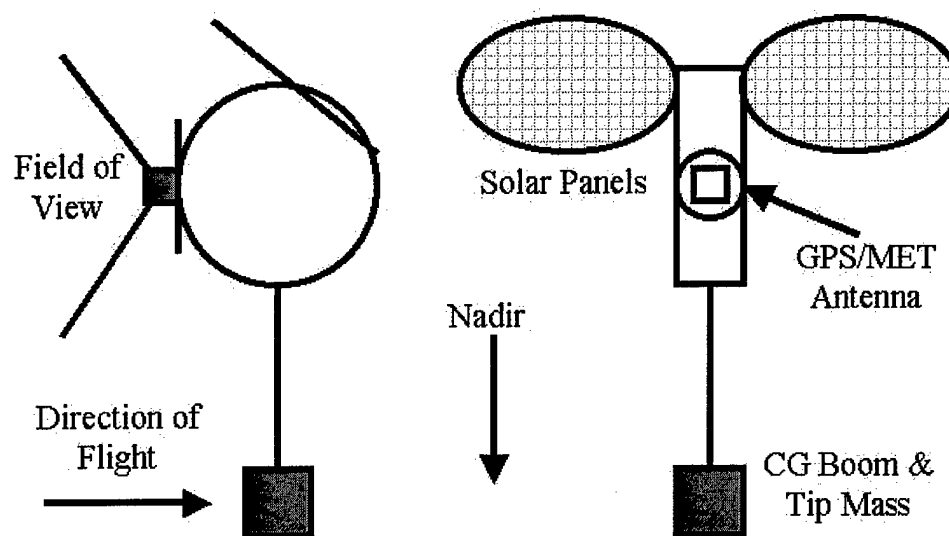


Figure 2.2 – OrbView-1 and GPS/MET

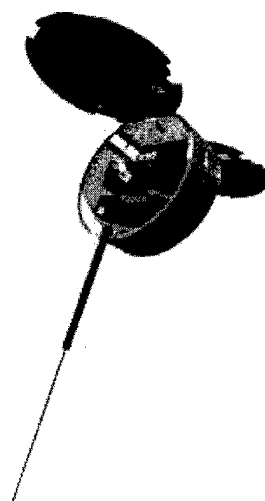


Figure 2.3 – OrbView-1 Satellite

Photo Courtesy of: <http://www.orbimage.com/satellite/orbview1/orbview1.html>

2.2 GEODE

GSFC developed GEODE as a real-time software analysis package [35].

GEODE is highly modular, programmed in ANSI C and has been targeted to UNIX and PC systems as well as the RAD6000 RISC microprocessor. It requires a modest 400 kilobytes of computer RAM. GEODE was originally designed as experimental software to fly on the SSTI Lewis satellite contracted by NASA to TRW [35]. GEODE is implemented with an Extended Kalman Filter (EKF), which feeds a real-time state propagator. GEODE is designed to be hosted on either a spacecraft flight computer, or in a GPS receiver's processing unit. Pre-launch orbit determination studies using GEODE indicate that 1σ orbit accuracy of 10 m in position, and 0.01 m/s in velocity may be attained in the presence of SA. The pre-launch studies were accomplished with Extreme Ultraviolet Explorer (EUVE) and T/P raw pseudorange data. The SSTI Lewis satellite was to be placed in a 523 km, Sun Synchronous orbit [36]. Unfortunately, SSTI Lewis was lost shortly after its launch in August of 1997 and therefore GEODE is not flight qualified. Below is a summary of relevant information concerning GEODE [37].

- JGM-2 30x30 gravity model
- Solar and Lunar point mass 3rd body force model
- Harris-Priester atmospheric drag model
- Geometrical editing of measurements with high ionospheric errors
- Broadcast GPS ephemerides used
- Extended Kalman Filter (EKF) implemented
- UDU^T factorized state error covariance

- Uplink of polar motion coefficients, accurate a priori state information and a priori state error and process noise covariance terms
- Processes pseudorange measurements only – not carrier phase

Figure 2.4 is generated using position data estimated by GEODE compared to post processed POE (accurate to approximately 30 cm radially) generated with MicroCosm®. The observations used by GEODE are GPS pseudoranges collected by the GPS/MET experiment on 4 Feb 1997. AS is off but SA is on. There are 24 hours of data with one pseudorange processed every 10 seconds. It took less than one minute to process the entire 24 hours of data on a 450 MHz Pentium II with 128 MB RAM. The filter converged after processing approximately two hours of data and yielded a converged 3D RSS error of 11.61 m. All RMS and RSS statistics presented in this dissertation are calculated using converged estimates (after 2 hours) only. Figure 2.4 shows plots of the Radial, In-track and Cross-track (RIC) errors compared to the MicroCosm® mean of J2000 POE, along with the square root of the filter's estimated state error covariance (positive and negative), also called the estimated standard deviation. Figure 2.4 also shows the RIC RMS values and the mean of the errors in each direction. A brief description of why the RMS and mean of errors are shown in this dissertation as well as a brief discussion of systematic errors follows.

Without any systematic errors the RMS values presented would indicate the level of precision and accuracy attained by GEODE. In the presence of systematic errors, the RMS really only provides a measure of precision. In Figure 2.4 systematic errors can be seen in the periodic nature of the plots and possibly in

the mean of the comparison error. For instance, the cross-track plot in Figure 2.4 shows a periodicity with frequency of once per satellite orbit. This “once per rev” periodicity is probably caused by GEODE/POE coordinate transformation differences but could also be due to errors in the filter’s dynamic and measurement models. Periodicities in errors are not revealed in the mean and RMS of error statistics. Looking at plots and/or plotting the power spectrum of the errors can reveal periodic errors. The in-track plot in Figure 2.4 shows a mean in the difference between the POE and the filter’s estimate of -1.12 m in the in-track direction. It is difficult to ascertain the cause of the error mean but it could be from systematic or random errors. Systematic errors can be introduced into the filtering process through the GPS pseudorange measurements, the mechanics of the filter, the observation model or the dynamic model. Random errors are most certainly introduced in the GPS pseudorange measurements but could also be introduced in other ways.

Since the source of the mean of comparison error shown in the in-track plot in Figure 2.4 cannot be determined, no conclusions can be drawn from it alone. However, if a change is made to GEODE that decreases the error mean, then it might be concluded the change reduced some systematic error. In this dissertation improvements to GEODE will be gauged not only by their affect on the RMS and RSS of the errors between GEODE’s satellite position estimates and POE but also by the affect on the mean of the comparison errors.

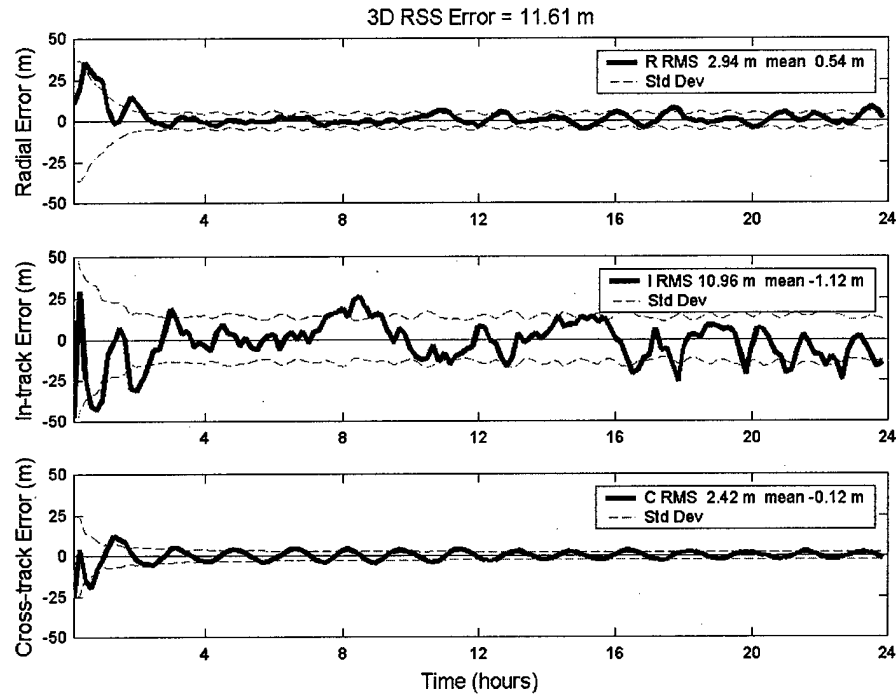


Figure 2.4 - GEODE GPS/MET Position Error in Mean of J2000 Rotated to RIC
Statistics Are Calculated Based On Converges Estimates Only

2.2.1 UDU^T Factorized Covariance

The conventional Extended Kalman Filter (EKF) formulation is shown below [38].

$$\bar{P}_k = \Phi(t_k, t_{k-1}) P_{k-1} \Phi^T(t_k, t_{k-1}) + Q_k \quad (2.1)$$

$$y_k = Y_{k_{\text{observed}}} - Y_{k_{\text{computed}}} \quad (2.2)$$

$$K_k = \bar{P}_k H_k^T (H_k \bar{P}_k H_k^T + R)^{-1} \quad (2.3)$$

$$\hat{X}_k = \bar{X}_k + K_k y_k \quad (2.4)$$

$$P_k = (I - K_k H_k) \bar{P}_k \quad (2.5)$$

where

- $\bar{P}_k \equiv$ time updated covariance matrix at time k
- $P_{k-1} \equiv$ measurement updated covariance at time $k-1$
- $Q_k \equiv$ process noise covariance matrix at time k
- $y_k \equiv$ measurement residual at time k
- $K_k \equiv$ Kalman gain at time k
- $H_k \equiv$ observation-state matrix at time k
- $\bar{X}_k \equiv$ A priori estimate of the state at time k
- $\hat{X}_k \equiv$ best estimate of the state at time k
- $R \equiv$ Observation Error Covariance Matrix

Implementation of the conventional EKF can lead to filter divergence either through inaccuracies in the mathematical models used in the filter (dynamic or measurement models) or through the state error covariance matrix becoming non-positive definite. Since errors introduced during the computational procedure are the cause of the covariance matrix becoming non-positive definite, a reformulation of the algorithm can minimize these errors [38]. Therefore, several filter algorithm modifications have been developed to improve the numerical stability of the Kalman filter.

The UDU^T factorized covariance implementation of the Kalman filter was first introduced by Thornton and Bierman [39, 40] where

$$P = UDU^T \quad (2.6)$$

U is unit upper triangular and D is diagonal. Factorizing the state error covariance matrix in this way avoids square roots, guarantees non-negativity of the computed covariance and keeps the filter numerically stable and accurate [37].

Numerical stability means that an algorithm computes the same result even when the initial conditions are slightly perturbed. The UDU^T factorization provides numerical stability [41]. The UDU^T factorization algorithm performs the time and measurement updates on the U and D matrices rather than directly updating the P matrix. The algorithm is implemented in GEODE so the measurement update is performed on each measurement independently. Maybeck shows both the numerical advantages and computational burden changes due to employing various covariance factorizations. Maybeck's conclusion is that with a 10 member state and two measurements to update, UDU^T factorization provides the best balance of numerical stability and reduced computational burden [41]. The algorithm as implemented in GEODE can be found in the GEODE Mathematical Specification [37].

2.2.2 Process Noise

Kalman filter algorithms use the process noise covariance matrix, Q_k , to correct the state error covariance for inadequacies in the force model. See equation (2.1). Without process noise, elements of the covariance matrix asymptotically approach zero, as does the Kalman gain. When this occurs, as seen in equation (2.4), the filter begins ignoring measurements [38]. Ignoring measurements forces the filter to rely solely on the dynamic model and since the system's dynamics are linearized, filter divergence can result.

GEODE's EKF uses a "physically connected" algorithm for calculating the gravitational acceleration's contribution to the position and velocity components of the state error covariance [37]. The "physically connected" algorithm uses gravity model variances in the position and velocity process noise formulations. Gravitational acceleration forces are chosen since they provide the largest force model errors. The formulation of the position and velocity process noise components (upper left 6x6 of the Q matrix) rely heavily on radial, in-track, and cross-track correlation times provided to GEODE in the uplink command file. These correlation times change depending on the semi-major axis of the user satellite's orbit and the degree and order of the gravity model used in GEODE. The correlation times are calculated using an algorithm presented in Wright [42] and Fortran code is available with GEODE for these calculations. Example correlation times for various truncations of the JGM-2 and EGM-96 gravity models are shown in Chapter 3.

Random-walk algorithms are implemented for the remaining elements of the state, i.e., the receiver clock bias, receiver clock bias drift rate, atmospheric drag coefficient (C_D) and the solar radiation pressure coefficient (C_R). The process noise covariance algorithms for these elements of the state are also found in the GEODE Mathematical Specification [37].

2.2.3 Dual Frequency GPS Observations

GEODE was designed for use with a single frequency GPS receiver.

Therefore, several changes are made to GEODE's measurement handling procedures to take advantage of dual frequency GPS observations. The reason for the change is that the GPS/MET data was collected using a dual frequency receiver, with AS off.

2.2.3.1 Ionospheric Correction

If dual frequency GPS measurements are used in GEODE, the P1 and P2 measurements can be combined to remove the first order ionospheric effects on the pseudorange and phase measurements [10, 43]. The ionospheric time delay at the L_1 frequency is

$$\Delta t_{L_1} = \frac{1}{c} \left(\frac{f_2^2}{f_1^2 - f_2^2} \right) (\rho_{P_1} - \rho_{P_2}) \quad (2.7)$$

Likewise the ionospheric time delay at L_2 is

$$\Delta t_{L_2} = \frac{1}{c} \left(\frac{f_1^2}{f_1^2 - f_2^2} \right) (\rho_{P_1} - \rho_{P_2}) \quad (2.8)$$

where

$c \equiv$ the speed of light in a vacuum = 299,792,458 m/s

$f_1 \equiv$ 1575.42 MHz

$f_2 \equiv$ 1227.6 MHz

$\rho_{P_1} \equiv$ pseudorange measurement taken on L_1

$\rho_{P_2} \equiv$ pseudorange measurement taken on L_2

Therefore, the ionosphere free pseudorange measurement is:

$$\rho_{P_3} = \rho_{P_1} + c\Delta t_{L_1} = \rho_{P_2} + c\Delta t_{L_2} \quad (2.9)$$

or

$$\rho_{P_3} = \rho_{P_1} + \left(\frac{f_2^2}{f_1^2 - f_2^2} \right) (\rho_{P_1} - \rho_{P_2}) \quad (2.10)$$

leading to

$$\rho_{P_3} = \left(\frac{f_1^2}{f_1^2 - f_2^2} \right) \rho_{P_1} - \left(\frac{f_2^2}{f_1^2 - f_2^2} \right) \rho_{P_2} \quad (2.11)$$

Substituting in the L1 and L2 frequencies and simplifying we get:

$$\rho_{P_3} = \frac{1698\rho_{P_1} - 1031\rho_{P_2}}{667} \quad (2.12)$$

an approximation to this equation is:

$$\rho_{P_3} = 2.5\rho_{P_1} - 1.5\rho_{P_2} \quad (2.13)$$

Likewise, the following can form the ionospheric free phase measurement:

As $\Delta\rho_{P_1} = c\Delta t_{L_1}$,

$$\Delta\phi_{L_1} = -f_{L_1}\Delta t_{L_1} \quad \text{and} \quad \Delta\phi_{L_2} = -f_{L_2}\Delta t_{L_2} \quad (2.14)$$

leading to

$$\phi_{L_{3,1}} = \phi_{L_1} - \Delta\phi_{L_1} \quad \text{and} \quad \phi_{L_{3,2}} = \phi_{L_2} - \Delta\phi_{L_2} \quad (2.15)$$

and thus

$$\phi_{L_{3,1}} = \phi_{L_1} + f_{L_1}\Delta t_{L_1} \quad \text{and} \quad \phi_{L_{3,2}} = \phi_{L_1} + f_{L_1}\Delta t_{L_1} \quad (2.16)$$

using equation (2.7)

$$\phi_{L_{3,1}} = \phi_{L_1} + \frac{1}{c} \left(\frac{f_{L_1} f_{L_2}^2}{f_{L_1}^2 - f_{L_2}^2} \right) (\rho_{P_1} - \rho_{P_2}) \quad (2.17)$$

now using equation (2.10)

$$\phi_{L_{3,1}} = \phi_{L_1} + \frac{f_{L_1}}{c} (\rho_{P_3} - \rho_{P_1}) \quad (2.18)$$

and

$$\phi_{L_{3,2}} = \phi_{L_2} + \frac{f_{L_2}}{c} (\rho_{P_3} - \rho_{P_2}) \quad (2.19)$$

To convert the phase measurement to range units use

$$\rho_{L_i} = -\frac{c\phi_{L_i}}{f_{L_i}} \quad (2.20)$$

Figure 2.5 shows a plot of the dual frequency ionospheric corrections for the 4 Feb 1997 GPS/MET data. The solar flux (F10.7) for the 4 Feb 1997 is approximately 70. The benign solar flux environment contributes significantly to the low (3.93 m) mean of the ionospheric delay on this day. The elevation of the GPS satellites with respect to the OrbView-1 satellite is also shown on the plot in Figure 2.5 for the largest ionospheric corrections. Distinction between measurements taken while the OrbView-1 satellite is in the Sun (day) and in darkness (night) is also made on the plot. The difference in the mean between the day and night corrections is significant (2.79 m), as expected.

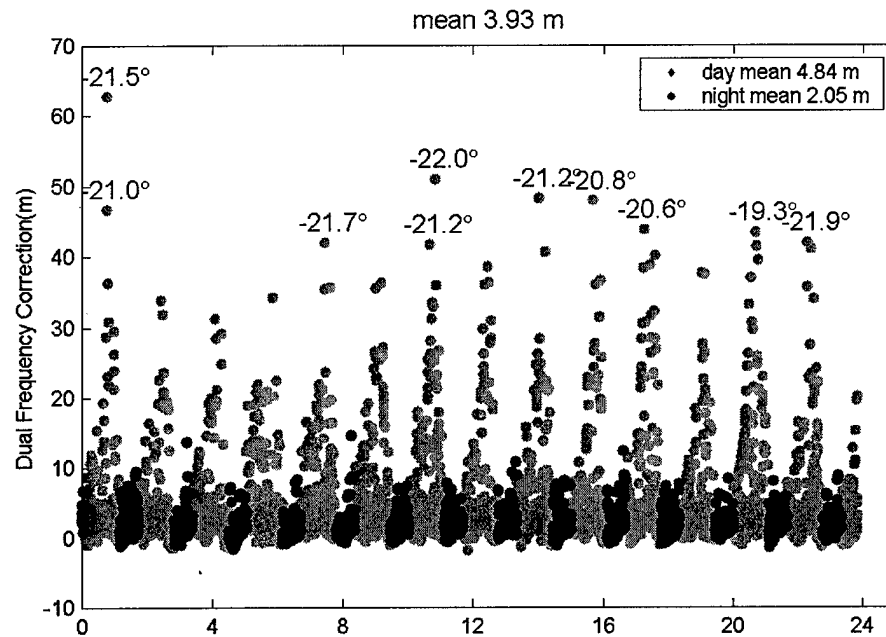


Figure 2.5 – GPS/MET Dual Frequency Ionospheric Delay Corrections

2.2.3.2 Interfrequency Bias

Another important consideration when using dual frequency GPS data is to correctly handle the GPS satellite interfrequency bias. Differences in the hardware signal paths of the L1 and L2 signals on board each GPS satellite create a space vehicle (SV) dependent group delay differential between L1 and L2 [44]. The L1-L2 interfrequency bias is broadcast in the navigation message and is designated with the variable T_{gd} . The T_{gd} correction is implemented for single frequency users because the broadcast clock correction coefficients are based on the effective code phase using dual frequency ionospheric corrections. Therefore, the single frequency user must adjust for this differential delay. GEODE does account for T_{gd} so it must be removed when processing dual frequency data.

Table 2.1 shows a comparison of the errors between GEODE and MicroCosm® POE when GEODE uses single and dual frequency measurements. Although the 3D RSS and mean of the radial error errors improved with use of the dual frequency ionospheric corrections, the mean of the in-track error changed by over 3 meters. One possible explanation is an unknown systematic error is introduced by the application of the dual frequency correction. There could be errors associated with the T_{gd} correction itself as JPL found errors in the initial broadcast T_{gd} values and began estimating new values for the Air Force to broadcast starting in 1999 [44]. Another possibly error source could be that the receiver interfrequency bias is not being accounted for adequately in the estimation of the receiver clock bias. No additional insight into the cause of the in-track error mean increase is found by comparing the measurement residuals in Table 2.2 or by looking at plots of the errors in Figure 2.6 and Figure 2.7. Qualitatively, it can be said that the precision of the GEODE estimate using dual frequency measurements is improved but nothing definitively can be said about its accuracy. The dual frequency GPS/MET ionospheric corrections will be used in Chapter 4 to compare GEODE results achieved with application of the Differenced Range Versus Integrated Doppler (DRVID).

Table 2.1 – GEODE GPS/MET Single Versus Dual Frequency Error Results

GPS/MET - 4 Feb 1997	Error Mean (m)			RMS Error (m)			
	R	I	C	R	I	C	3D
Single Frequency	0.55	-0.99	-0.10	2.74	10.24	2.15	10.81
Dual Frequency	0.11	2.04	-0.11	2.48	9.68	2.12	10.21

Table 2.2 - GEODE GPS/MET Single Versus Dual Frequency Measurement Residuals

GPS/MET 4 Feb 1997	Measurement Residual RMS (m)	Measurement Residual Mean (m)
Single Frequency	44.96	-0.11
Dual Frequency	44.60	-0.07

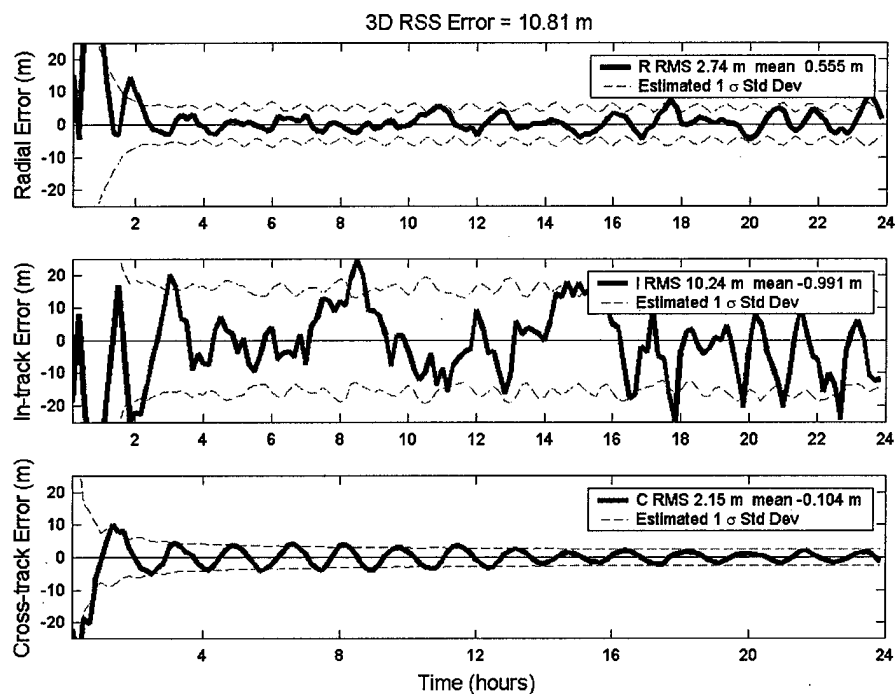


Figure 2.6 – GPS/MET Single Frequency Results

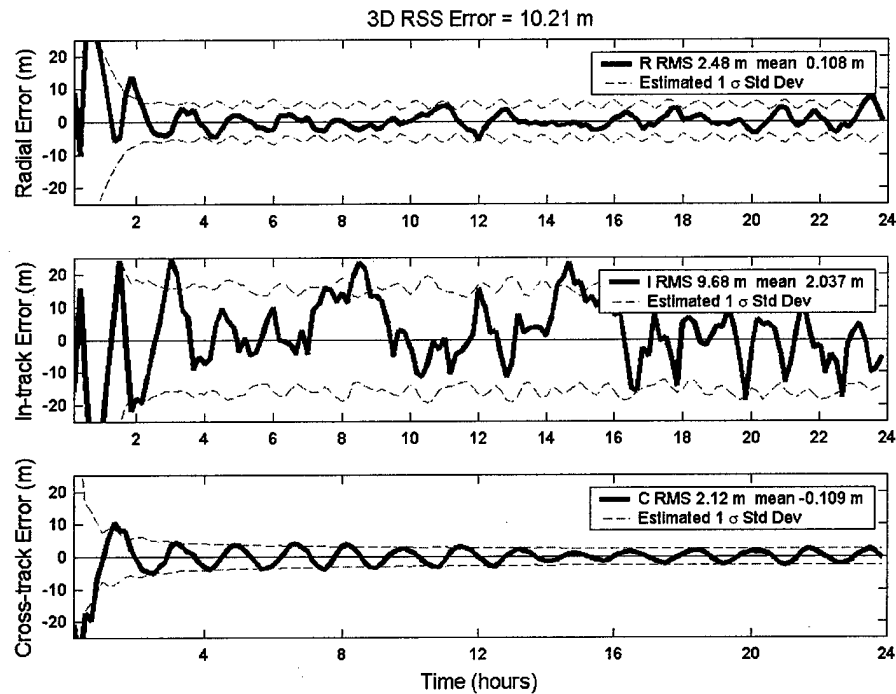


Figure 2.7 – GPS/MET Dual Frequency Results

2.2.4 Height Of Ray Path (HORP) Editing

GEODE uses a technique called HORP to edit out measurements that travel through the atmosphere [37]. HORP editing requires two user inputs contained in the uplink command file: atmosphere height, h , and maximum central angle, α_{\max} . h and α_{\max} are shown in Figure 2.8.

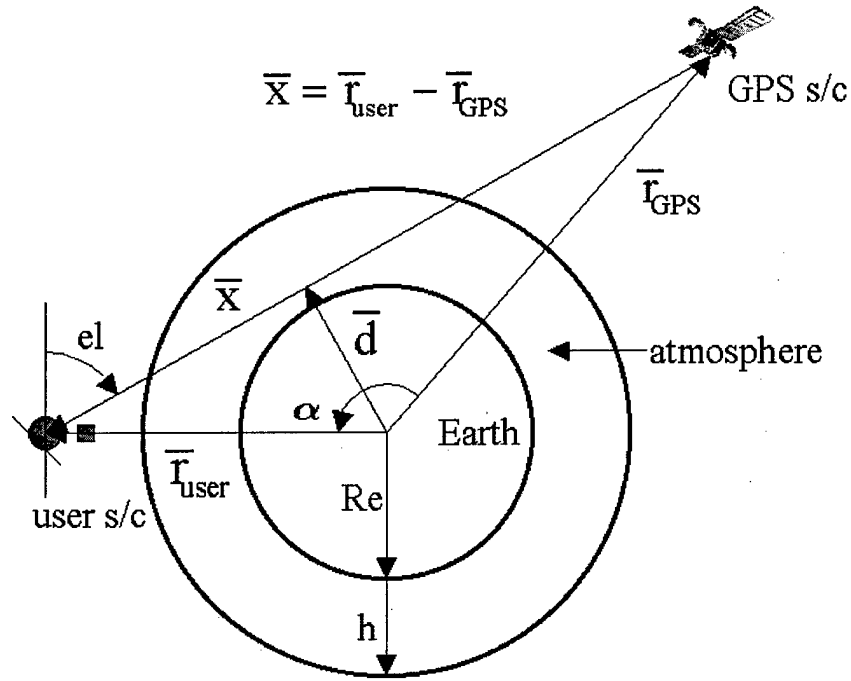


Figure 2.8 – HORP Editing

Measurements are edited out if $|\vec{d}| < R_E + h$ and $\alpha > \alpha_{max}$. Here

$$\alpha = \cos^{-1} \left(\frac{\vec{r}_{user} \cdot \vec{r}_{GPS}}{|\vec{r}_{user}| |\vec{r}_{GPS}|} \right) \quad (2.21)$$

and

$$\text{elevation} = \frac{\pi}{2} - \cos^{-1} \left(\frac{\vec{X} \cdot \vec{r}_{user}}{|\vec{X}| |\vec{r}_{user}|} \right) \quad (2.22)$$

If the input for h in the uplink command file is set to 0.0 then

$$h = |\vec{r}_{user}| - 15\text{km} \quad (2.23)$$

If h is set to 0.0 when processing GPS/MET data all measurements taken below approximately -3.72° elevation will be considered for editing. Again,

measurements will not be edited out unless $|\bar{d}| < R_E + h$ and $\alpha > \alpha_{\max}$. As

shown in Table 2.3, the value of α_{\max} can significantly affect GEODE's results.

Table 2.3 – GEODE GPS/MET Varying α_{\max} Results

GPS/MET - 4 Feb 1997		Mean Error (m)			RMS Error (m)			
α_{\max}^* (deg)	elevation	R	I	C	R	I	C	3D
70	4.6	0.12	4.11	-0.07	4.18	14.77	2.64	15.58
75	-0.5	0.12	4.11	0.07	4.18	14.77	2.64	15.58
80	-5.4	0.09	3.49	-0.08	4.46	15.41	2.64	16.26
85	-10.2	0.04	2.71	-0.14	4.15	13.35	2.62	14.23
90	-14.9	0.24	0.12	-0.13	3.81	11.71	2.30	12.52
95	-19.6	0.43	-1.90	-0.13	3.15	11.17	2.25	11.82
96	-20.5	0.42	-1.54	-0.11	3.11	11.04	1.99	11.64
97	-21.4	0.48	-1.06	-0.11	2.86	10.63	1.92	11.18
98	-22.3	0.54	-1.12	-0.12	2.94	10.96	2.42	11.61
99	-23.2	0.63	-1.34	-0.11	3.09	11.05	2.22	11.69
100	-24.1	0.55	-0.99	-0.10	2.74	10.24	2.15	10.81
101	-25.0	0.67	-1.94	-0.09	2.96	10.53	2.01	11.12
102	-25.9	0.66	-1.61	-0.09	3.08	10.53	2.01	11.15
103	-26.8	0.96	-3.18	-0.09	3.01	11.06	1.86	11.61
104	-27.7	0.99	-3.71	-0.09	2.99	11.27	2.07	11.85
105	-28.5	0.99	-3.71	-0.09	2.99	11.27	2.07	11.85

* α_{\max} is nominally set to 70°

** $h = 0.0$ implies 15km below the satellite altitude of ≈ 747 km

2.2.5 Polar Motion and $\Delta UT1$

In determining the transformation matrices between the Earth Centered Inertial (ECI) mean of J2000 coordinate system and an Earth Centered Earth Fixed (ECEF) coordinate system, two parameters are used which require prediction, and therefore, are challenging to implement in a real-time filter flown on board a satellite. The two parameters are the pole location (polar motion) and the difference between the UT1 and UTC time systems.

2.2.5.1 Polar Motion

Polar motion takes into account the fact that the celestial ephemeris pole, which is normal to the true equator, is in motion with respect to the terrestrial reference frame. In other words, the rotational pole moves within the Earth. The maximum amplitude of polar motion is 0.3 arc seconds or approximately 9 m on the surface of the Earth [45]. Polar motion consists largely of two motions, an annual elliptical component with a period of 365 days and a Chandler circular component with a period of about 435 days [46]. The motion is difficult to predict and is determined by observations.

The coordinates of the Earth's instantaneous pole location are measured by the International Polar Motion Service (IPMS) in terms of x_p and y_p components in the polar plane. x_p is measured along the Greenwich meridian and y_p is measured along the 90° W meridian. Past values of x_p and y_p are published in the International Earth Rotation Services Final Bulletin found at:

<ftp://maia.usno.navy.mil/ser7/finals.all>

A plot of x_p and y_p from May 1976 to May 2000 are shown in Figure 2.9.

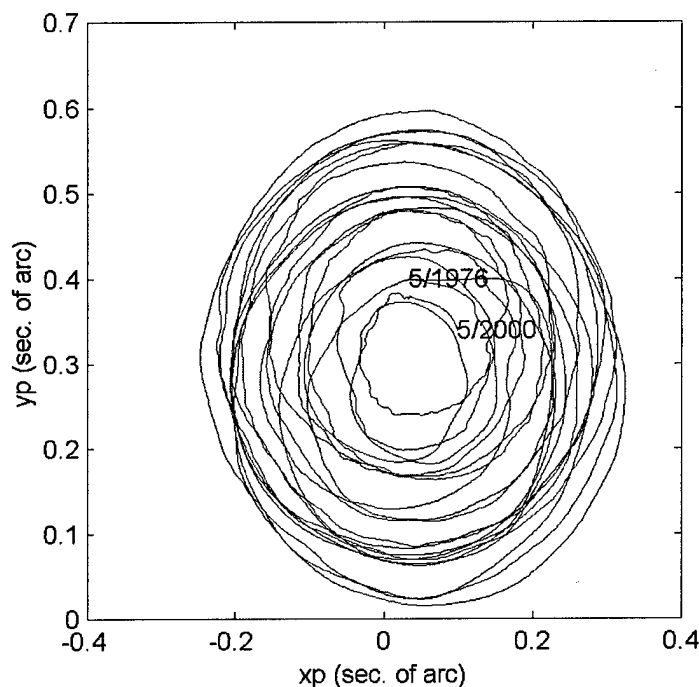


Figure 2.9 - Polar Motion Plot

The United States Naval Observatory (USNO) also supplies polar motion predictions published in the International Earth Rotation Service (IERS) Bulletin-A. The estimated accuracy of the predictions is 0.005 arc-second for the 40-day predictions [37]. The predicted values of x_p and y_p are obtained by evaluating the following trigonometric functions for the day of interest:

$$x_p = a_1 + a_2 \cos A + a_3 \sin A + a_4 \cos B + a_5 \sin C \text{ (arc-seconds)} \quad (2.24)$$

$$y_p = a_6 + a_7 \cos A + a_8 \sin A + a_9 \cos B + a_{10} \sin C \text{ (arc-seconds)} \quad (2.25)$$

where

$$A = \frac{2\pi}{365.25} (\text{MJD} - T_p) \text{ (radians)} \quad (2.26)$$

$$C = \frac{2\pi}{435} (\text{MJD} - T_p) \text{ (radians)} \quad (2.27)$$

MJD \equiv Modified Julian Date = JD of interest – 2500000.5 days

$T_p \equiv$ epoch of the prediction

The 10 coefficients are published in the IERS Bulletin-A found at:

<http://hpiers.obspm.fr/iers/bul/bula/bulletinA>

The effect of not including polar motion in GEODE depends on the size of the pole wander. The results in Table 2.4 show the effects on GEODE's position estimates with and without polar motion when GPS/MET data is processed. The comparison is again made against one day of MicroCosm® POE.

Table 2.4 – GEODE GPS/MET Results With and Without Polar Motion

GPS/MET - 4 Feb 1997	Mean Error (m)			RMS Error (m)			
	R	I	C	R	I	C	3D
With Polar Motion	0.55	-0.99	-0.10	2.74	10.24	2.15	10.81
Without Polar Motion	0.65	-0.99	-0.12	2.98	13.05	3.16	13.76

2.2.5.2 Δ UT1

The calculation of the Greenwich Hour Angle (GHA) requires Greenwich Sidereal Time (GST), which uses the UT1 time system. UT1 is a time scale measured by the rotation of the Earth. UTC is the time scale used worldwide for technical and scientific activities and is a compromise between highly stable atomic time and irregular Earth rotation. The current practice is to keep the difference between UT1 and UTC less than 0.9 seconds by adjusting UTC by

integer leap seconds. The USNO distributes the UT1-UTC prediction known as ΔUT1 in the IERS Bulletin-A. ΔUT1 is calculated by the following equation as presented in the IERS Bulletin-A:

$$\Delta\text{UT1} = u_1 + u_2 (\text{MJD} - T_{\text{UT1}}) + u_3 (\text{MJD} - T_{\text{UT1}})^2 \text{ (seconds)} \quad (2.28)$$

where

$\text{MJD} \equiv \text{Modified Julian Date} = \text{JD of interest} - 2500000.5 \text{ days}$

$T_{\text{UT1}} \equiv \text{MJD of the epoch of prediction}$

The estimated accuracy of the ΔUT1 prediction is 0.0048 seconds for a 40 day prediction. The effect of not including ΔUT1 in GEODE is far more significant than not including polar motion. See Table 2.4 and Table 2.5.

Table 2.5 – GEODE GPS/MET Results With and Without ΔUT1

GPS/MET - 4 Feb 1997	Mean Error (m)			RMS Error (m)			
	R	I	C	R	I	C	3D
With ΔUT1	0.55	-0.99	-0.10	2.74	10.24	2.15	10.81
Without ΔUT1	1.68	25.80	-0.9	4.37	28.96	59.73	66.53

2.2.6 All in View Versus Cyclic

GEODE has the capability to process measurements from all GPS satellites in view or to process the measurements from only one satellite at a given observation epoch. The keywords associated with these different processing schemes in the uplink command file are ALL for all in view and CYCLIC for processing only one observation at each observation epoch. The reason the

CYCLIC option is implemented is SA. Since the effects of SA are time correlated it is thought that by spacing the processing of GPS observations at the same period as the correlation in SA, the SA errors would appear more random [4]. Therefore, a time variable is also included in the uplink command file known as minimum sampling frequency. This minimum sampling frequency is nominally set at the correlation time of SA (3-5 minutes) [37]. In reality, tuning the minimum sampling frequency yields significant changes in GEODE's estimates. Table 2.6 shows a comparison of GEODE results when processing all in view versus cyclic. Table 2.7 shows results of tuning the minimum sampling frequency. An additional advantage to only processing one GPS measurement at each observation epoch is reduced computational burden since measurements from a minimum of 5 and a maximum of 8 GPS satellites are available at each observation epoch. The CYCLIC scheme is used throughout this dissertation as no accuracy / precision improvement is shown when processing all GPS satellites in view, even with SA free data.

Table 2.6 – GEODE GPS/MET ALL vs. CYCLIC Comparison

GPS/MET - 4 Feb 1997	Mean Error (m)			RMS Error (m)			
	R	I	C	R	I	C	3D
CYCLIC - *110	0.55	-0.99	-0.10	2.74	10.24	2.15	10.81
ALL	1.68	-4.48	-0.08	4.38	13.94	2.05	14.76

* 110 is the minimum sampling frequency in seconds

Table 2.7 – GEODE GPS/MET Min Sampling Frequency Tuning Results

GPS/MET - 4 Feb 1997 min sampling frequency	Mean Error (m)			RMS Error (m)			
	R	I	C	R	I	C	3D
10 (sec)	0.67	-2.26	-0.06	3.36	11.53	1.77	12.14
20	0.61	-1.87	-0.09	2.99	10.77	1.98	11.35
30	0.60	-1.70	-0.10	3.03	10.83	2.17	11.45
40	0.60	-1.70	-0.10	3.03	10.83	2.17	11.45
50	0.62	-2.27	-0.09	3.01	10.75	1.93	11.33
60	0.61	-1.82	-0.09	2.93	10.67	2.00	11.24
70	0.66	-1.84	-0.09	3.07	10.98	2.07	11.59
80	0.61	-1.52	-0.10	2.70	10.44	2.03	10.97
90	0.65	-1.67	-0.10	2.85	10.43	2.15	11.03
100	0.62	-2.04	-0.10	3.09	11.06	2.25	11.70
110	0.55	-0.99	-0.10	2.74	10.24	2.15	10.81
120	0.68	-1.88	-0.08	3.22	10.83	1.77	11.43
130	0.63	-1.88	-0.10	3.16	10.46	2.31	11.17
180	0.49	-0.98	-0.09	3.16	10.10	2.76	10.94
240	0.50	-0.45	-0.06	3.98	12.18	2.80	13.12
300	0.27	-0.02	-0.12	4.48	15.09	3.06	16.04

2.2.7 Antenna Phase Center Offset From Satellite Center of Gravity (CG)

Since the phase center of a GPS antenna may not be coincident with the CG of the satellite it is important to account for this offset when computing the predicted measurement. As reported earlier, the phase center of the GPS/MET antenna is offset from the OrbView-1 CG by

- 0.507 m in the x direction
- 0.039 m in the y direction
- 0.178 m in the z direction [19]

The OrbView-1 satellite's attitude is maintained with 5–10° accuracy. Since a 10° attitude error translates to a maximum of a 4 cm error in x, y, or z, the offsets detailed above can be assumed to be fixed. Here, x is in the in-track direction, y is in the cross-track direction and z is in the radial direction. GEODE currently

has the capability to map the antenna phase center to the satellite's CG through a transformation from RIC coordinates to inertial coordinates. Obviously, a more rigorous approach would be to use accurate attitude information along with the above body fixed offsets to more precisely account for the offset in inertial space. Unfortunately, GEODE does not currently have this capability. Results are shown in Table 2.8 using no offset and the offset reported above. The 26 cm 3D RSS and over 1 m in-track bias improvements came with no additional computational burden as GEODE accounts for the offset even when it is zero.

Table 2.8 – GEODE GPS/MET Antenna Phase Center Mapping Results

GPS/MET - 4 Feb 1997			Mean Error (m)			RMS Error (m)			
Antenna Offset (m)			R	I	C	R	I	C	3D
0.0	0.0	0.0	0.63	-2.06	-0.10	2.70	10.54	2.03	11.07
0.178	-0.507	-0.039	0.55	-0.99	-0.10	2.74	10.24	2.15	10.81

2.2.8 Lagrange Interpolation of Precise GPS Ephemerides

The motivation for investigating the accuracy of precise GPS ephemerides compared to broadcast ephemerides is to determine the accuracy gained in satellite OD and the feasibility of using precise GPS ephemerides in a real-time OD scheme on board a satellite. Several organizations, JPL being one of them, produce GPS ephemeris predictions that are more accurate than those broadcast. Satellite OD in real-time can use either broadcast or predicted precise ephemerides. Obviously, post-processed precise ephemerides cannot be used in a real-time scenario. This section includes a comparison of broadcast and precise ephemerides, a comparison of GEODE interpolated ephemerides and ephemerides

interpolated using an International GPS Service (IGS) executable (reported accuracy of this interpolator is at the mm level), a comparison of Lagrange interpolated ephemerides and IGS ephemerides and finally the Lagrange interpolation algorithm.

2.2.8.1 Broadcast Versus Precise GPS Ephemerides

The first comparison is between broadcast and precise ephemerides for GPS PRN01 on 2 Feb 1997. Zumberge [24] reports broadcast ephemerides are accurate to 5 to 10 meters. Figure 2.10 shows a slightly smaller 3D RSS position error of 3.71 m, however, only 4 hours of data are plotted. The time bias error in the lower of the two plots in Figure 2.10, is the difference between the broadcast GPS clock correction and the correction supplied with the precise ephemerides. The large step decrease in the bias error at the two-hour point is due to switching to a new set of broadcast ephemerides.

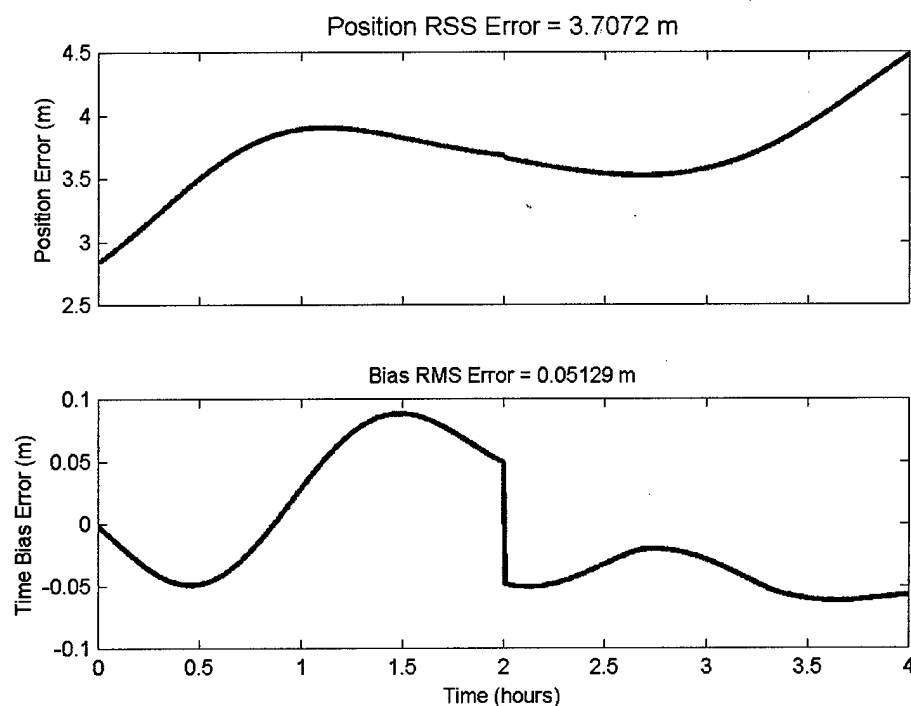


Figure 2.10 - Broadcast vs. Precise Ephemeris PRN01 2 Feb 1997

2.2.8.2 GEODE Interpolation Versus Precise GPS Ephemerides

The next comparison is between GEODE's interpolation of precise ephemerides and interpolation done by the IGS software. "Truth" data is generated using the IGS software and output at 1-second intervals. GEODE's interpolator is then used to interpolate between 5-min, 15-min and 30-min interval data, simulating the uplink of a set of precise ephemerides. The 30-min interval data would be the best choice since it requires the least uplink overhead. Figure 2.11 shows the results of GEODE's interpolator using precise ephemerides at a 5-min interval. It is not known what causes the excursion at the start of the position error plot. Figure 2.12 shows the results of GEODE's interpolator with 15-minute interval precise ephemerides. GEODE's interpolator is not

documented in the Mathematical Specification so it is difficult to ascertain the cause of the excursions and larger error. The 15-minute interval GPS ephemerides could not be used due to the large errors.

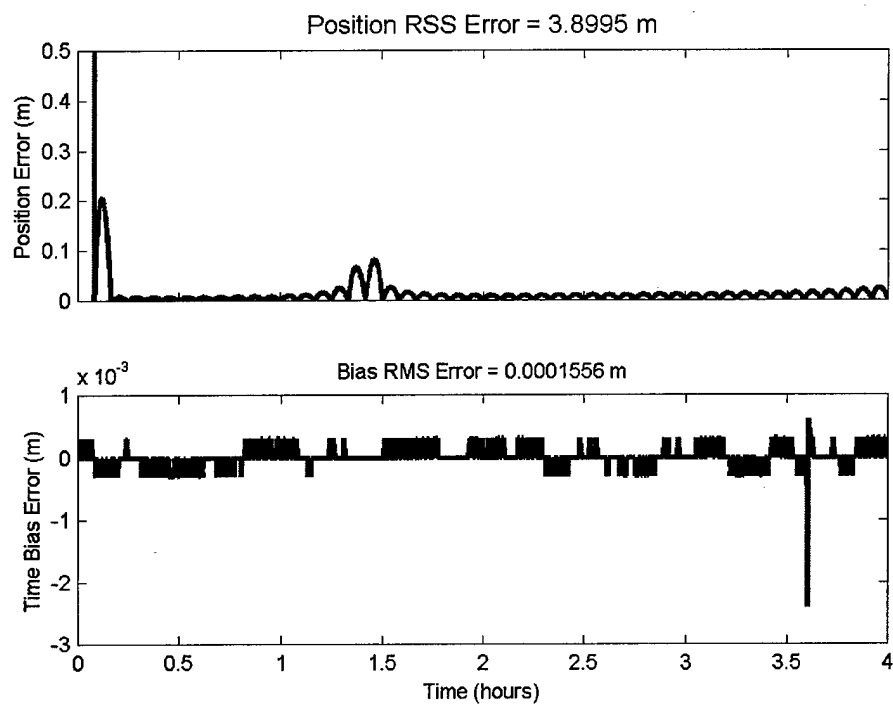


Figure 2.11 - GEODE Interpolator with 5-Minute Interval Ephemeris

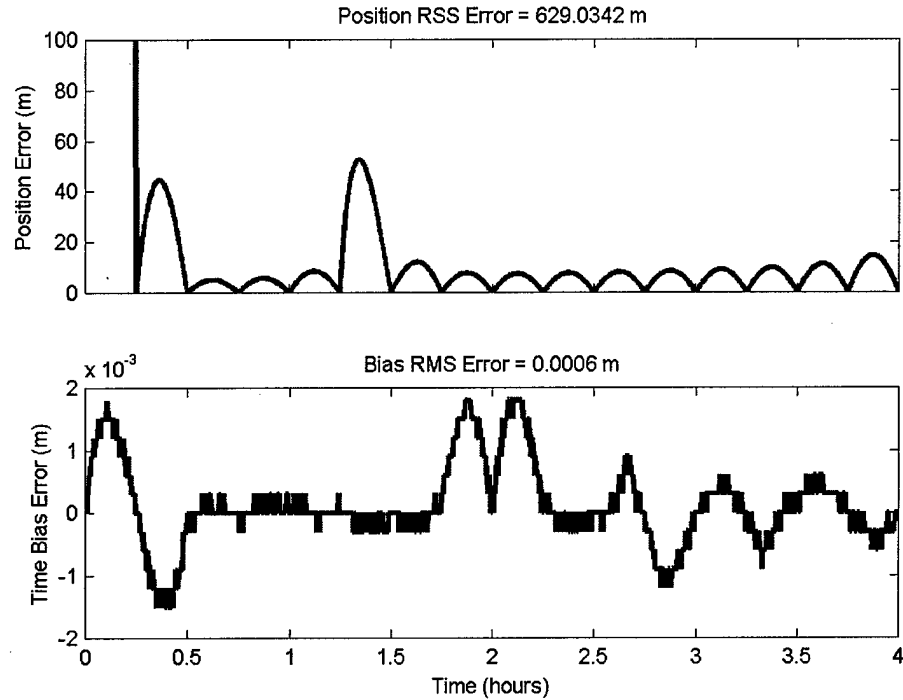


Figure 2.12 – GEODE Interpolator with 15-Minute Interval Ephemeris

2.2.8.3 Lagrange Interpolation Versus Precise GPS Ephemerides

Next, a Lagrange interpolation scheme is used and the results compared to the IGS interpolation. The best results are attained using the 5-minute ephemeris interval but the result achieved with the 12th order interpolation and 30-minute interval is the best balance of accuracy, upload minimization and reduced computational burden. It is interesting to note that the Lagrange interpolation performed worse using 17th order than 12th order. Figure 2.13 shows the 12th order Lagrange interpolation using 30-minute interval data and Figure 2.14 shows

the 17th order interpolation using 30-minute interval data. A summary of the results for each of the above methods is shown in Table 2.9.

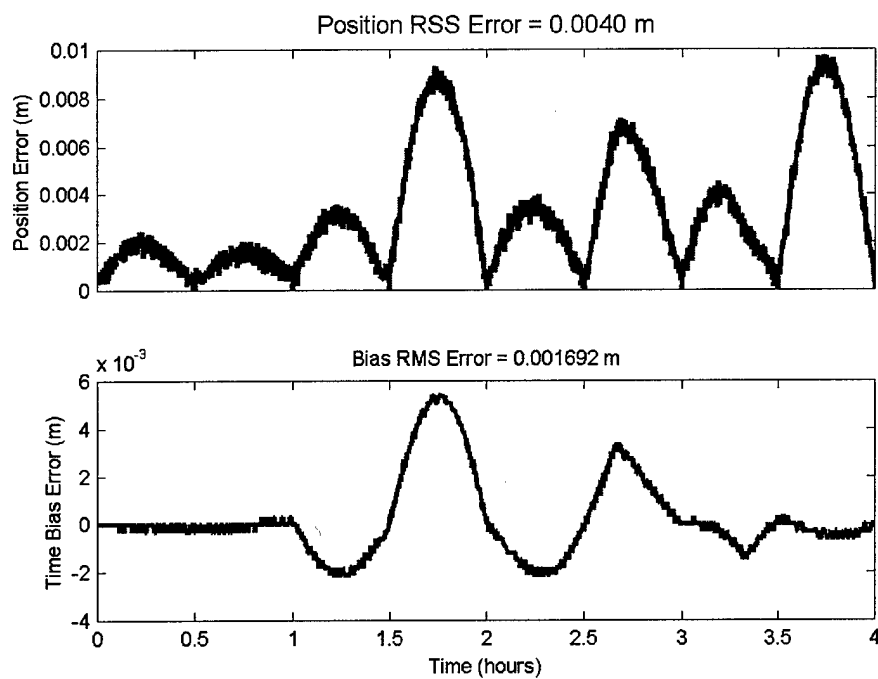


Figure 2.13 - Lagrange with 30-Minute Interval and 12th Order Interpolation

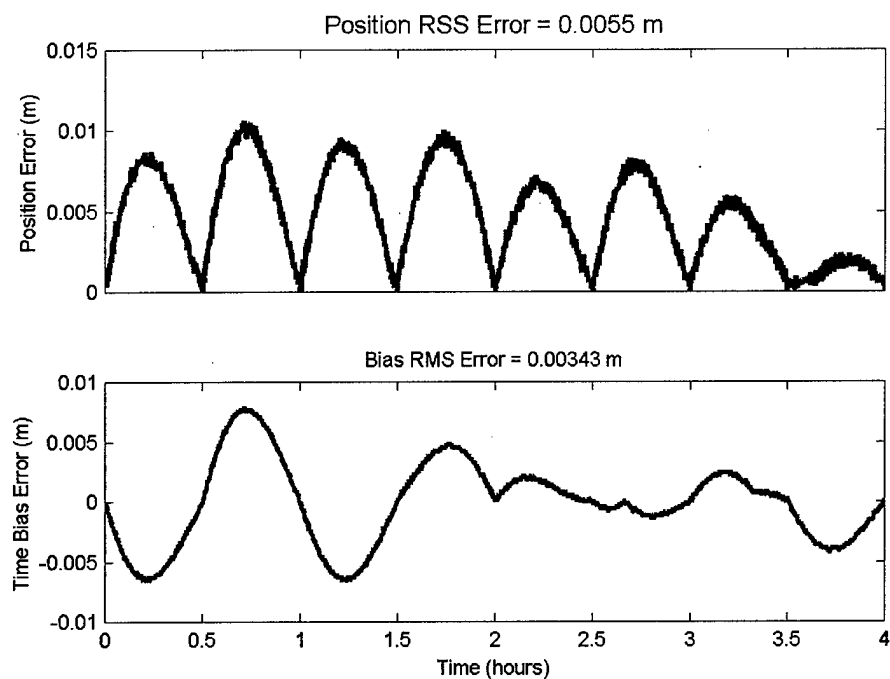


Figure 2.14 - Lagrange with 30-Minute Interval and 17th Order Interpolation

Table 2.9 - Statistics of Results

Method	Ephemeris Interval (min)	Interpolation Order	RSS of Range Error (meters)	RMS of Bias Error (meters)
Broadcast	n/a	n/a	3.7072	0.05129
GEODE	5	n/a	3.8995	0.0001556
GEODE	15	n/a	629.03	0.0006
Lagrange	30	12	0.0040	0.001692
Lagrange	30	17	0.0055	0.00343

2.2.8.4 Precise Ephemerides Interpolation Conclusions and Lagrange Algorithm

The conclusion drawn from these results is that the GEODE interpolator needs to be replaced. It produces inconsistent results and it requires ephemerides closely spaced in time. The Lagrange interpolation scheme performs more consistently, is much more accurate with ephemerides at lower frequency and its

computational burden is smaller than GEODE's. Below find the algorithm used for Lagrange interpolation borrowed from Hofmann-Wellenhof [17].

Assume functional values $f(t_j)$ are given at epochs $t_j, j = 0, 1, \dots, n$. Where n is the order of the interpolation. Here $f(t_j)$ are the GPS satellite x, y, z position values and the GPS clock bias values. Then,

$$l_j(t) = \frac{(t-t_0)(t-t_1)\dots(t-t_n)}{(t_j-t_0)(t_j-t_1)\dots(t_j-t_n)} \quad (2.29)$$

The interpolated value at epoch t follows from the summation

$$f(t) = \sum_{j=0}^n f(t_j) l_j(t) \quad (2.30)$$

The implementation of the algorithm shown above in GEODE is:

Given: GPS ephemeris (x_i, y_i, z_i) and bias _{i} at times $t_i \quad i = 1$ to n
Find: GPS ephemeris (x, y, z) and bias at time T

```

x = 0  y = 0  z = 0  bias = 0

i = 1 to n
    li = 1
    ti = time of ephemeris at time i
    j = 1 to n
        if i ≠ j
            tj = time of ephemeris at time j
            li = li * (T - tj) / (ti - tj)
        end if
    end j
    x = x + li * xi
    y = y + li * yi
    z = z + li * zi
    bias = bias + li * biasi

end i

```

2.2.8.5 GEODE Results Using Precise GPS Ephemerides

There is only a marginal improvement in GEODE's position estimates, compared to MicroCosm® POE, when precise GPS ephemerides are used instead of those broadcast. Table 2.10 shows a comparison of the results using GPS/MET data. The minimal improvement is most likely due to SA. SA can cause tens of meters of error in the pseudorange measurement and is such a dominating error source it swamps the errors introduced by using broadcast ephemerides.

Table 2.10 – GEODE GPS/MET Results Using Precise GPS Ephemeris

GPS/MET - 4 Feb 1997				RMS Error (m)			
	R	I	C	R	I	C	3D
Broadcast Ephemeris	0.55	-0.99	-0.10	2.74	10.24	2.15	10.81
Precise Ephemeris	0.58	-1.05	-0.09	2.99	10.11	1.97	10.73

Table 2.11 shows results of processing GEODE on SA free T/P data from 5 May 2000. Here the GEODE solution is compared to POE generated by JPL. While the improvement on the GPS/MET data is only 0.74%, the improvement to the T/P data is 10.0%. Therefore, it is concluded that in the presence of SA using precise GPS ephemerides is unnecessary while in the absence of SA, using precise GPS ephemerides may be a viable method of improving OD accuracy.

Table 2.11 – GEODE T/P Results Using Precise GPS Ephemeris

T/P – 5 May 2000				RMS Error (m)			
	R	I	C	R	I	C	3D
Broadcast Ephemeris	0.21	-0.04	0.01	0.35	1.06	0.44	1.20
Precise Ephemeris	0.22	-0.16	0.00	0.34	0.97	0.31	1.08

2.2.9 JPL High-Rate GPS Clock Estimates

In order to assess GEODE's accuracy with SA off, data with SA free measurements are needed. The T/P data mentioned in the previous section can be used but at the T/P altitude (1336 km), ionospheric effects are smaller and the satellite's dynamic environment is more benign. GPS/MET, on the other hand, is lower (750 km altitude) and thus experiences larger measurement errors due to ionosphere and a more challenging dynamic environment. Unfortunately, there are no periods during the GPS/MET mission when SA is off. Therefore, high rate GPS clock estimates produced by JPL using GOA II are used instead of the broadcast or precise GPS clock estimates [47]. The high rate clock estimates are found at:

ftp://sideshow.jpl.nasa.gov/pub/gipsy_products/hrclocks/

2.2.9.1 JPL High-Rate GPS Clock Estimate Challenges

There are several challenges in using the JPL high rate GPS clock estimates. There are sporadic time periods, for different GPS satellites, when the high rate clock estimates are not available. Figure 2.15 shows two several hour-long periods where the high rate estimates are not available. The 3 Feb 1997 GPS/MET data has only 7 out of 25 GPS satellites without gaps. The typical gap length is 2-3 hours.

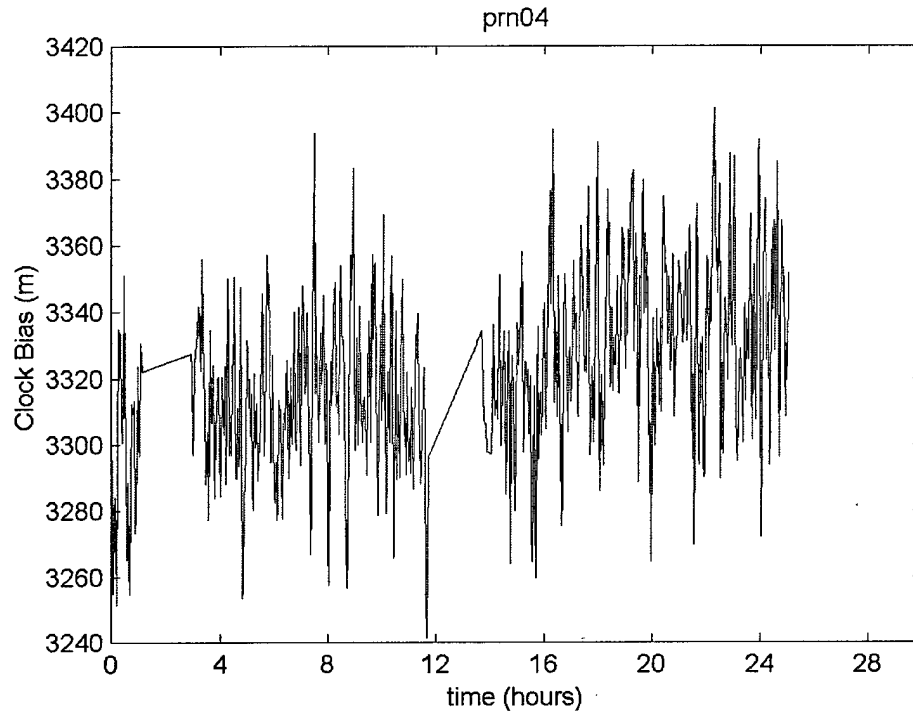


Figure 2.15 – High Rate Clock Corrections for PRN 4 on 3 Feb 1997

Another challenge of using the high rate clock estimates is there are discontinuities from one day to the next due to changes in the reference ground clocks used to generate the estimates [47]. Also, satellite clock estimates available on one day may not be available the next day. Fortunately, each 24-hour arc uses the same reference ground clock and usually satellites are not dropped during a 24-hour arc.

A final item of interest is a bias between the broadcast clocks and the high rate clocks. As seen in Figure 2.16 and Figure 2.17, the high rate GPS clock estimates from 3-5 Feb 1997 are biased by 72.3 m for PRN 2 and 71.8 m for PRN 9. The bias is not constant over the course of a day and slowly increases

over time. The data for all other GPS satellites on these days have similar biases.

The bias between the broadcast clocks and the JPL high rate clocks is due to a bias between the reference ground clock used in the estimation of the JPL high rate clocks and GPS system time [48]. Fortunately, the bias is absorbed in the estimate of the receiver clock bias, since it is nearly constant for all satellites.

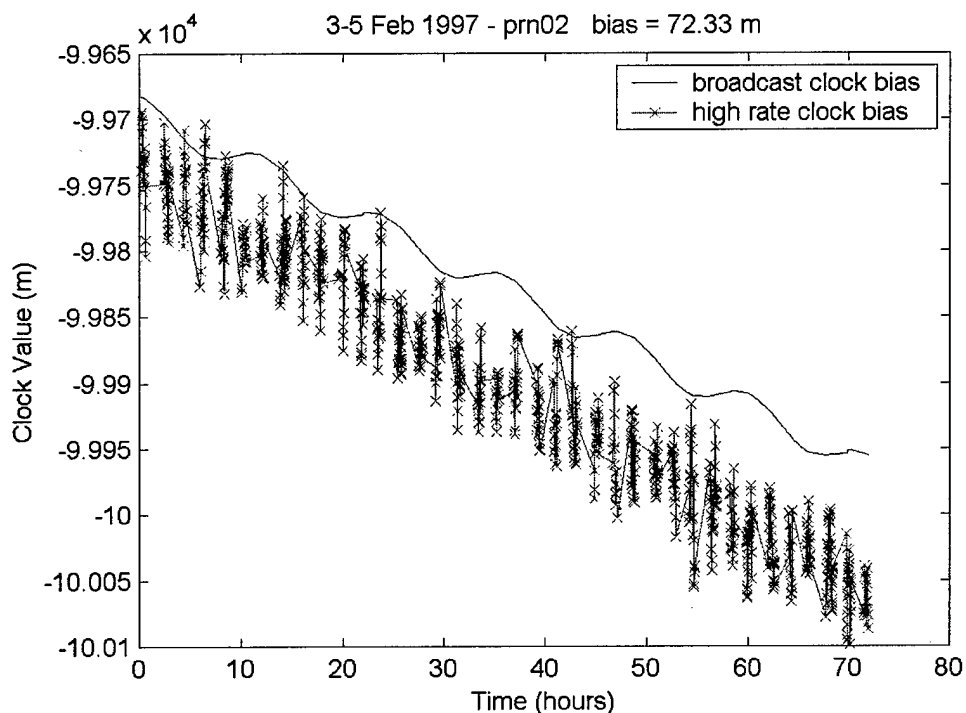


Figure 2.16 – Broadcast vs. High Rate Clock Biases for PRN 2

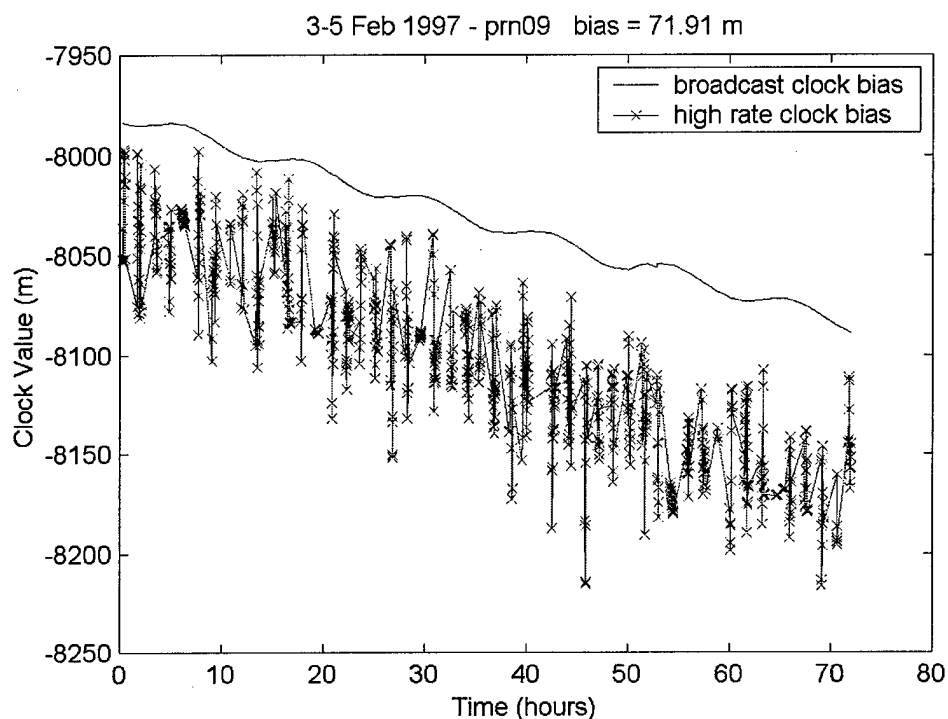


Figure 2.17 – Broadcast vs. High Rate Clock Biases for PRN 9

2.2.9.2 Application of JPL High Rate GPS Clock Estimates

While application of the JPL high rate clock estimates does not completely remove the effects of SA, due to the reasons mentioned above, it does provide a pessimistic indication of the results attainable with SA off. When processing the 4 Feb 1997 GPS/MET data, gaps in the high rate clock data are interpolated through and where data is not available for a GPS satellite, the satellite's measurement is not used. Table 2.12 shows results when the high rate GPS clock estimates are used instead of those broadcast for single and dual frequency and for precise and broadcast ephemerides. As expected, the case where the high rate

GPS clocks are used with dual frequency ionospheric correction and precise GPS ephemerides provide the most accurate and most precise results.

Table 2.12 – GEODE GPS/MET SA Off Results Comparison

GPS/MET - 4 Feb 1997	Error Mean (m)			RMS Error (m)			
	R	I	C	R	I	C	3D
Single Frequency							
Broadcast Clock Biases Broadcast GPS Ephemerides	0.55	-0.99	-0.10	2.74	10.24	2.15	10.81
Broadcast Clock Biases Precise GPS Ephemerides	0.58	-1.05	-0.09	2.99	10.11	1.97	10.73
High Rate Clock Biases Broadcast GPS Ephemerides	0.28	-3.59	-0.04	2.22	7.23	0.77	7.60
High Rate Clock Biases Precise GPS Ephemerides	0.30	-3.56	-0.03	2.31	6.95	0.74	7.36
Dual Frequency							
Broadcast Clock Biases Broadcast GPS Ephemerides	0.11	2.04	-0.11	2.48	9.68	2.12	10.21
Broadcast Clock Biases Precise GPS Ephemerides	0.11	2.01	-0.11	2.48	9.22	2.03	9.76
High Rate Clock Biases Broadcast GPS Ephemerides	-0.08	-1.38	-0.04	2.10	6.14	0.86	6.55
High Rate Clock Biases Precise GPS Ephemerides	-0.06	-1.35	-0.03	1.91	5.43	1.04	5.85

2.3 SA Free T/P Data

Another data set used in the research performed for this dissertation is from the T/P satellite (collected on 5 May 2000). Again, SA was turned off on 2 May 2000. Additional information regarding T/P can be found at:

<http://topex-www.jpl.nasa.gov/>

While the dynamic environment and ionospheric effects on T/P (1336 km altitude) are more benign than those at lower altitudes, SA free T/P data is also used to gauge GEODE's performance.

Figure 2.18 shows plots of the radial, in-track and cross-track errors between GEODE's position estimates for T/P and JPL's POE. The 1.2 m 3D RSS error is a significant improvement over the GPS/MET results (6.55 m 3D RSS) with high rate GPS clock estimates used to reduce the effects of SA. Another indication of the significance of SA being turned off is the measurement residual plot in Figure 2.19. A comparison between a plot of the measurement residuals for the GPS/MET data with high rate GPS clock estimates applied (shown in Figure 2.20) and the T/P measurement residuals (shown in Figure 2.19) shows an order of magnitude difference. The T/P measurement residual RMS is 3.3 m while the GPS/MET measurement residual RMS is 31.5 m. Table 2.13 shows a summary of T/P results with and without precise GPS ephemerides. Improvement to GEODE will be gauged in this dissertation by processing both GPS/MET and T/P data.

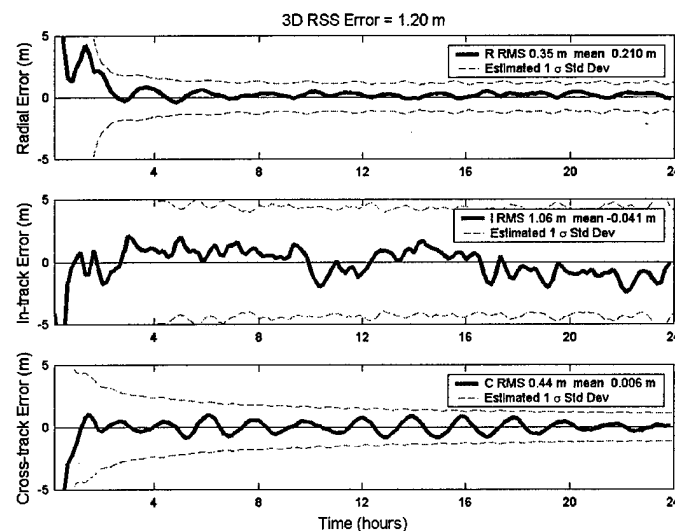


Figure 2.18 – GEODE SA Free T/P Results

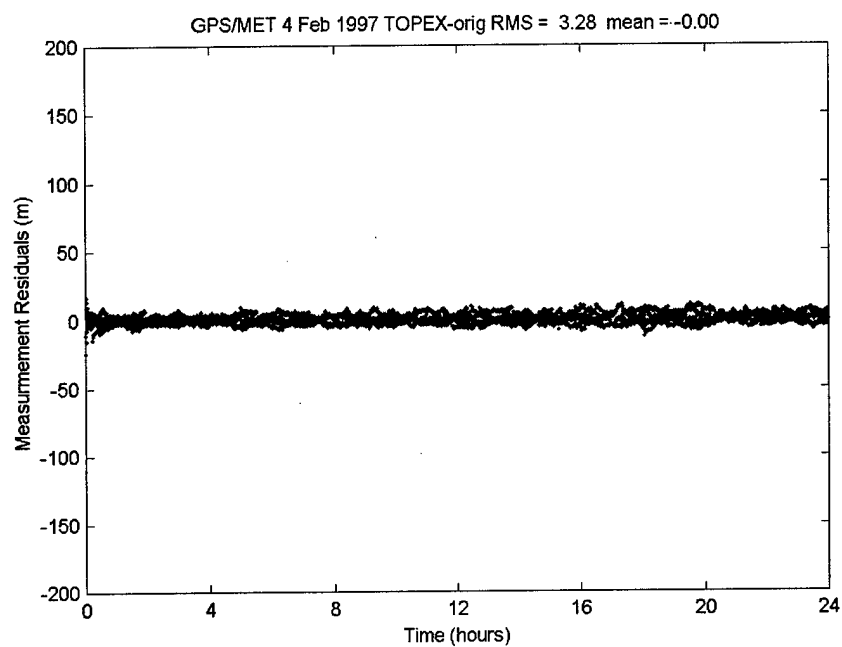


Figure 2.19 – T/P Measurement Residuals

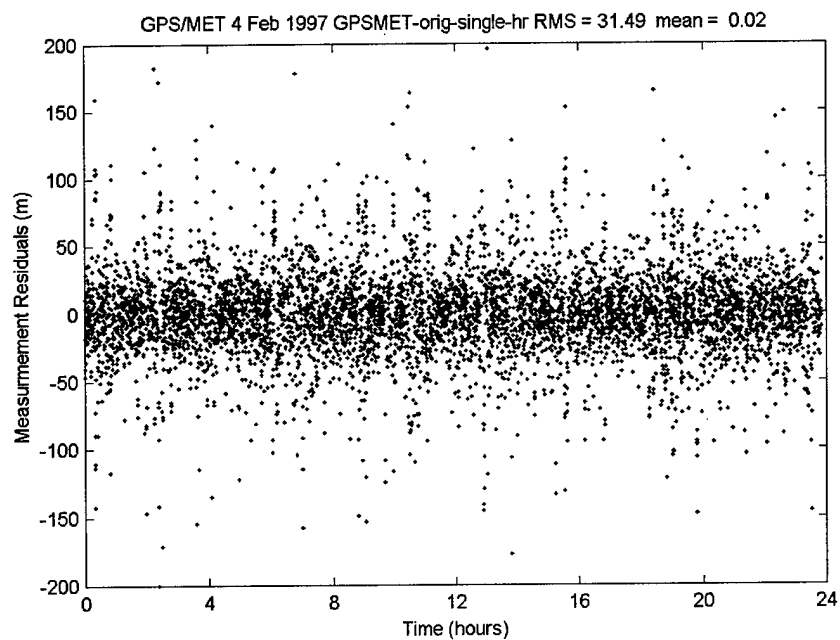


Figure 2.20 – GPS/MET with High Rate GPS Clock Estimates - Measurement Residuals

Table 2.13 – SA Free T/P Results with GEODE

5 May 2000	Error Mean (m)			Error RMS (m)			
	R	I	C	R	I	C	3D
T/P	0.21	-0.04	0.01	0.35	1.06	0.44	1.20
TOEX with Precise GPS Ephemerides	0.22	-0.16	0.00	0.34	0.97	0.31	1.08

2.4 Summary

The data collected by both the GPS/MET experiment on board the OrbView-1 satellite and T/P is extremely valuable in gauging the accuracy/precision of the real-time satellite OD software suite known as GEODE. Several GEODE processing schemes are investigated and results are presented for several modifications to GEODE that improve performance and provide insight into GEODE's abilities in an SA free GPS environment. Results presented in Table 2.12 and Table 2.13 will be used as a benchmark to compare results achieved with suggested improvements to GEODE in Chapters 3-6.

CHAPTER 3

Earth Gravity

Post-processing and near real-time Precise OD (POD) systems have the luxury of using state-of-the-art work stations or networked systems, while real-time systems are limited to the latest space qualified hardware. Unfortunately, the processing capability difference between ground computers and those found on satellites is significant. High-end flight computers have roughly the equivalent computational power of a 60 MHz Pentium I [49]. Therefore, on board OD systems must minimize the computational burden of their software while maximizing accuracy and autonomy. One area where computational burden can be reduced significantly, without overly decreasing accuracy, is the degree and order of the gravitational acceleration model used.

This chapter presents the results of an investigation into the effects on accuracy and computational burden of the degree and order of the gravity model used in propagating an orbit and in performing satellite OD. Since 20% of GEODE's computational time is spent evaluating gravitational accelerations, a method is also investigated to significantly reduce GEODE's computational burden by replacing spherical harmonic coefficient with an approximation method.

3.1 Model Size Integration Results and Computational Burden Estimates

The size (degree and order) of the gravity model used in propagating a satellite orbit from one time to the next significantly affects the accuracy of the propagation. But, as the degree and order of the gravity model increase, so does the computational burden on the computer used for the propagation. In performing real-time, autonomous satellite OD, it is highly desirable to minimize the computational burden while maximizing accuracy. The accuracy required by the integrator depends on the altitude of the satellite and the type of estimation filter used. The higher the satellite, the smaller the size of the gravity model needed to achieve the same accuracy. Figure 3.1 shows a comparison of accelerations calculated at various altitudes between a full 70x70 JGM-2 gravity model and truncated models. The trends, as expected, show decreasing accuracy with smaller models and lower altitude.

The filter type also affects the size of the gravity model needed. If the filter is a batch or batch-sequential, then the state is not measurement updated after each measurement is processed. Therefore, the integration time used in a batch or batch-sequential processor is typically a day or longer. On the other hand, an EKF updates the state every time a measurement is processed, thereby significantly reducing the integration time. In the case of processing the GPS/MET data, the measurements are 10 seconds apart so the integration time between measurements is only 10 seconds.

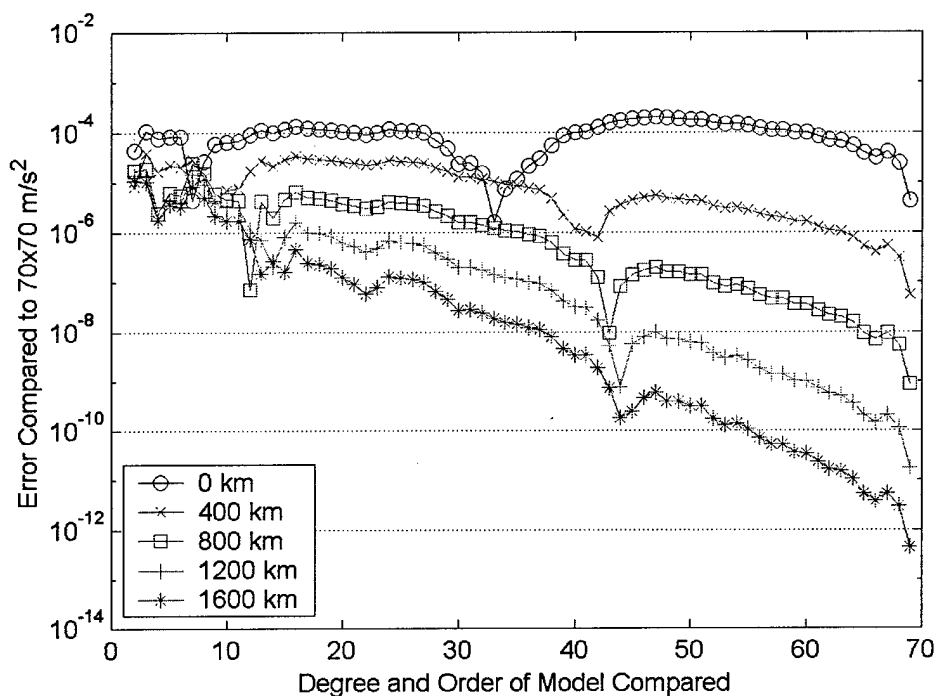


Figure 3.1 - Acceleration Accuracy Comparison of Various Size Gravity Models at Various Altitudes

To accurately assess the size of gravity model to be used in an on board EKF, the filter must be run with real or simulated data using various size gravity models. The position and velocity estimates are then compared to “truth” to assess accuracy.

Another method that can be used to guide the choice of the size of the gravity model used in real-time OD is to perform a one-day integration using an orbit similar to the satellite’s mission orbit. This process can be used to narrow the design space used for optimizing accuracy/precision versus computational burden. Table 3.1 shows a comparison between GPS/MET orbit propagations

performed with several truncations of the EGM-96 gravity model. The first column is the number of coefficients in the spherical harmonic coefficient expansion used to calculate the acceleration. The second column shows the number of Floating Point Operations (FLOPS) required in Matlab to calculate the non-spherical gravitational acceleration at one point. The third column shows the time required to propagate a low Earth, circular orbit for one full day using GEODE. Each of these estimates of computational burden are roughly proportional, as expected. The final column shows the 3D RSS error of the truncated models compared to the full 70x70.

The initial conditions for the propagation using the 70x70 gravity model are shown in Table 3.1. The initial conditions of the propagations performed with truncated gravity models are adjusted to provide the best fit to the 70x70 model.

Table 3.1 - Computational Burden and Accuracy of Various Truncations of the EGM-96 Gravity Model

Model Size	Number of Coefficients	Number of Matlab Flops	GEODE Integration Time (sec)	EGM-96 RSS Error Compared to 70x70 (m)
5x5	36	528	51.5	91.80
10x10	126	1553	52.1	31.40
20x20	456	5103	55.8	6.13
30x30	986	10653	64.8	1.61
40x40	1716	18211	68.1	0.61
50x50	2646	27761	77.9	0.13
70x70	5106	52853	98.0	N/A

Table 3.2 – Initial Conditions of Propagation With EGM-96 70x70 Gravity Model

Osculating Elements	
a	7122.463 km
e	0.00143
i	70.00°
Ω	196.54°
ω	233.66°
U	2.47°

The purpose of Table 3.1 is to show the computational burden required and propagation accuracy attainable with truncations of the EGM-96 model. As shown in Table 3.1, there is only a 4.5 m difference in accuracy between the 20x20 truncation and the 30x30 truncation but over a 16% computational burden difference. With knowledge of the accuracy attainable with various truncations the next step is to compare OD accuracy.

3.2 GEODE Results and Computational Burden Changes with Various Gravity Model Truncations

There is a moderate improvement in the 24-hour propagation accuracy between a 20x20 truncation and a 30x30 truncation (roughly 4.5 m) at the GPS/MET altitude and inclination. This section presents a comparison of the GEODE OD accuracy and computational burden using various truncations of the JGM-2 and EGM-96 models. Table 3.3 presents the JGM-2 Earth gravity state noise correlation times generated with Fortran 77 code produced by GSFC called autocor4.for (see Section 2.2.2). Table 3.4 shows GEODE's results with various truncations of the JGM-2 gravity model using the data in Table 3.3.

There is only a one-meter difference in OD accuracy between the 20x20 truncation and the higher order truncations. The best results are obtained using the 26x26 truncation. It is also interesting to note that although there is only a one-meter accuracy improvement from the 20x20 truncation to the 30x30 truncation, there is an 11% difference in the processing time. In general, the accuracy and precision increase as the degree and order of the gravity model increase.

The EGM-96 Earth gravity state noise correlation times are listed in Table 3.5 and the GEODE results are listed in Table 3.6. GEODE performed similarly with both gravity models. A comparison between the 3D position error RSS for both the JGM-2 and EGM-96 models can be seen graphically in Figure 3.2. The conclusion from these results is that a 30x30 gravity model provides the best balance of accuracy, precision and computational burden. Next a method will be presented to replace GEODE's current method of calculating Earth gravity in an attempt to maintain or improve accuracy and precision while reducing the computational burden.

Table 3.3 – Earth Gravity JGM-2 State Noise Correlation Times

autocor4.for	Direction		
	R	I	C
5x5	386.2048	24.5966	754.0956
10x10	211.0938	4.5542	420.7908
20x20	136.1409	0.1918	271.4699
21x21	132.9159	0.2454	264.8726
22x22	129.8031	0.1773	258.6294
23x23	127.0829	0.2589	253.0201
24x24	124.4671	0.2155	247.7713
25x25	122.0885	0.1718	242.9791
26x26	119.9174	0.1766	238.5807
27x27	117.9191	0.1658	234.5325
28x28	116.1295	0.1952	230.8798
29x29	114.4664	0.1525	227.5483
30x30	112.9898	0.15918	224.5475
40x40	104.9078	0.1340	208.1667
50x50	102.8627	0.1311	204.0012
70x70	102.4124	0.1301	203.0799

Table 3.4 – GEODE GPS/MET JGM-2 Comparison

GPS/MET 4 Feb 1997		Mean Error (m)			RMS Error (m)			
Gravity Model	Run Time (sec)	R	I	C	R	I	C	3D
05x05	60.0	1.71	-5.57	-0.06	25.42	53.87	29.42	66.43
10x10	64.0	0.54	-2.03	0.62	7.66	18.16	7.15	20.96
20x20	64.4	0.52	-0.97	0.02	3.12	11.05	2.93	11.85
22x22	68.7	0.66	-1.14	0.05	2.90	10.53	2.26	11.15
24x24	69.0	0.58	-0.91	-0.07	2.77	10.56	2.56	11.21
25x25	69.5	0.58	-0.88	-0.07	2.78	10.36	2.03	10.92
26x26	71.1	0.60	-1.02	-0.06	2.69	10.18	2.06	10.73
27x27	71.7	0.57	-0.97	-0.06	2.72	10.26	2.13	10.82
28x28	72.0	0.56	-0.99	-0.06	2.74	10.31	2.26	10.91
30x30	72.5	0.55	-0.99	-0.10	2.74	10.24	2.15	10.81
40x40	76.9	0.52	-0.90	-0.07	2.71	10.14	2.29	10.75
50x50	86.0	0.52	-0.88	-0.05	2.71	10.12	2.41	10.75
70x70	117.8	0.52	-0.88	-0.05	2.70	10.11	2.38	10.74

Table 3.5 – Earth Gravity EGM-96 State Noise Correlation Times

autocor4.for	Direction		
	R	I	C
5x5	387.2046	25.1933	754.8398
10x10	211.0605	4.8500	420.5247
20x20	134.3853	0.3476	267.6209
21x21	131.0949	0.3915	261.1110
22x22	128.4610	0.3233	255.8411
23x23	126.1396	0.3875	251.0632
24x24	123.9387	0.3443	246.6534
25x25	121.9078	0.3012	242.5654
26x26	120.0385	0.3004	238.7804
27x27	118.2884	0.2866	235.2359
28x28	116.7078	0.3085	232.0099
29x29	115.2452	0.2680	229.0789
30x30	113.9493	0.2710	226.4442
40x40	106.6019	0.2344	211.5380
50x50	104.5926	0.2283	207.4407
70x70	104.1469	0.2267	206.5280

Table 3.6 – GEODE GPS/MET EGM-96 Comparison

GPS/MET 4 Feb 1997	Error Mean (m)			RMS Error (m)			
	R	I	C	R	I	C	3D
Gravity Model							
05x05	1.71	-5.58	-0.06	25.45	53.88	29.40	66.45
10x10	0.54	-2.01	0.62	7.70	18.21	7.16	21.03
20x20	0.52	-0.96	0.01	3.13	11.03	2.94	11.83
22x22	0.57	-0.87	-0.08	2.78	10.55	2.63	11.22
24x24	0.57	-0.87	-0.08	2.78	10.55	2.63	11.22
25x25	0.57	-0.82	-0.07	2.82	10.40	2.11	10.98
26x26	0.60	-0.98	-0.07	2.71	10.21	2.12	10.78
27x27	0.57	-0.95	-0.07	2.73	10.26	2.16	10.84
28x28	0.56	-0.95	-0.07	2.75	10.33	2.26	10.92
30x30	0.55	-0.97	-0.11	2.75	10.25	2.18	10.83
40x40	0.53	-0.90	-0.07	2.71	10.16	2.35	10.78
50x50	0.52	-0.88	-0.06	2.71	10.13	2.42	10.76
70x70	0.53	-0.88	-0.06	2.71	10.12	2.40	10.75

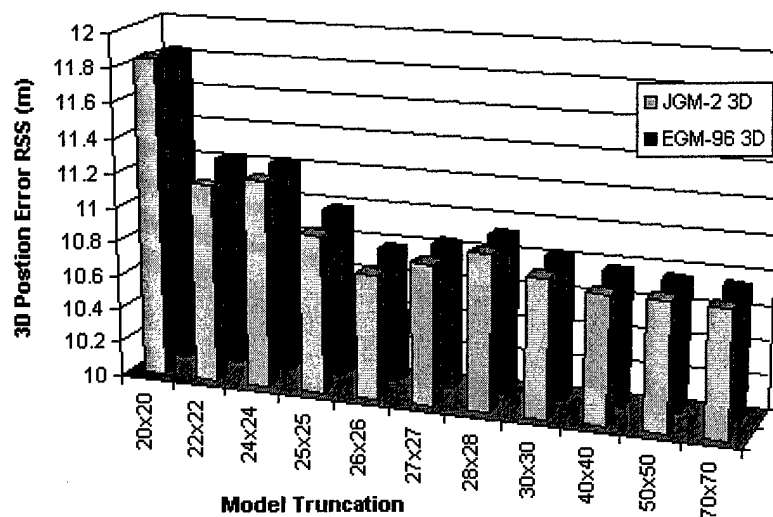


Figure 3.2 – JGM-2 / EGM-96 3D Position Error RSS Comparison

3.3 Gravitational Acceleration Approximation Function (GAAF)

Improving the speed of gravitational acceleration computations can significantly reduce the computational burden of an on board computer performing real-time satellite OD. Several methods currently used to improve the speed of computing gravitational accelerations are truncating the gravity model, pre-selecting a significant subset of coefficients, or tuning a truncated gravity field through estimation. Another method described in Hujsak [50] represents gravitational accelerations in terms of an instantaneous two-body acceleration for an instantaneous pseudocenter of the Earth. A set of pseudocenters at various heights and fixed latitude and longitude are fit to polynomials or polynomial quotients. The polynomial coefficients are calculated at various latitudes and longitudes. The stored coefficients are used to calculate the gravitational

acceleration. First, polynomials are evaluated using the satellite's height to recover a set of six pseudocenters surrounding the desired latitude and longitude of the satellite. Then, a six-point, bi-variate interpolation scheme is implemented to recover the pseudocenter at the given latitude and longitude. The pseudocenter is then used to recover the gravitational acceleration.

In the following development of GAAP, the method of pseudocenters is introduced and the benefits of ignoring the $C_{2,0}$ geopotential coefficient term in pseudocenter formulation are discussed. Next polynomial representation of pseudocenters as a function of height is shown, followed by interpolation of pseudocenters on a sphere of common height. Finally, storage requirements are shown.

3.3.1 Method of Pseudocenters

Given the Earth Centered, Earth Fixed (ECEF) gravitational acceleration on a spacecraft, \bar{a}_{ECEF} , and using the restricted two-body equation of motion, a pseudocenter, \bar{c}_{ECEF} , can be calculated. In equation (3.1) $\bar{\rho}_{ECEF}$ is a pseudoradius to the spacecraft.

$$\bar{a}_{ECEF} = -\mu \frac{\bar{\rho}_{ECEF}}{\bar{\rho}^3} \quad (3.1)$$

In the above equation \bar{a}_{ECEF} is the nonspherical acceleration calculated using spherical harmonic coefficient expansion of the nonspherical gravitational coefficients. Now the actual radius to the satellite is the pseudoradius plus a pseudocenter. A pseudocenter is a vector from the center of the Earth to where

the center of the Earth would need to be for the nonspherical acceleration acting on the satellite to equal the restricted two-body acceleration acting on the satellite.

$$\bar{\mathbf{r}}_{\text{ECEF}} = \bar{\rho}_{\text{ECEF}} + \bar{\mathbf{c}}_{\text{ECEF}} \quad (3.2)$$

or

$$\bar{\mathbf{c}}_{\text{ECEF}} = \bar{\mathbf{r}}_{\text{ECEF}} - \bar{\rho}_{\text{ECEF}} \quad (3.3)$$

By definition,

$$\rho = |\bar{\rho}_{\text{ECEF}}| \quad (3.4)$$

and

$$\bar{\rho}_{\text{ECEF}} = \rho \hat{\bar{\rho}}_{\text{ECEF}} \quad (3.5)$$

Also, since the pseudoradius vector is in the opposite direction of the acceleration:

$$\hat{\bar{\rho}}_{\text{ECEF}} = -\frac{\bar{\mathbf{a}}_{\text{ECEF}}}{|\bar{\mathbf{a}}_{\text{ECEF}}|} \quad (3.6)$$

Therefore, substituting equation (3.5) into equation (3.3) yields:

$$\bar{\mathbf{c}}_{\text{ECEF}} = \bar{\mathbf{r}}_{\text{ECEF}} - \rho \hat{\bar{\rho}}_{\text{ECEF}} \quad (3.7)$$

Now, dot product both sides of equation (3.1) with $\hat{\bar{\rho}}$ yielding:

$$|\bar{\mathbf{a}}_{\text{ECEF}}| = -\mu \frac{1}{\rho^2} \quad (3.8)$$

Therefore,

$$\rho = \sqrt{\frac{\mu}{|\bar{\mathbf{a}}_{\text{ECEF}}|}} \quad (3.9)$$

Leading to the result:

$$\bar{\mathbf{c}}_{\text{ECEF}} = \bar{\mathbf{r}}_{\text{ECEF}} - \sqrt{\frac{\mu}{|\bar{\mathbf{a}}_{\text{ECEF}}|}} \hat{\bar{\rho}}_{\text{ECEF}} \quad (3.10)$$

or

$$\bar{c}_{ECEF} = \bar{r}_{ECEF} + \sqrt{\mu} \frac{\bar{a}_{ECEF}}{|\bar{a}_{ECEF}|^{3/2}} \quad (3.11)$$

3.3.2 Benefits of Pseudocenter Formulation Without the C_{2,0} (J₂) Term

As noted in HujaK [50] the magnitude of the pseudocenters are less than 15 km ($|\bar{c}_{ECEF}| < 15 \text{ km}$) for all heights above 100 km. However, omitting the C_{2,0} term from the gravitational acceleration calculation yields $|\bar{c}_{ECEF}| < 250 \text{ meters}$ which can halve the storage requirements for the support data. The omitted C_{2,0} acceleration is then added in after the pseudocenter is used to recover the acceleration. Let

$$\bar{a}_{ECEF_0} = \bar{a}_{ECEF} - \bar{a}_{ECEF_{C_{2,0}}} \quad (3.12)$$

where

$$\bar{a}_{ECEF_{C_{2,0}}} = \begin{bmatrix} -C_{2,0} \frac{3}{2} \frac{\mu x}{r^3} \left(\frac{R_E}{r} \right)^2 \left(5 \left(\frac{z}{r} \right)^2 - 1 \right) \\ -C_{2,0} \frac{3}{2} \frac{\mu y}{r^3} \left(\frac{R_E}{r} \right)^2 \left(5 \left(\frac{z}{r} \right)^2 - 1 \right) \\ -C_{2,0} \frac{3}{2} \frac{\mu z}{r^3} \left(\frac{R_E}{r} \right)^2 \left(5 \left(\frac{z}{r} \right)^2 - 3 \right) \end{bmatrix} [51] \quad (3.13)$$

and $C_{2,0} = -J_2 = -1.082626925638815 \times 10^{-03}$ (from JGM-2)

Now the pseudocenter is calculated independent of C_{2,0}.

$$\bar{c}_{ECEF_0} = \bar{r}_{ECEF} + \sqrt{\mu} \frac{\bar{a}_{ECEF_0}}{|\bar{a}_{ECEF_0}|^{3/2}} \quad (3.14)$$

3.3.3 Polynomial Representation of Pseudocenter as a Function of Height

The first step in creating a set of coefficients by which gravitational acceleration can be recovered is to determine the altitude range of the spacecraft. Hujsak [50] uses an altitude range of 400 km to 1500 km. However, since the proposed real-time OD system will be used with spacecraft in circular or near circular orbits, smaller ranges are investigated here. Hujsak [50] suggests using quotients of polynomials of the form:

$$c_i = \frac{a_0 + a_1x + a_2x^2 + \dots + a_{n-1}x^{n-1}}{1 + b_1x + \dots + b_{d-1}x^{d-1}} \quad (3.15)$$

where

$$x = \frac{h - h_{\min}}{h_{\max} - h_{\min}} \quad (3.16)$$

Hujsak [50] reports $n + d \leq 8$ if the height in equation (3.16) is limited to

$$h_{\max} = 1500 \text{ km} \geq h \geq h_{\min} = 400 \text{ km}.$$

In this study, the GPS/MET spacecraft, altitude

$$h_{\max} = 752 \text{ km} \geq h \geq h_{\min} = 732 \text{ km},$$

is considered first. Up to seventh order polynomials of the form

$$c_i = a_0 + a_1x + a_2x^2 + \dots + a_7x^7 \quad (3.17)$$

are considered for the ease of implementation.

3.3.4 Pseudocenter Interpolation on a Sphere of Common Height

Hujsak [50] suggests a six-point, bi-variate interpolation scheme to take the pseudocenters calculated from the coefficients to the pseudocenter for a given latitude and longitude. Figure 3.3 shows the points used in the six-point, bi-variate interpolation scheme [52]. The circles represent the pseudocenters calculated at the fixed latitudes and longitudes while the square represents the latitude and longitude of the current satellite position.

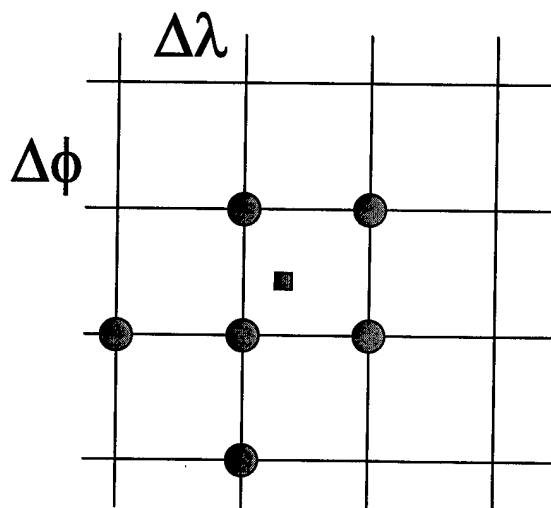


Figure 3.3 – Six-Point Bi-Variate Interpolation Scheme

The equation used for the six-point, bi-variate interpolation is:

$$\begin{aligned}
\bar{c}_0(\phi_p, \lambda_q, h) &= \bar{c}_0(\phi_0 + p\Delta\phi, \lambda_0 + q\Delta\lambda, h) \\
&= .5q(q-1)\bar{c}(\phi_0, \lambda_0 - \Delta\lambda, h) \\
&+ .5p(p-1)\bar{c}(\phi_0 - \Delta\phi, \lambda_0, h) \\
&+ (1 + pq - p^2 - q^2)\bar{c}(\phi_0, \lambda_0, h) \\
&+ .5p(p-2q+1)\bar{c}(\phi_0 + \Delta\phi, \lambda_0, h) \\
&+ .5q(q-2p+1)\bar{c}(\phi_0, \lambda_0 + \Delta\lambda, h) \\
&+ pq\bar{c}(\phi_0 + \Delta\phi, \lambda_0 + \Delta\lambda, h)
\end{aligned} \tag{3.18}$$

where

$$\begin{aligned}
p &= \frac{(\phi_p - \phi_0)}{\Delta\phi} \\
q &= \frac{(\lambda_q - \lambda_0)}{\Delta\lambda}
\end{aligned} \tag{3.19}$$

3.3.5 GAAF Storage Requirements

Hujsak [50] suggests larger increments of longitude as latitude increases to reduce storage requirements. In order to simplify indexing into the arrays holding the pseudocenter coefficients, there is an overlap between sets of pseudocenter coefficients, i.e., latitudes -59° and -60° are contained in sets 3b and 2b (see Table 3.7). The longitudes contained in 3b are $-2^\circ, 0^\circ, 2^\circ, \dots, 360^\circ$. Single precision (4 byte) floating point variables are used. The number of storage bytes needed for each latitude and longitude is calculated by:

$$\# \text{ coefficients/pseudocenter} * 3 \text{ pseudocenters} * 4 \text{ bytes}$$

At the GPS/MET altitude, 1,774,296 bytes are required (1.69 MB) compared to 5,024,832 bytes (4.79 MB) for the original implementation. The tradeoff is a smaller altitude and inclination range but the storage reduction is significant. Table 3.7 shows the longitude increments for different latitudes and the storage requirements for each range.

Table 3.7 – Original GPS/MET GAAF Storage Requirements For 3 Coefficients

	latitudes	$\Delta\lambda$	#lats	#lons	#bytes each	total bytes
3b	-75° to -59°	2.0°	17	182	36	111,384
2b	-61° to -47°	1.5°	15	242	36	130,680
1	-49° to 49°	1.0°	99	362	36	1,290,168
2a	47° to 61°	1.5°	15	242	36	130,680
3a	59° to 75°	2.0°	17	182	36	111,384
	Total					1,774,296

To decrease the complexity of implementing GAAF, coefficients are also generated using a single longitude increment of 1°. The number of bytes required to store the simplified implementation is $151 * 362 * 3 * 3 * 4$ or 1,967,832 bytes or (1.88 MB). The small increase in the number of bytes required is worth the improved simplicity of implementation. A detailed explanation of how GAAF is implemented and validated is shown next.

3.3.6 Integration With GAAF

The first task in implementing GAAF is to create a capability to generate highly accurate gravitational accelerations at multiple latitudes, longitudes and heights. Since GEODE already has a JGM-2 30x30 gravity model working, “subroutines” (classes) are taken from GEODE and augmented to include the full JGM-2 70x70 gravity model. The updated subroutines are then reintroduced into

GEODE. This is done to validate the new gravity model and to provide a method for evaluating GAAF. A GPS/MET orbit is integrated with GEODE and the results are compared to an integration performed with Analytical Graphics' Satellite Toolkit (STK). Additional information about STK can be found at <http://www.stk.com>. A direct comparison in the Earth Centered Inertial (ECI) coordinate system shows a 3D RSS error of 0.738 meters. There is no definitive explanation for the difference, except possibly differences in the way both programs handle polar motion, differences in nutation and precession constants and differences in the UTC to UT1 time conversion. Figure 3.4 shows the difference between the 70x70 GEODE trajectory and the 70x70 STK trajectory.

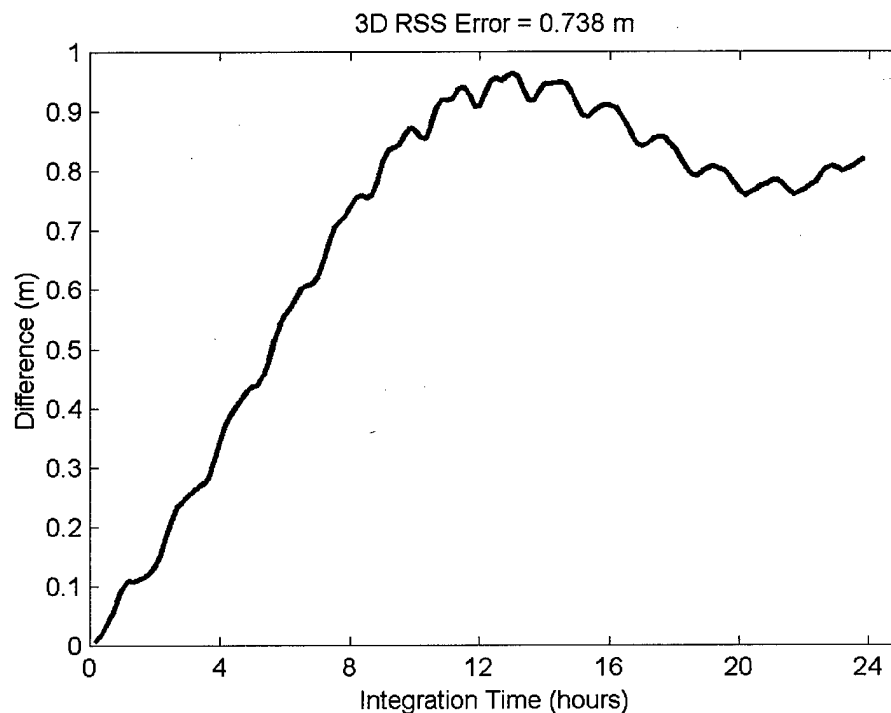


Figure 3.4 – GEODE / STK Integration Comparison

Another method used to ensure the new 70x70 gravity model is working properly is to compare the difference between a 70x70 and 30x30 propagation in GEODE and the difference between a 70x70 and 30x30 propagation in STK. The “differences” comparison shows that truncating the gravity model manifests itself the same way for both the STK and GEODE propagations. Figure 3.5 shows the excellent agreement between the STK/GEODE truncation comparisons.

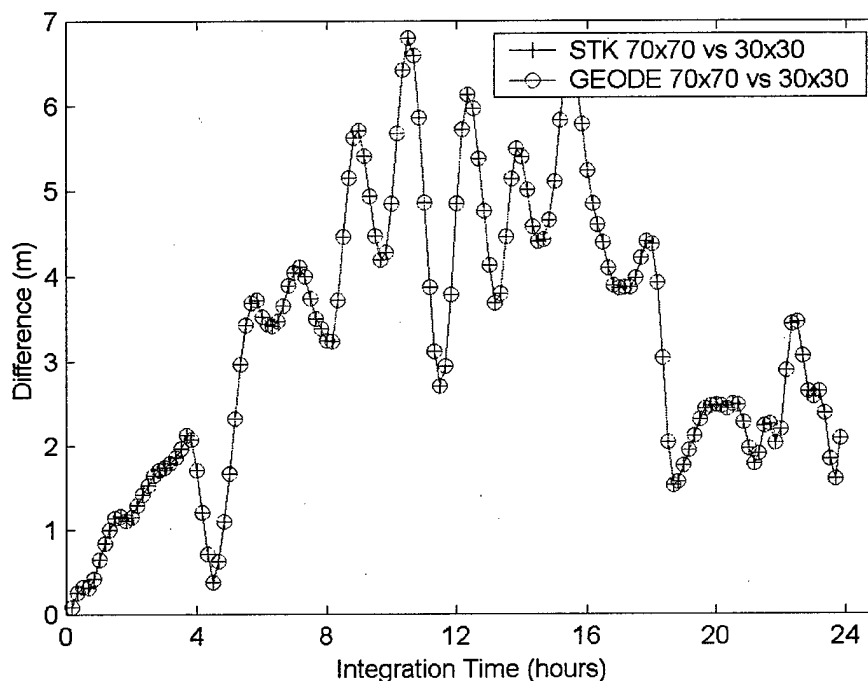


Figure 3.5 – GEODE / STK Difference Comparison

The conclusion from these results is the JGM-2 70x70 gravity model implemented in GEODE is working correctly. The JGM-3 and EGM-96 gravity models are implemented and validated in GEODE in the same way.

The next step is to implement GAAF with the GEODE integrator and compare the results to a 70x70 propagation. With the gravitational accelerations now available, a method is devised to determine the height range, height increment and number of polynomial coefficients to use for the GPS/MET orbit. Since the OrbView-1 satellite carrying GPS/MET is in a near circular orbit with a maximum altitude of just over 749 km and a minimum altitude of just over 734 km, an altitude range of 732 – 752 km is chosen. The decimated range is chosen to attempt to reduce the size of the memory needed to store the GAAF data. 2 to 8 polynomial coefficients are used to fit the pseudocenters. Hujsak [50] suggests using a quotient of polynomials as in equation (3.15) but this method could not be duplicated, so, polynomials are used as shown in equation (3.17).

Pseudocenters at fixed latitude and longitude are fit to polynomials using the following methodology:

Example:

let height increment for fit $\Delta h = 2$ km

$h_{\min} = 732$ km, $h_{\max} = 752$ km

$\phi = 30^\circ$

$\lambda = 30^\circ$

$n \equiv$ number of pseudocenters to fit = 11

$p \equiv$ number of polynomial coefficients = 2 through 8

therefore from equation (3.16)

$$\bar{x} = [0 \quad 0.1 \quad 0.2 \quad 0.3 \quad 0.4 \quad 0.5 \quad 0.6 \quad 0.7 \quad 0.8 \quad 0.9 \quad 1.0]^T \quad (3.20)$$

$$\bar{a} = [a_0 \quad a_1 \quad a_2 \quad \dots \quad a_{p-1}] \quad (3.21)$$

$$\bar{y}_i = [c_{i,1} \quad c_{i,2} \quad c_{i,3} \quad c_{i,4} \quad c_{i,5} \quad c_{i,6} \quad c_{i,7} \quad c_{i,8} \quad c_{i,9} \quad c_{i,10} \quad c_{i,11}]^T \quad (3.22)$$

$$X = \begin{bmatrix} 1 & x_1 & x_1^2 & \dots & x_1^{p-1} \\ 1 & x_2 & x_2^2 & \dots & x_2^{p-1} \\ 1 & x_3 & x_3^2 & \dots & x_3^{p-1} \\ \dots & \dots & \dots & \dots & \dots \\ 1 & x_{11} & x_{11}^2 & \dots & x_{11}^{p-1} \end{bmatrix} \quad (3.23)$$

$$\bar{\epsilon} = [\epsilon_1 \quad \epsilon_2 \quad \epsilon_3 \quad \dots \quad \epsilon_{11}]^T$$

Now the normal equation can be defined as:

$$\bar{y} = X\bar{a} + \bar{\epsilon} \quad (3.24)$$

where the solution to the normal equation for \bar{a} yields the coefficients of the polynomial that “fits” the vector of pseudocenters, \bar{y} . There are many ways to solve the normal equation. The method of least squares, as detailed in Montgomery [53], is

$$\bar{a} = (X^T X)^{-1} X^T \bar{y} \quad (3.25)$$

However, due to the computational burden of performing an inverse on a matrix as large as 50x50 (a much larger matrix is required for fitting a larger height range), a Givens orthogonal transformation is used to solve for \bar{a} [39]. Here an orthogonal transformation is performed to upper triangularize the matrix

$$[X \quad \bar{y}] \quad (3.26)$$

resulting in a matrix of the form

$$\begin{bmatrix} h_{11} & \dots & h_{1n} & b_1 \\ 0 & \dots & \dots & \dots \\ 0 & 0 & h_{nn} & b_n \\ 0 & 0 & 0 & \sum_{i=1}^n \epsilon_i^2 \end{bmatrix} \quad (3.27)$$

Then, back substitution is performed to solve for \bar{a} , where $a_n = b_n/h_{nn}$ and so on.

Orthogonal transformations require less computational burden to solve the normal equation [39]. Table 3.8 shows the pseudocenter elements at $\phi = 30^\circ$ and $\lambda = 30^\circ$ for the height range of 732-752 km at 2 km increments. Figure 3.6 shows the linear nature of the pseudocenters.

Table 3.8 – Test Pseudocenters

height	x	y1	y2	y3
732	0	26.1723	-40.4541	32.0436
734	0.1	26.2094	-40.5061	32.0783
736	0.2	26.2465	-40.5578	32.1126
738	0.3	26.2835	-40.6093	32.1466
740	0.4	26.3204	-40.6605	32.1803
742	0.5	26.3572	-40.7115	32.2135
744	0.6	26.3940	-40.7623	32.2465
746	0.7	26.4307	-40.8128	32.2790
748	0.8	26.4674	-40.8631	32.3113
750	0.9	26.5040	-40.9131	32.3432
752	1	26.5405	-40.9629	32.3747

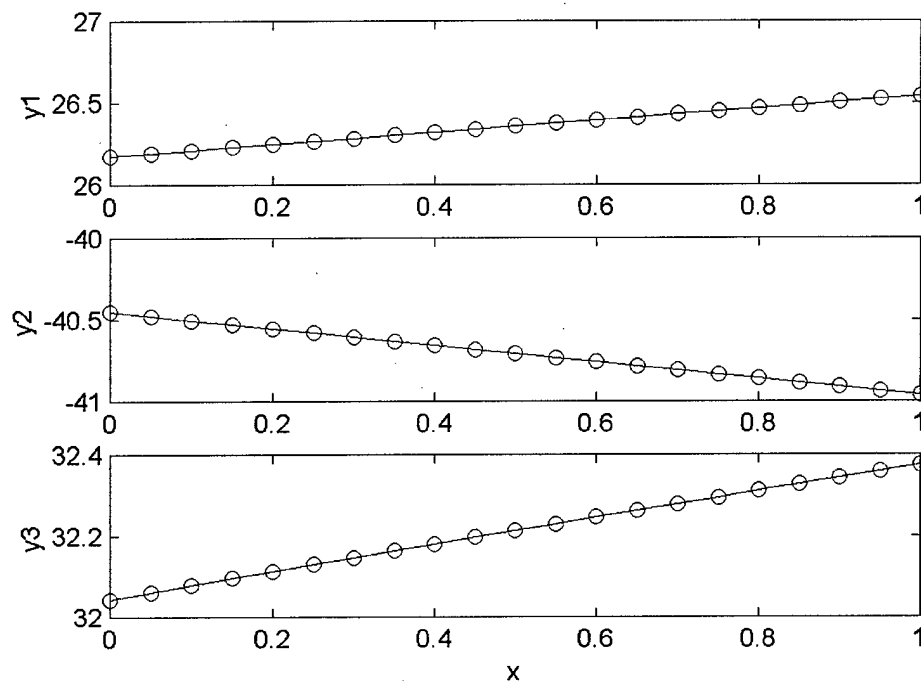


Figure 3.6 – Linear Nature of Pseudocenters

Next, the most appropriate number of polynomial coefficients to fit the pseudocenters is determined. The Residual Mean Square (RMS) (σ^2) [53] is calculated for set of polynomials where

$$\sigma^2 = \frac{\bar{y}^T \bar{y} - \bar{a}^T X^T \bar{y}}{n - p} \quad (3.28)$$

Table 3.9 shows the polynomial coefficients calculated and their corresponding residual mean square error. At 30° latitude, 30° longitude and with a 2 km height increment, the best fit is $p = 3$. To determine the best height increment and number of polynomial coefficients for the GPS/MET orbit, a range of height increments from 0.25 to 4 km are used along with a range of polynomial

coefficients from 2 to 8 (first order to seventh order). The RMS error is calculated at multiple (100's) latitudes and longitudes. The best fit is determined by the average of the RMS errors. The GPS/MET orbit produced a best fit with the height increment at 3.0 km and $p = 3$. An example set of coefficients and RMS values for various order polynomials are shown below in Figure 3.7.

Table 3.9 – Example GPS/MET GAAF Coefficients and RMS for y1

	a0	a1	a2	a3	a4	a5	a6	a7	σ^2
p = 2	26.173	0.3681							1.05e-07
p = 3	26.172	0.3714	-0.00332						2.80e-11
p = 4	26.172	0.3714	-0.003046	-0.000182					2.10e-11
p = 5	26.172	0.3714	-0.003036	-0.00020	8.36e-6				9.35e-10
p = 6	26.172	0.3714	-0.003037	-0.000197	5.93e-6	9.71e-7			1.45e-08
p = 7	26.172	0.3714	-0.003038	-0.000193	-2.41e-6	8.44e-6	-2.50e-6		5.06e-07
p = 8	26.172	0.3714	-0.003040	-0.000177	-4.53e-5	7.44e-5	-4.95e-5	1.25e-5	7.08e-05

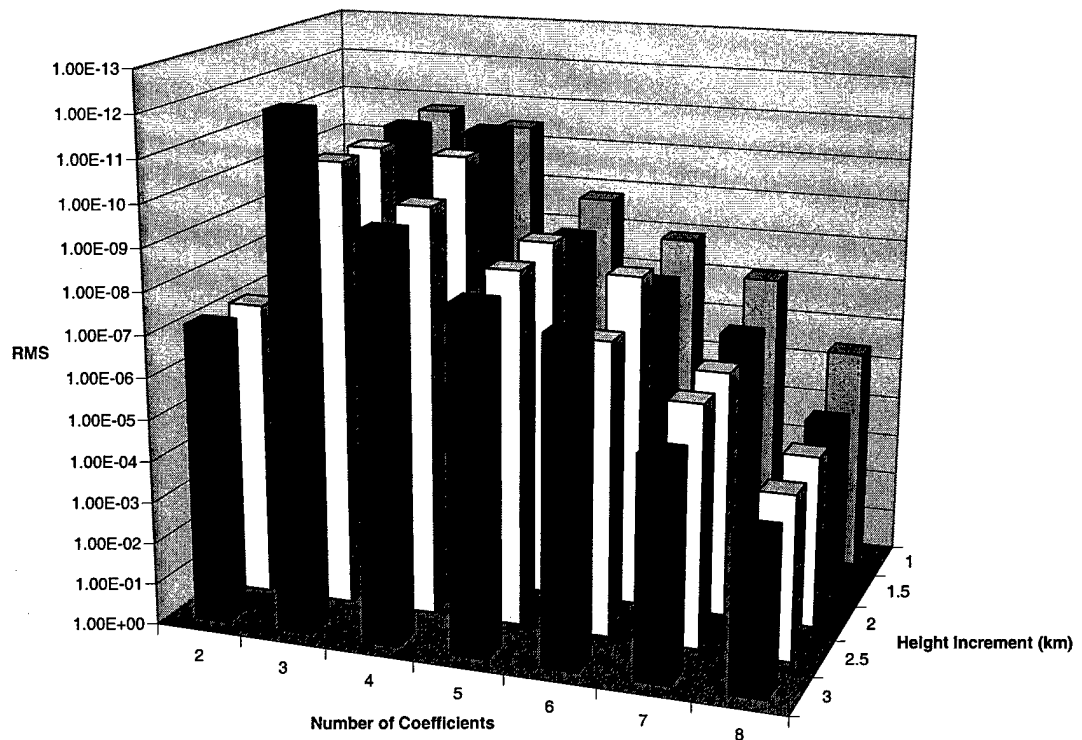


Figure 3.7 – GPS/MET Polynomial Fit RMS Error

The pseudocenter coefficients are then calculated and stored in a file formatted as an array in the C programming language. The array variable is then initialized as a static variable in C and the coefficients are accessed according to latitude and longitude. Six sets of coefficients are accessed each time an acceleration is calculated. Below find the equations used to recover acceleration from the pseudocenter coefficients with $p = 3$. The six pseudocenters at the given height are calculated to interpolate between the fixed latitudes and longitudes. Equation (3.18) is used for the bi-variate interpolation. First, the pseudocenters are calculated from the tables of polynomial coefficients.

$$c_{ECEF_0_i} = a_0 + a_1 x + a_2 x^2 \quad i = 1, 2, 3 \quad (3.29)$$

where a_0 , a_1 and a_2 are the polynomial coefficients.

$$x = \frac{h - h_{\min}}{h_{\max} - h_{\min}} \quad (3.30)$$

$$h_{\min} = 732 \text{ km}$$

$$h_{\max} = 752 \text{ km}$$

Next, six sets of pseudocenters are used to interpolate using equation (3.18).

Then the pseudoradius is calculated by

$$\bar{\rho}_{ECEF} = \bar{r}_{ECEF} - \bar{c}_{ECEF_0} \quad (3.31)$$

and the acceleration (without the $C_{2,0}$ term is calculated)

$$\bar{a}_{ECEF_0} = \frac{-\mu \bar{\rho}_{ECEF}}{\rho^3} \quad (3.32)$$

$$\bar{a}_{ECEF} = \bar{a}_{ECEF_0} + \bar{a}_{ECEF_{C_{2,0}}} \quad (3.33)$$

where $\bar{a}_{ECEF_{C_{2,0}}}$ is found by equation (3.13). The acceleration in the ECEF

coordinate system is then rotated to the J2000 system by the transpose of the transformation matrix [J2000toECEF]. Here

$$[J2000toECEF] = [TODtoECEF][MODtoTOD][J2000toMOD] \quad (3.34)$$

where the definition of the transformation matrices above can be found in Lee [37].

With the code written to recover gravitational accelerations from the array of polynomial coefficients a 24-hour GPS/MET propagation is performed with the GEODE integrator. However, here GAAF is used instead of spherical harmonic coefficient expansion. First order polynomials are used to fit the pseudocenters to

minimize storage requirements. The results are compared to a propagation performed using the 30x30 and 70x70 JGM-2 models. Table 3.10 shows the orbit errors and 3D RSS error of the difference between the 30x30 and the 70x70 and GAAF and the 70x70. The run times for the various integrations are also included in the table. The GAAF run time is 19.3% shorter than the 30x30 model and more accurate. GAAF works wonderfully, increasing accuracy while decreasing computational burden. Figure 3.8 shows a plot of the propagation errors.

Table 3.10 – GPS/MET GAAF and 30x30 Integration Compared to 70x70

GPS/MET - 4 Feb 1997		Integration RMS Error (m)			
Gravity Model	Run Time (sec)	R	I	C	3D
70x70	121.5				
30x30 vs 70x70	74.4	2.41	1.03	2.57	3.67
GAAF* vs 70x70	60.1	0.14	0.06	0.13	0.02

*GAAF created using 70x70 JGM-2 Gravity Model

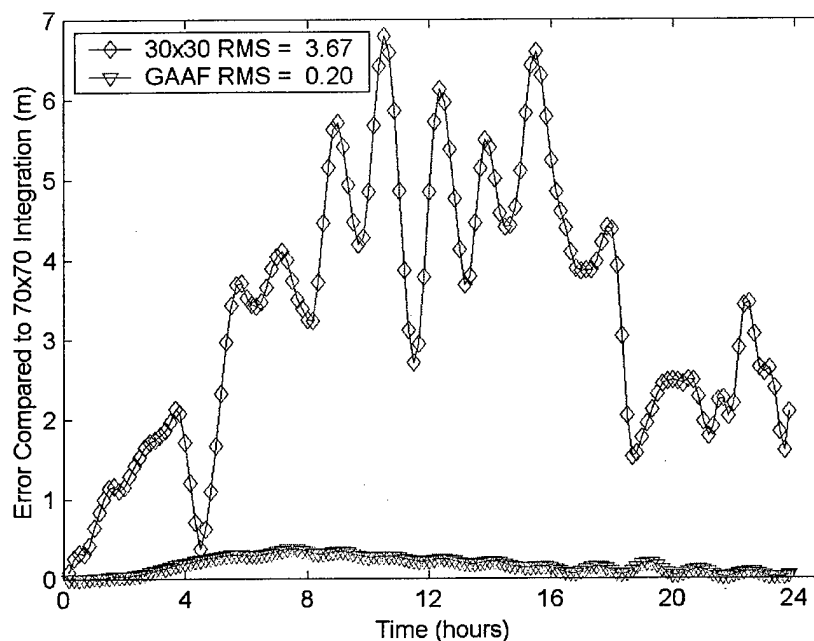


Figure 3.8 - GPS/MET GAAF and 30x30 Integration Compared to 70x70

3.4 GAAF in GEODE

The final step in assessing the accuracy and computational burden of GAAF is to use it in GEODE for satellite OD. Table 3.11 shows the GEODE OD results using GAAF. The results in Table 3.11 confirm the claim in Hujsak [50] that the computational burden of GAAF is equivalent to the computational burden of a 5x5 gravity model with the accuracy of a 70x70. GAAF maintains accuracy in GEODE and significantly reduces the computational burden with first order polynomials (2 coefficients per pseudocenter direction). This first order GPS/MET implementation of GAAF requires only 1.28 MB of storage space.

Table 3.11 – GEODE GPS/MET Gravity Model Results Comparison

GPS/MET 4 Feb 1997		Mean Error (m)			RMS Error (m)			
Gravity Model	*Run Time (sec)	R	I	C	R	I	C	3D
JGM-2 05x05	39.5	1.71	-5.57	-0.06	25.42	53.87	29.42	66.43
JGM-2 30x30	45.6	0.55	-0.99	-0.10	2.74	10.24	2.15	10.81
JGM-2 70x70	83.2	0.52	-0.88	-0.05	2.70	10.11	2.38	10.74
GAFF	39.2	0.52	-0.88	-0.05	2.71	10.11	2.38	10.74
EGM-96 30x30	45.6	0.55	-0.97	-0.11	2.75	10.25	2.18	10.83
JGM-3 30x30	45.6	0.52	-0.91	-0.11	2.74	10.24	1.98	10.78

* Run on 450MHZ Pentium II, 128 MB RAM

3.5 JGM-3 and EGM-96 Gravity Models

The JGM-3 and EGM-96 gravity models are also implemented in GEODE. Table 3.11 shows no improvement in OD accuracy or precision in GEODE when different models are used instead of the JGM-2 model.

3.6 Summary

Although there is a moderate increase in the propagation accuracy between a JGM-2 20x20 gravity model and a JGM-2 30x30 gravity model, the OD accuracy and the computational burden difference between the two JGM-2 models is minimal. The best choice in balancing accuracy/precision and computational burden in a real-time OD system appears to be a 30x30 gravity model. Also, the type of model (JGM-2, JGM-3 or EGM-96) does not appear to affect OD accuracy with GEODE.

A different approach significantly reducing computational burden while maintaining accuracy is Hujsak's Gravity Acceleration Approximation Function (GAAF) [50]. GAAF maintains the accuracy of a 70x70 gravity model with the computational burden of a 5x5 model. GAAF improves GEODE's computational burden by 14% compared to GEODE with a 30x30 gravity model. The cost of using GAAF is a 1 to 5 MB RAM requirement, depending on the application. GAAF should definitely be considered as a viable alternative to conventional methods of calculating the gravitational acceleration in real-time OD systems where computational burden needs to be minimized.

CHAPTER 4

Ionosphere

Ionospheric errors can significantly degrade the accuracy of the GPS pseudorange measurement. These errors can range from a few meters to many tens of meters and with SA off, ionospheric errors can be the largest measurement error source [10]. Dual frequency GPS users can determine ionospheric errors, to first order, using a combination of the P1 and P2 measurements as shown in equation (2.11). Single frequency users must either rely on ionospheric models or a linear combination of the pseudorange and phase measurements. In a real-time OD system on board a satellite, the overhead of using a model may be unrealistic. Therefore, the Differenced Range Versus Integrated Doppler (DRVID) [29] method is presented and investigated here. The results of a DRVID implementation in GEODE are also presented.

4.1 Differenced Range Versus Integrated Doppler (DRVID)

The ionosphere is the region of the upper atmosphere between 50 and 1000 km altitude. It contains electrons and ions formed by the ionizing radiation of the Sun. These electrons and ions are in sufficient quantities to significantly affect radio wave propagation where the delay experienced by these signals is proportional to the number of electrons in the signal's path. Unfortunately, the

affects on radio wave propagation are highly variable and change by at least one order of magnitude through the course of each day. The effects can be:

- three times greater on a signal transmitted near the horizon compared to one transmitted from the zenith direction
- five times greater during the day than at night
- four times greater in November than July
- three times greater during solar maximum than solar minimum [54]

Because of this high variability, the ionosphere is very difficult to model.

There are four regions of the ionosphere formed by different chemical interactions with the ultraviolet (UV) radiation from the Sun. Only one of these is of primary concern for satellite OD using GPS. It is the F2 region from 210 – 1000 km and is the densest and has the highest variability [43]. The peak density in the F2 region varies between 250 and 400 km. The F2 region can, potentially, cause the most significant effects on GPS receiving systems [43]. Another area associated with the ionosphere is the protonosphere. Its region designation is H+ and it occupies the area above 1000 km and extends to the GPS orbits. It is composed of ionized hydrogen and some helium gas, is of very low density and its estimated contribution to signal time delay is 10% during the day and approximately 50% at night [43]. The protonosphere does not change significantly between day and night but is depleted during major magnetic storms and can take several days to recover [43].

The ionosphere can be a significant error source in using GPS measurements. These errors can range from a few meters to many tens of meters at the GPS frequencies. There are effectively eight ways the ionosphere effects

GPS measurements [43], but only two are significant enough to be discussed here: group delay of the signal modulation (absolute range error) and carrier phase advance (relative range error).

Most receivers (unless codeless or Precise Positioning System (PPS) capable) can only collect data on the L1 frequency and thus the group range delay and phase advance of the GPS observations cannot be calculated. Modeling the ionosphere is marginally accurate and scaling the coefficients to satellite altitudes may cause further inaccuracies [55]. Transmitting measurements or delay corrections to a satellite introduces additional complexity and overhead. Unfortunately, the systematic errors introduced by not modeling the ionospheric range delay and phase advance can hinder the estimation of unmodeled or mismodeled forces using techniques like Dynamic Model Compensation (DMC) or the Reduced Dynamic Technique (RDT) [9]. In Gold [56] it is shown that RDT performs worse than a purely dynamic run if ionospheric errors are not removed. Fortunately, the DRVID measurement can potentially remove the systematic ionospheric delay errors that can reduce the accuracy of OD systems estimating empirical accelerations.

The group delay is proportional to the Total Electron Content (TEC) and inversely proportional to the frequency squared of the modulated signal. The TEC is the number of electrons in a vertical column having a 1 m^2 cross-section and extending from the receiver to the GPS satellite. The following equation is used to calculate the group delay in units of time [10]:

$$\Delta t_{p_{ion}} = \frac{40.3}{cf^2} \text{TEC} \quad (4.1)$$

where

$c \equiv$ the speed of light in a vacuum = 299,792,458 m/s
 $f \equiv$ signal frequency i.e. $f_{L_1} = 1575.42$ MHz and $f_{L_2} = 1227.6$ MHz

or expressed in units of range

$$\Delta p_{ion} = \frac{40.3}{f^2} \text{TEC} \quad (4.2)$$

While the range measurement is delayed, the ionosphere advances phase. Phase advance, in units of time, is calculated by

$$\Delta t_{\phi_{ion}} = -\frac{40.3}{cf^2} \text{TEC} \quad (4.3)$$

or expressed as phase range

$$\Delta p_{\phi_{ion}} = -\frac{40.3}{f^2} \text{TEC} \quad (4.4)$$

Techniques for dealing with ionospheric errors include modeling, using direct measurements, using a dual frequency receiver or combining range and phase measurements on a single frequency receiver.

There are many models available to estimate TEC to attempt to calculate the range delay and/or phase advance of GPS measurements. The simplest and most readily available is the Klobuchar model consisting of eight parameters contained in the broadcast navigation message. Surprisingly, the simple Klobuchar model consistently exceeds its design goal of 50% accuracy.

Unfortunately, very complex models using hundreds of coefficients can only marginally improve accuracy and cannot consistently surpass 75% accuracy [30].

Another method of generating ionospheric delay corrections is JPL's Global Ionosphere Map (GIM). Dual frequency GPS measurements are taken from a network of GPS receivers. These measurements are processed and maps of the electron content of the ionosphere are produced. GIM will be integrated into the FAA's operational WAAS software [16]. GIM operations can take place in real-time, on board a satellite; however, there is significant overhead in providing the maps to the satellite for processing. It is unknown what the computational burden of the GIM software is but it requires a 383 KB file each day [57]. WAAS or WADGPS will broadcast ionospheric corrections but, again, neither system is currently operational.

The DRVID technique can be attributed to MacDoran [29] although previous work had been done as early as 1966 [31]. Due to similarities between the original signal structures and those used in GPS, DRVID is generalized for use with single frequency GPS measurements [58]. The DRVID technique is further investigated in Schreiner [31] and Gold [59]. JPL's implementation of DRVID in satellite OD using GPS is called GRAPHIC (Group and Phase Ionosphere Calibration) [30, 32, 60].

It is important to note that since the pseudorange measurement is 20-100 times less precise than the phase measurement, the error in the combined DRVID measurement is half that of the pseudorange measurement. The new

measurement gets the worst of both data types since it gets the reduced information content of the phase delay (due to the phase integer ambiguity) and the approximate noise level of the pseudorange measurement [60].

4.2 DRVID Development

The geometric range from the user satellite to each GPS satellite is given by:

$$\rho_i = \sqrt{(x_u - x_{GPS_i})^2 + (y_u - y_{GPS_i})^2 + (z_u - z_{GPS_i})^2} \quad (4.5)$$

The measured code based pseudorange in meters is:

$$\rho_{P_{L_i}} = \rho_i + b_u c - b_{GPS_i} c + \Delta\rho_{ion} \quad (4.6)$$

where:

- $c \equiv$ the speed of light
- $b_u \equiv$ user clock bias
- $b_{GPS} \equiv$ GPS spacecraft clock bias
- $\Delta\rho_{ion} \equiv$ change in range due to ionospheric affects

The measured beat phase based pseudorange in cycles is [31, 54]:

$$\phi_{L_{L_i}} + N_i = -\frac{f}{c}\rho_i - b_u f + b_{GPS_i} f + \frac{f}{c}\Delta\rho_{ion} \quad (4.7)$$

where:

- $N_i \equiv$ unknown integer ambiguity.
- $f \equiv$ measurement frequency

The measured beat phase based pseudorange in meters is:

$$-(\phi_{L_{L_i}} + N_i) \frac{c}{f} = \rho_i + b_u c - b_{GPS_i} c - \Delta\rho_{ion}$$

$$\rho_{L_i} = -\left(\phi_{L_i} + N_i\right) \frac{c}{f} = \rho_i + b_u c - b_{GPS_i} c - \Delta\rho_{ion} \quad (4.8)$$

$$\phi_{L_i} \frac{c}{f} = N_i \frac{c}{f} - \rho_i - b_u c + b_{GPS_i} c + \Delta\rho_{ion} \quad (4.9)$$

Now a linear combination of equations (4.6) and (4.7) is made to remove the change in range due to the ionosphere.

$$\frac{\rho_{P_i} + \rho_{L_i}}{2} = \frac{\rho_{P_i} - \left(\phi_{L_i} + N_i\right) \frac{c}{f}}{2} \quad (4.10)$$

$$\frac{\rho_{P_i} - \left(\phi_{L_i} + N_i\right) \frac{c}{f}}{2} = \frac{\rho_i + b_u c - b_{GPS_i} c + \Delta\rho_{ion} + \rho_i + b_u c - b_{GPS_i} c - \Delta\rho_{ion}}{2} \quad (4.11)$$

$$\rho_{ion free_i} = \frac{\rho_{P_i} - \phi_{L_i} \frac{c}{f}}{2} = \rho_i + b_u c - b_{GPS_i} c + N_i \frac{c}{2f} \quad (4.12)$$

Now the ionospheric free DRVID measurement is given by

$$Y_{observed} = \frac{\rho_{P_i} - \phi_{L_i} \frac{c}{f}}{2} \quad (4.13)$$

The ionospheric free computed measurement is given by:

$$Y_{computed} = \rho_i + b_u c - b_{GPS_i} c + N_i \frac{c}{2f} \quad (4.14)$$

The difficulty now becomes solving for the integer ambiguity N_i . N_i can be estimated as part of the state, however, care needs to be taken to account for cycle slips on the phase measurement.

4.2.1 Estimation of the Integer Ambiguity N_i

If the integer ambiguity is to be estimated, the new GEODE state would become:

$$X = \begin{bmatrix} x & y & z & \dot{x} & \dot{y} & \dot{z} & C_D & C_R & b & \dot{b} & N_1 & \dots & N_i & \dots & N_n \end{bmatrix}_{(10+n) \times 1}^T \quad (4.15)$$

where n is the number of GPS satellites providing pseudorange and phase measurements to the user spacecraft at a given epoch. The observation state relationship is defined by:

$$Y_i^k = G_i [X(t_k), t_k] + \epsilon_i \quad (4.16)$$

Since the observation state relationship is non-linear we take the partial derivative of the computed observation equation with respect to the state, i.e.,
(with $b = b_u c$)

$$G_i [X(t_k), t_k] = \rho_{ionfree_i} = \rho + b - b_{GPS_i} c + N_i \frac{c}{2f} \quad (4.17)$$

where

$$\rho = \sqrt{(x_u - x_{GPS_i})^2 + (y_u - y_{GPS_i})^2 + (z_u - z_{GPS_i})^2} \quad (4.18)$$

$$H_i^k = \frac{\partial G_i [X(t_k), t_k]}{\partial X(t_k)} \quad (4.19)$$

$$\begin{aligned}
 H_i = & \begin{bmatrix} \frac{\left(x_u - x_{\text{GPS}_i} \right)}{\rho_{\text{ion free}_i}} \\ \frac{\left(y_u - y_{\text{GPS}_i} \right)}{\rho_{\text{ion free}_i}} \\ \frac{\left(z_u - z_{\text{GPS}_i} \right)}{\rho_{\text{ion free}_i}} \\ 0 \\ 0 \\ 0 \\ 0 \\ 0 \\ 1 \\ 0 \\ 0 \\ \vdots \\ \frac{c}{2f} \\ \vdots \\ 0 \end{bmatrix}^T \\
 & \quad \quad \quad 1 \times (10 + n)
 \end{aligned} \tag{4.20}$$

The difficulties involved in this implementation are: dynamically adjusting the size of the state to reflect the number of GPS spacecraft being tracked and keeping track of cycle slips to reinitialize the appropriate member of the state when a cycle slip occurs. Another problem with this implementation is

the added computational burden and complexity of adding up to 12 constants to the state, depending on the number of channels of the GPS receiver.

4.2.2 Calculation of $\Delta\rho_{\text{ion}}$ Using $\Delta\rho_{\text{PI}}$ and $\Delta\rho_{\text{LI}}$

Another method of calculating the change in range due to ionospheric effects is to use beat phase and pseudorange at different epochs. In this manner the change in the ionospheric effects can be calculated from one epoch to the next. Differencing equation (4.9) at two epochs yields [31]:

$$\Delta\rho_{\text{LI}}^k = (\phi_{\text{LI}}^k - \phi_{\text{LI}}^0) \quad (4.21)$$

where 0 is the initial tracking epoch and k is the epoch of interest.

Or

$$\Delta\rho_{\text{LI}}^k = -(N_i^k - N_i^0) - (\rho_i^k - \rho_i^0) - (b_u^k c - b_u^0 c) + (b_{\text{GPS}_i}^k c - b_{\text{GPS}_i}^0 c) + (\Delta\rho_{\text{ion}_i}^k - \Delta\rho_{\text{ion}_i}^0)$$

Differencing equation (4.6) at the two epochs yields:

$$\Delta\rho_{\text{PI}}^k = (\rho_i^k - \rho_i^0) + (b_u^k c - b_u^0 c) - (b_{\text{GPS}_i}^k c - b_{\text{GPS}_i}^0 c) + (\Delta\rho_{\text{ion}_i}^k - \Delta\rho_{\text{ion}_i}^0) \quad (4.22)$$

Assuming the integer ambiguity is constant between epochs and adding these two “delta range” measurements together yields:

$$\Delta\rho_{\text{PI}}^k - \Delta\rho_{\text{LI}}^k = 2(\Delta\rho_{\text{ion}_i}^k - \Delta\rho_{\text{ion}_i}^0) \quad (4.23)$$

There are several ways to account for $\Delta\rho_{\text{ion}_i}^0$. One is to model the ionosphere so whenever the user receiver starts tracking a new GPS spacecraft the ionospheric “bias” ($\Delta\rho_{\text{ion}_i}^0$) is calculated. Then with $\Delta\rho_{\text{ion}_i}^0$ known:

$$\Delta\rho_{ion_i}^k = \frac{\Delta\rho_{P_i}^k - \Delta\rho_{L_i}^k}{2} + \Delta\rho_{ion_i}^0 \quad (4.24)$$

or

$$\Delta\rho_{ion_i}^k = \frac{(\rho_{P_i}^k - \rho_{P_i}^0) - (\phi_{L_i}^k - \phi_{L_i}^0) \frac{c}{f}}{2} + \Delta\rho_{ion_i}^0 \quad (4.25)$$

4.2.2.1 Model Bias DRVID

In Kubitschek [61] estimation of the $\Delta\rho_{ion_i}^0$ bias through ionospheric modeling using GIM maps applied in conjunction with DRVID provided excellent ionospheric error estimation compared to the use of dual frequency measurements. Results from [61] for 2 Feb 1997 GPS/MET data are presented in the first column of Table 4.1. Estimation of the $\Delta\rho_{ion_i}^0$ bias using the GIM maps requires a 383 KB data file that is updated daily. Uplinking a 383 KB file to a spacecraft every day is probably unreasonable overhead. Another approach that proved just as accurate as modeling the $\Delta\rho_{ion_i}^0$ bias in [61] is not estimating the bias but allowing the OD filter to estimate it along with the GPS satellite clock bias. Allowing the filter to estimate the $\Delta\rho_{ion_i}^0$ bias works because the bias is constant for each GPS satellite during a continuous tracking arc. Unfortunately, real-time filters do not estimate the GPS satellite clock biases so a different approach is needed.

Table 4.1 – Error Between DRVID Methods and Dual Frequency

3 Feb 1997	RMS Error between dual frequency and	
PRN#	bias estimation from modeling (m)	bias = 0 (m)
PRN 1	1.668	1.876
PRN 2	1.888	2.614
PRN 3	3.213	3.297
PRN 4	1.635	2.389
PRN 5	2.187	2.651
PRN 6	1.121	1.903
PRN 7	1.861	2.035
PRN 9	1.22	1.916
PRN10	1.985	2.619
PRN14	2.305	4.047
PRN15	1.917	2.463
PRN16	2.576	5.420
PRN17	2.059	2.264
PRN18	2.515	3.937
PRN19	1.672	2.154
PRN21	1.927	2.450
PRN22	5.74	7.290
PRN23	1.752	1.820
PRN24	2.138	2.100
PRN25	3.171	3.369
PRN26	0.996	1.604
PRN27	1.235	5.769
PRN29	1.009	1.765
PRN30	0.944	1.391
PRN31	1.333	1.725
Mean	2.002	2.835

4.2.2.2 Zero Bias DRVID

Another less computationally burdensome method presented itself when plotting the measurement elevation angles of GPS/MET with respect to GPS satellites. Since GPS/MET is an occultation experiment its GPS antenna is

pointing in the anti-velocity direction providing reception of “setting” occultations. See Figure 2.2.

Examination of the elevation of the GPS/MET GPS observations indicates GPS spacecraft are nominally acquired at or near their highest elevation. Figure 4.1 through Figure 4.5 show the elevation of the measurements from GPS satellites PRN01, PRN16, PRN14, PRN29 and PRN10 taken by GPS/MET on 4 Feb 1997. The lighter points on the plots distinguish periods when the OrbView-1 satellite is in sunlight (Day in the legend of the plots). The darker points are when the satellite is in the darkness (Night).

The elevations for PRNs 1 and 29 show they are nominally acquired at or near their highest elevation. The elevations for PRNs 16, 10 and 14 show an elevation increase and decrease every third time they are acquired. Seven out of the twenty-seven GPS satellites tracked by GPS/MET on 4 Feb 1997 exhibit the elevation decrease, increase, decrease phenomenon at approximately -15° elevation. This phenomenon is most likely due to occultation of the GPS signal.

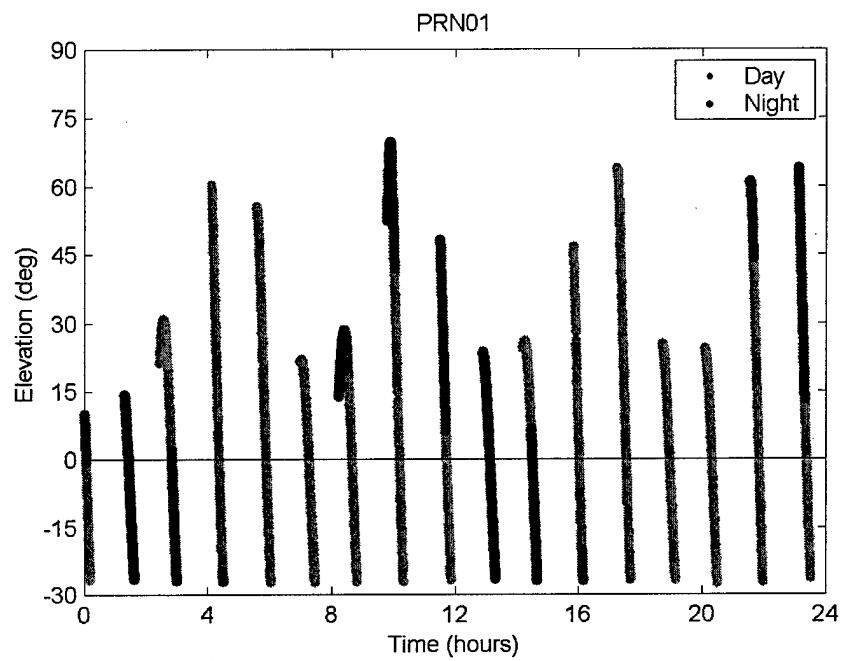


Figure 4.1 – PRN01 GPS/MET Elevation Plot

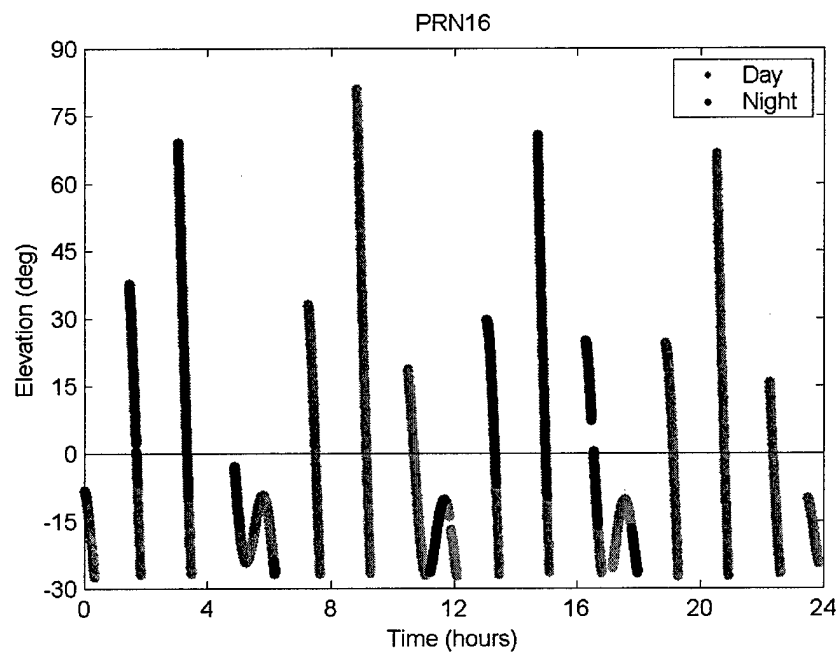


Figure 4.2 – PRN16 GPS/MET Elevation Plot

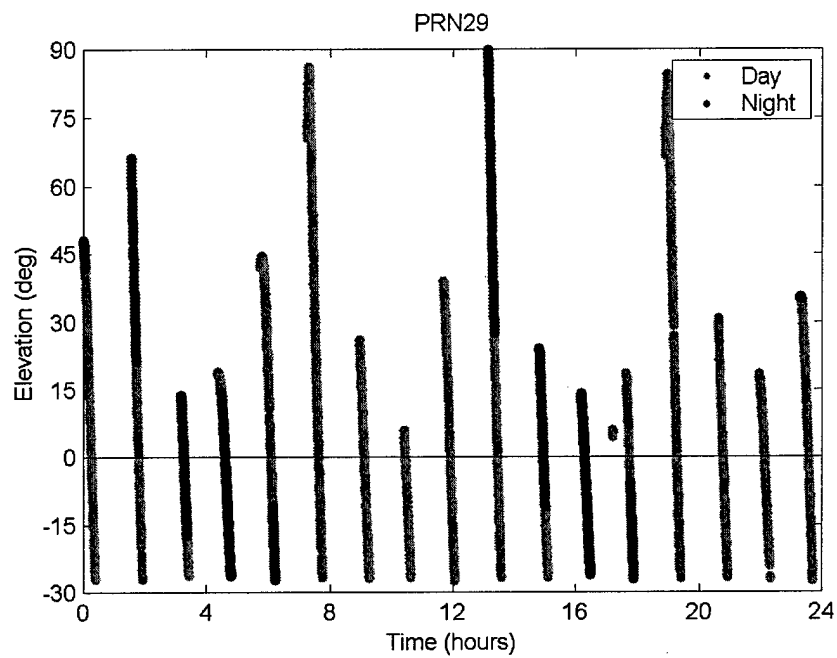


Figure 4.3 – PRN29 GPS/MET Elevation Plot

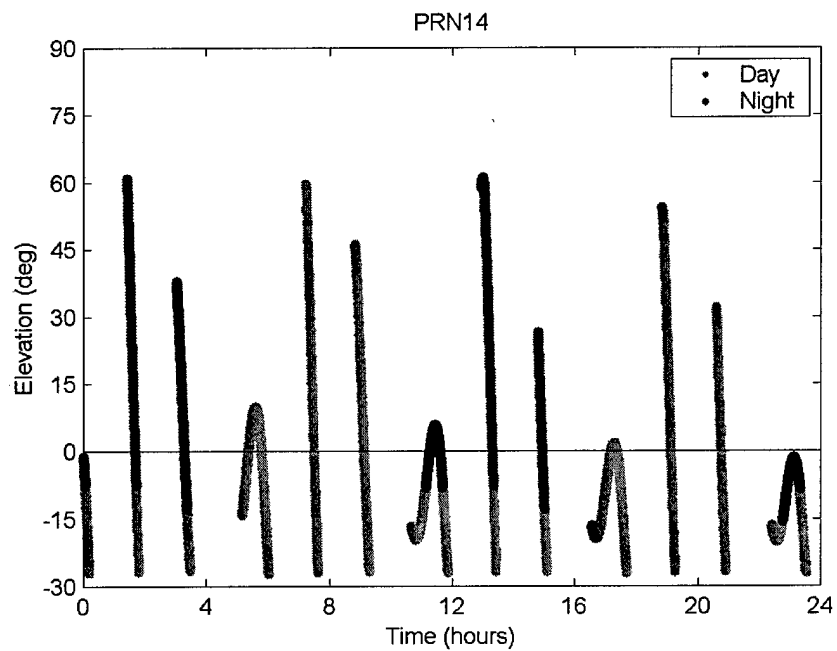


Figure 4.4 – PRN14 GPS/MET Elevation Plot

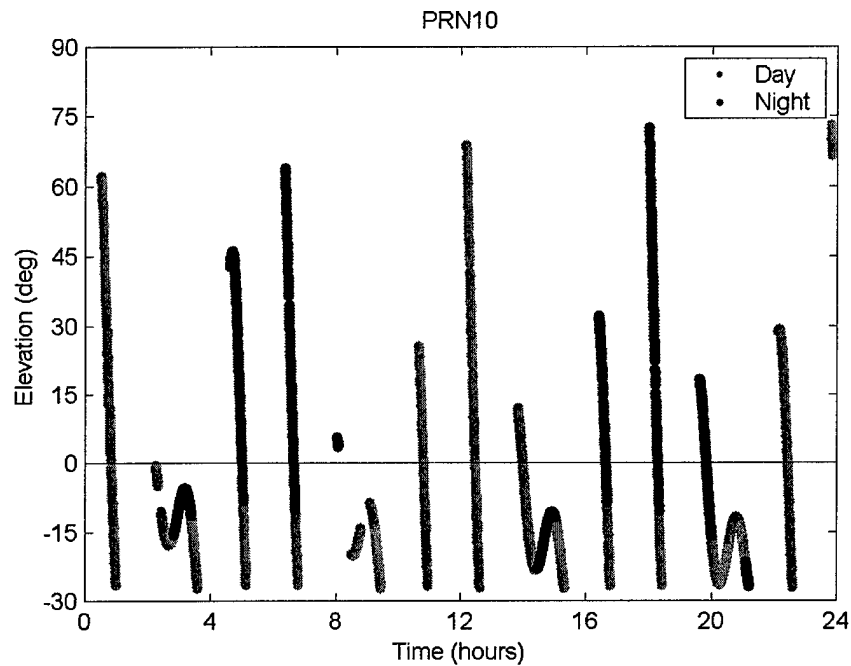


Figure 4.5 – PRN10 GPS/MET Elevation Plot

Most of the GPS tracking arcs start with GPS satellites at their highest elevation with respect to GPS/MET. Therefore, the assumption that $\Delta\rho_{ion_1}^0 \approx 0$ is possible since the change in range due to ionospheric effects is lowest when the GPS spacecraft are at their highest elevation. Figure 4.6 shows a plot of the dual frequency ionospheric correction at the start of each tracking arc. With zero bias DRVID the “bias” at the start of each tracking arc is assumed to be zero. However, Figure 4.6 shows the mean of the bias at the start of each tracking arc is 2.12 m with several significant outliers. The two largest outliers are with PRNs 29 and 16. Figure 4.3 shows the elevation plot for PRN29 and Figure 4.2 shows the elevation plot for PRN16. As seen in the figures, the outliers are caused by breaks in the tracking arcs. At the time of each of these tracking arc breaks a

cycle slip occurs on the phase measurement introducing a new integer ambiguity.

Cycle slips also disrupt the DRVID calculations since the phase measurement does not have the same integer ambiguity from one epoch to the next. The outliers for PRNs 10 and 14 are similarly explained. Also see Figure 4.4 and Figure 4.5.

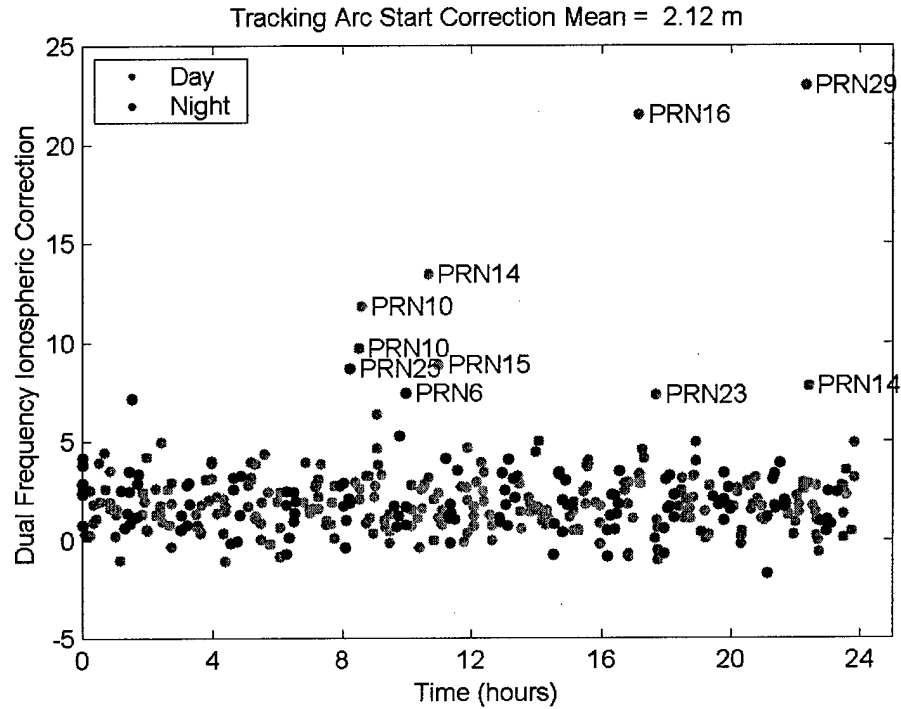


Figure 4.6 – Dual Frequency Ionospheric Correction at GPS Tracking Arc Start

If $\Delta\rho_{ion_i}^0 \approx 0$ is assumed, equation (4.25) becomes,

$$\Delta\rho_{ion_i}^k = \frac{(\rho_{P_{L_i}}^k - \rho_{P_{L_i}}^0) - (\phi_{L_{L_i}}^k - \phi_{L_{L_i}}^0) \frac{c}{f}}{2} \quad (4.26)$$

Now the change in range due to ionospheric effects can be approximated without the additional computational burden of estimating integer ambiguities in the state

or by estimating the initial $\Delta\rho_{ion_i}^0$ bias. To apply this model to spacecraft other than GPS/MET, application of the DRVID ionospheric correction should only take place when the elevation from the user satellite to the GPS satellite begins decreasing and when the elevation decrease begins at high elevation angles.

Results of estimating $\Delta\rho_{ion_i}^k$ using DRVID on the GPS/MET data are shown in the last column of Table 4.1. The zero bias DRVID estimation technique suffered only a 0.833 meter error compared to the model bias technique. Figure 4.7 shows a plot of the largest zero bias DRVID errors compared to dual frequency shown in Table 4.1 and Figure 4.8 shows the smallest zero bias DRVID errors shown in Table 4.1.

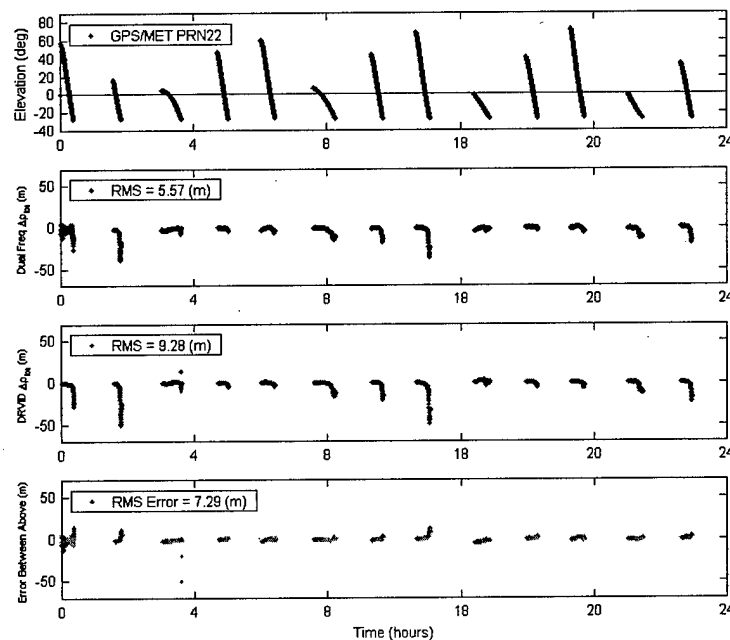


Figure 4.7 - PRN 22 Zero Bias DRVID, Dual Frequency Comparison

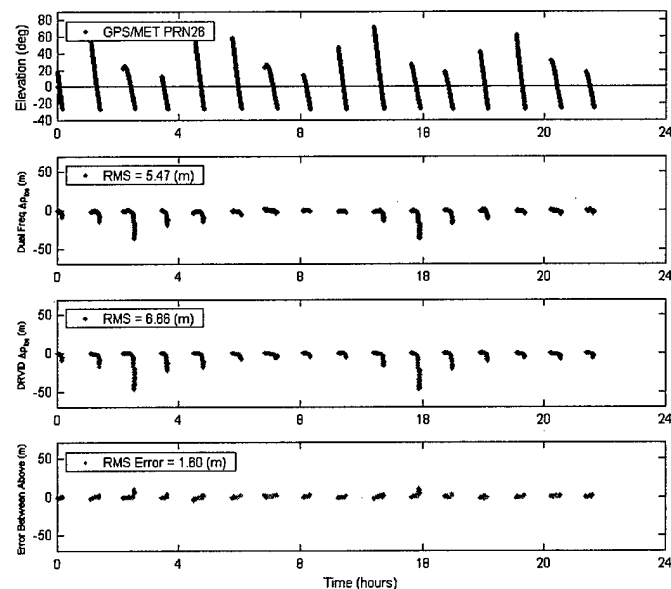


Figure 4.8 - PRN 23 Zero Bias DRVID, Dual Frequency Comparison

4.3 DRVID in GEODE

The implementation of DRVID in GEODE requires significant bookkeeping of the GPS/MET to GPS satellite elevation angles. To ensure the measurement epoch with the smallest ionospheric error is chosen to provide $\rho_{P_{L_i}}^0$ and $\phi_{L_{L_i}}^0$ for equation (4.26), the elevation angle and the phase and pseudorange measurements from the previous measurement epoch must be available at the current epoch. Then, the previous elevation can be compared to the current elevation and when the current elevation is smaller than the previous elevation, $\rho_{P_{L_i}}^0$ and $\phi_{L_{L_i}}^0$ are recorded. Then, the previous epoch is the zero bias point. Care must also be taken to ensure cycle slips in the phase measurements

are detected during any given tracking arc. If a cycle slip occurs, the zero bias point must be reset.

Figure 4.9 shows an example tracking case where the GPS satellite elevation with respect to the user satellite starts at 85° at time 1, then increases to 90° at time 2 and back to 85° at time 3. In this case, the pseudorange and phase measurements from time 2 will be used as ρ_{PI}^0 and ϕ_{LI}^0 . The measurements at time 1 and time 2 will be treated as a single frequency. DRVID will be applied to the measurement at time 3.

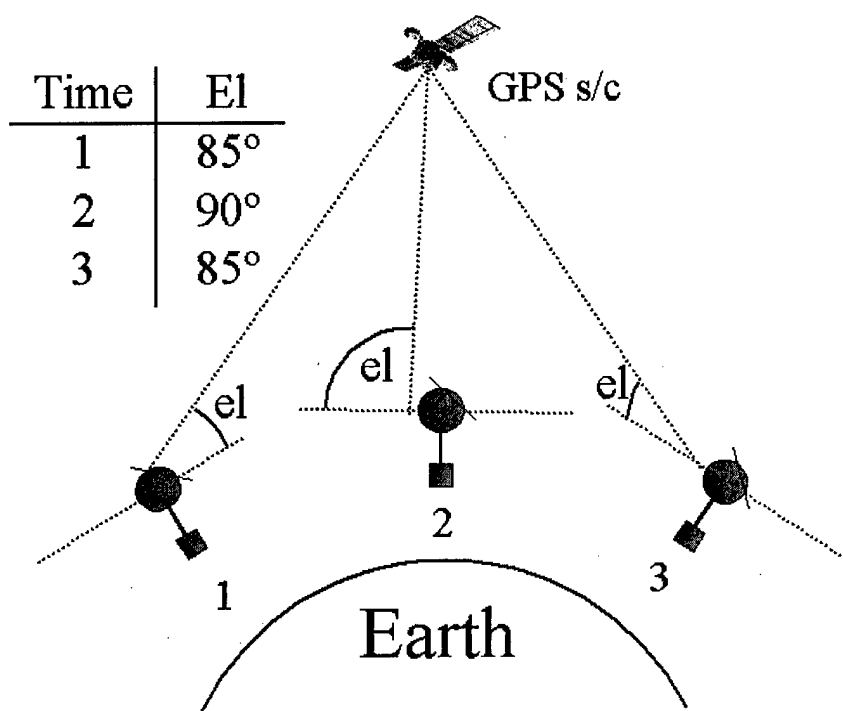


Figure 4.9 – DRVID Elevation Angle Example

Figure 4.10 shows a plot of DRVID ionospheric correction estimates compared to dual frequency corrections in GEODE. DRVID appropriately

estimated the necessary ionospheric corrections in most cases. PRNs 5, 27 and 16, cause the outliers near hours 11, 14 and 17 respectively. Figure 4.12 through Figure 4.14 show the relationship between the elevation angle and the error between the dual frequency ionospheric correction and the DRVID ionospheric correction. In each case a break in the tracking arc and cycle slip occurs so the zero point is reset. Since the breaks occur at low elevations, single frequency measurements are used for the remainder of the tracking arcs. The vertical lines on Figure 4.12 through Figure 4.14 indicate when the satellite is in sunlight and darkness. The narrow regions are darkness.

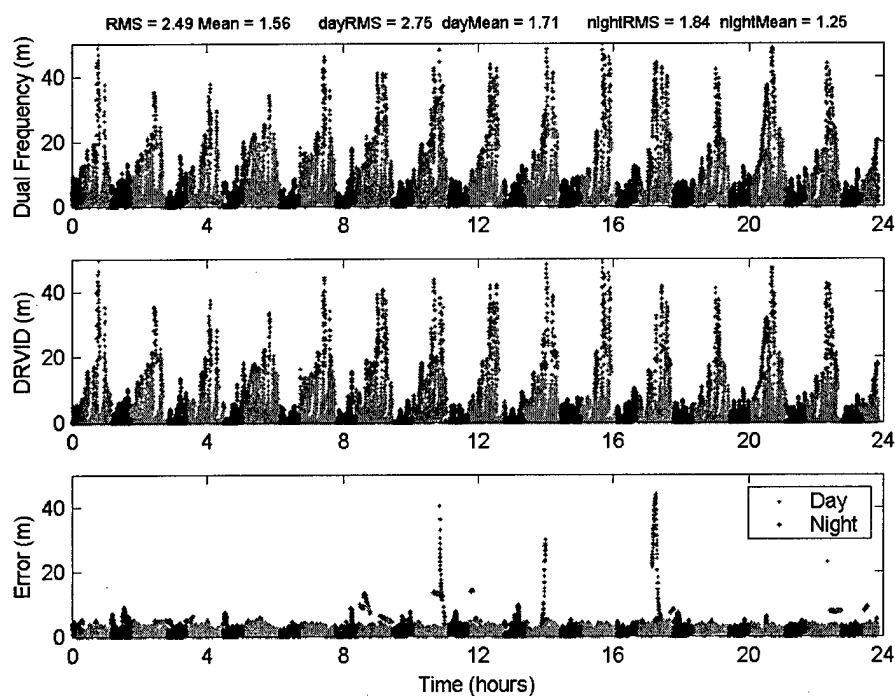


Figure 4.10 – 4 Feb 1997 GPS/MET DRVID Dual Frequency Comparison

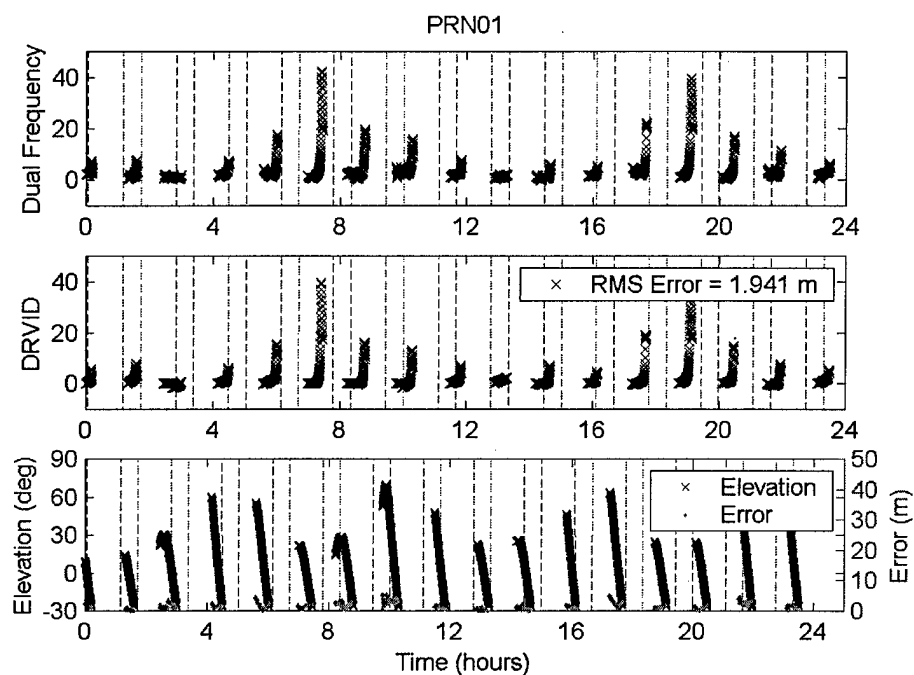


Figure 4.11 – PRN01 GPS/MET DRVID in GEODE

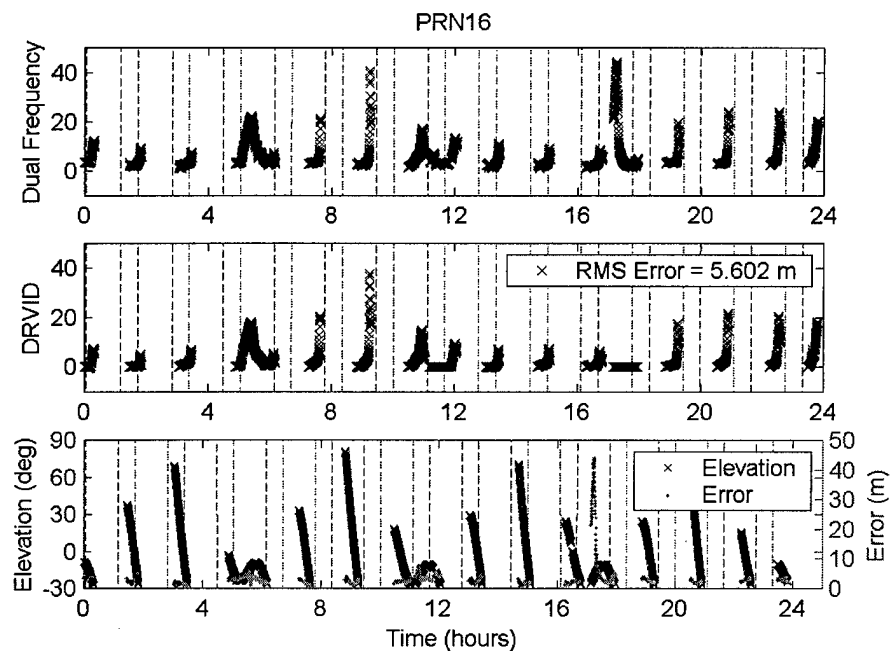


Figure 4.12 – PRN16 GPS/MET DRVID in GEODE

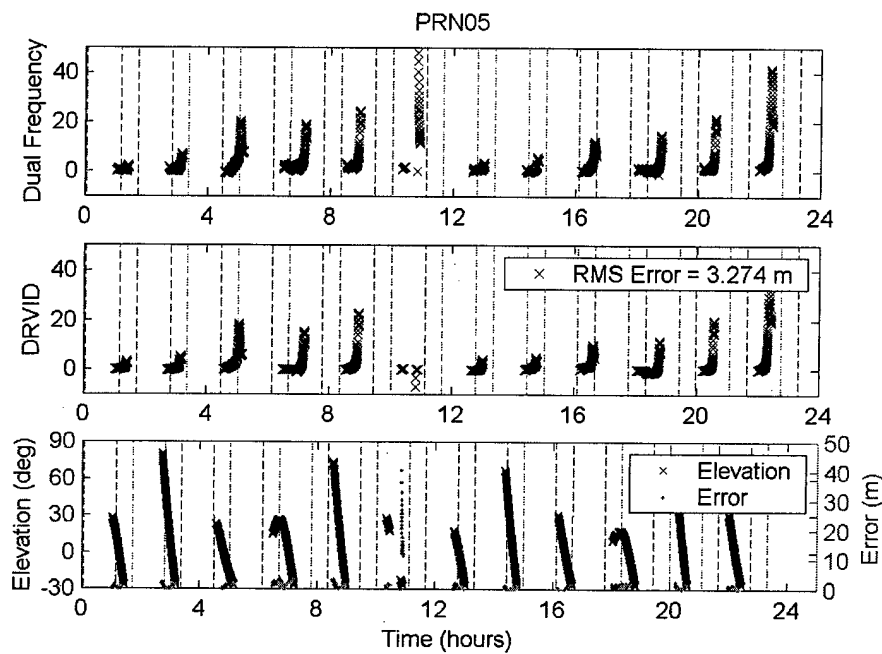


Figure 4.13 - PRN05 GPS/MET DRVID in GEODE

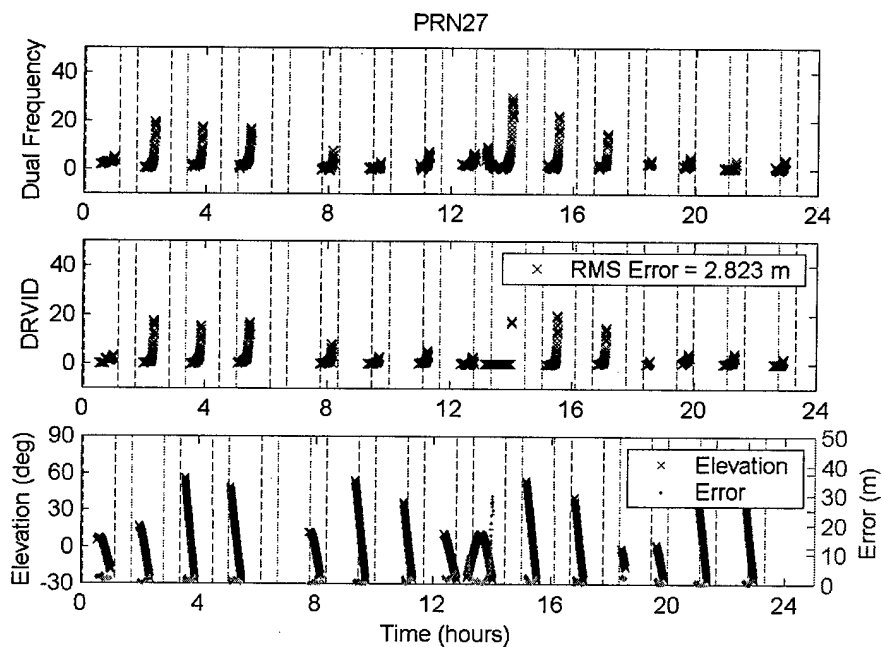


Figure 4.14 - PRN27 GPS/MET DRVID in GEODE

4.3.1 DRVID in GEODE Results

The application of the zero bias DRVID technique to the GPS/MET data in GEODE leads to an accuracy improvement close to the improvement realized using dual frequency data. Table 4.2 shows a comparison between the single frequency, dual frequency and DRVID results for the 4 Feb 1997 data. DRVID improves the 3D RSS error by 4.2% for the case without high rate clocks and 4.5% with high rate clocks. Additional GPS/MET DRVID results are presented in Chapters 5 and 6.

Table 4.2 – GEODE With Ionospheric Correction for GPS/MET

GPS/MET - 4 Feb 1997	Error Mean (m)			RMS Error (m)			
	R	I	C	R	I	C	3D
Without High Rate GPS Clocks							
Single Frequency	0.55	-0.99	-0.10	2.74	10.24	2.15	10.81
Dual Frequency	0.11	2.04	-0.11	2.48	9.68	2.12	10.21
DRVID	0.24	-1.14	-0.11	2.63	9.72	2.23	10.32
With High Rate GPS Clocks							
Single Frequency	0.28	-3.59	-0.04	2.22	7.23	0.77	7.60
Dual Frequency	-0.08	-1.38	-0.04	2.10	6.14	0.86	6.55
DRVID	-0.03	-3.54	-0.04	1.97	6.95	0.90	7.28

Zero bias DRVID ionospheric corrections are also applied to the SA free T/P data. Table 4.3 shows the 3 cm 3D RSS position error improvement. The reason the accuracy improvement is proportionally smaller (only 2.5%) than the improvement realized on the GPS/MET data is the ionospheric effects on the T/P data are smaller due to T/P's higher orbit.

Table 4.3 – GEODE With Ionospheric Correction for T/P

T/P – 5 May 2000	Error Mean (m)			RMS Error (m)			
	R	I	C	R	I	C	3D
Single Frequency	0.21	-0.04	0.01	0.35	1.06	0.44	1.20
DRVID	0.20	0.01	0.01	0.35	1.02	0.45	1.17

While the error RMS and RSS improvements are near those of using dual frequency ionospheric corrections, a comparison of the execution time required by GEODE with and without DRVID shows a 12.1% computational burden increase. This significant increase is a result of the need to calculate and store the elevation angle for each satellite being tracked at every measurement epoch. Calculating the GPS elevation angle requires computation of the position of each GPS satellite in view, therefore, the GPS satellite ephemerides must be evaluated for each elevation calculation. The computational burden is reduced significantly if all satellites in view are processed for the measurement update (ALL) instead of cyclically.

4.4 Summary

Differenced Range Versus Integrated Doppler (DRVID) [29] is a technique utilizing the difference in the way the pseudorange and phase measurements are affected by the ionosphere. Since the ionosphere advances phase and delays range measurements, a linear combination of both measurements can remove ionospheric errors to first order.

There are three methods by which DRVID can be applied to estimate GPS pseudorange ionospheric corrections. First, the phase integer ambiguity can be

estimated as part of the state. Integer ambiguity resolution is not suited to real-time systems and therefore is not considered here. The second application of DRVID involves estimation of an initial ionospheric bias correction using a model such as JPL's GIM. Model bias estimation shows promise, but the overhead involved in generating the bias estimates and updating the model is probably unreasonable for a real-time system. Application of the zero bias DRVID technique to estimate the GPS pseudorange ionospheric correction results in an accuracy/precision improvement over using single frequency measurements with no ionospheric correction. The zero bias DRVID technique provides accuracy very near dual frequency correction but with a 12.1% increase in computational burden.

CHAPTER 5

Dynamic Model Compensation (DMC)

The dynamic models used to propagate satellite ephemeris are always approximations of the actual forces acting on the satellite. No matter how detailed and precise, models will always fall short of describing the real dynamics. In real-time satellite OD the dynamic model is used to propagate the satellite's position and velocity between measurement epochs. The dynamic model might also be used to propagate the satellite's ephemeris for prediction purposes. If the dynamic model does not predict the satellite's motion accurately enough, the filter in an OD scheme can diverge. Care needs to be taken, in a real-time OD system to balance the accuracy requirements of the time update of the state with the overhead of the propagator. In choosing a finite approximation of the satellite dynamics there will always be forces in the dynamic model that will be unmodeled or mismodeled.

Dynamic Model Compensation (DMC) is a process noise formulation that assumes a dynamical system is subject to accelerations not included in the systems dynamic model and which possess a random element [9]. These accelerations have been called "fictitious" [62], "augmenting", "compensative" [9] and "empirical"[4]. Regardless of what they are called, they are estimated in

the filter and their formulation includes the development of process noise covariance values. DMC was used as early as the 1970's [63] but the formulation shown here follows the derivation in Cruickshank [64] and [9].

In this chapter, DMC is first introduced through a simple one-dimensional example. Then the development is extended to the three-dimensional satellite OD problem where accelerations are estimated in Cartesian XYZ coordinates. Next, DMC is refined and accelerations are estimated in Radial, In-track and Cross-track (RIC) coordinates. Finally, XYZ and RIC DMC are employed in two simulations and in GEODE and accuracy/precision and computational burden results are presented.

5.1 Dynamic Model Compensation (DMC)

Suppose the particle in Figure 5.1 is moving with constant velocity and the particle's position is to be estimated from range observations.

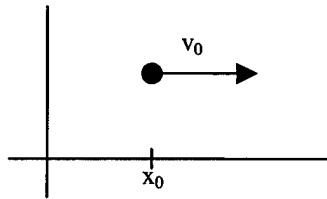


Figure 5.1 – Particle Moving at Constant Velocity

The dynamic model for this system can be expressed in state space form as:

$$\bar{X} = \begin{bmatrix} x \\ \dot{x} \end{bmatrix} = \begin{bmatrix} x_0 + v_0(t - t_0) \\ v_0 \end{bmatrix} \quad (5.1)$$

leading to the derivative in state space form.

$$\dot{\bar{X}} = A\bar{X} = \begin{bmatrix} 0 & 1 \\ 0 & 0 \end{bmatrix} \begin{bmatrix} x \\ \dot{x} \end{bmatrix} \quad (5.2)$$

The state transition matrix for this simple system is formed from

$$\dot{\Phi}(t, t_0) = A\Phi(t, t_0) \quad (5.3)$$

where the initial condition is $\Phi(t_0, t_0) = I$. A method of calculating the state

transition matrix for this simple system is Laplace transforms. Here

$$\Phi(t, t_0) = L^{-1}[(sI - A)^{-1}] \quad (5.4)$$

The state transition matrix is therefore

$$\Phi(t, t_0) = \begin{bmatrix} 1 & (t - t_0) \\ 0 & 1 \end{bmatrix} \quad (5.5)$$

If stochastic forces perturb the movement of the particle, either random (possibly time correlated) and/or deterministic, estimation under the constant velocity assumption is not optimal. DMC can be used to improve estimation performance in such a situation. Assume that the unmodeled acceleration $\omega(t)$ can be modeled as a first order Gauss-Markov process

$$\dot{\omega}(t) = \beta\omega(t) + u(t) \quad (5.6)$$

where:

$\omega(t) \equiv$ compensative acceleration

$u(t) \equiv$ uncorrelated, stationary Gaussian process (white noise) with $E[u] = 0$ and $E[u^T u] = \sigma_u^2$ (standard deviation of the forcing noise)

$\beta \equiv \frac{1}{\tau}$ where τ is the correlation time and is considered constant

Now the state can be augmented with the compensative acceleration

$$\bar{X} = \begin{bmatrix} x \\ \dot{x} \\ \omega \end{bmatrix} \quad (5.7)$$

and

$$\dot{\bar{X}} = \begin{bmatrix} \dot{x} \\ \omega \\ -\beta\omega + u(t) \end{bmatrix} = \begin{bmatrix} 0 & 1 & 0 \\ 0 & 0 & 1 \\ 0 & 0 & -\beta \end{bmatrix} \begin{bmatrix} x \\ \dot{x} \\ \omega \end{bmatrix} + \begin{bmatrix} 0 \\ 0 \\ 1 \end{bmatrix} u(t) = A\bar{X} + Bu(t) \quad (5.8)$$

The general solution, found using convolution, has both deterministic and random components

$$X(t) = \Phi_w(t, t_0)X(t_0) + \int_{t_0}^t \Phi_w(t, t_0)Bu(t)dt \quad (5.9)$$

$$\begin{array}{cc} \uparrow & \uparrow \\ \text{Deterministic} & \text{Random} \end{array}$$

The state transition matrix $\Phi_w(t, t_0)$ can again be found from $\dot{\Phi}(t, t_0) = A\Phi(t, t_0)$.

The Laplace transform method can again be used, but inverting a 3x3 or larger matrix can be a challenge. The Symbolic Toolbox in Matlab or Mathematica can easily be used for larger matrices.

$$\Phi_w(t, t_0) = \begin{bmatrix} 1 & \Delta t & \tau\Delta t + \tau^2(e^{-\Delta t/\tau} - 1) \\ 0 & 1 & \tau(1 - e^{-\Delta t/\tau}) \\ 0 & 0 & e^{-\Delta t/\tau} \end{bmatrix} \quad (5.10)$$

Assuming the initial stochastic state is

$$X(t_0) = \begin{bmatrix} 0 \\ 0 \\ \omega_0 \end{bmatrix} \quad (5.11)$$

the deterministic component of equation (5.9) is

$$\bar{X}_{\text{det}} = \Phi_w(t, t_0)X(t_0) = \begin{bmatrix} \omega_0 \tau \Delta t + \omega_0 \tau^2 (e^{-\Delta t/\tau} - 1) \\ \omega_0 \tau (1 - e^{-\Delta t/\tau}) \\ \omega_0 e^{-\Delta t/\tau} \end{bmatrix} \quad (5.12)$$

Now the state propagation model is also augmented and the deterministic portion of (5.9) is included.

$$\bar{X}(t) = \begin{bmatrix} x(t) \\ \dot{x}(t) \\ \omega(t) \end{bmatrix} = \begin{bmatrix} \omega_0 \tau \Delta t + \omega_0 \tau^2 (e^{-\Delta t/\tau} - 1) + v_0 \Delta t + x_0 \\ \omega_0 \tau (1 - e^{-\Delta t/\tau}) + v_0 \\ \omega_0 e^{-\Delta t/\tau} \end{bmatrix} \quad (5.13)$$

The process noise covariance can be formulated from the random terms in (5.9),

i.e. $\int_{t_0}^t \Phi_w(t, \tau) B u(\tau) d\tau$. The calculation of the process noise covariance matrix

over the time interval $\Delta t = t - t_0$ is:

$$Q_w = \int_{t_0}^t \Phi_w(t, \tau) B E[u(\tau)u^T(\tau)] B^T \Phi_w^T(t, \tau) d\tau \quad (5.14)$$

or since $E[u(\tau)u^T(\tau)] = \sigma_u^2$

$$Q_w = \int_{t_0}^t \Phi_w(t, \tau) B \sigma_u^2 B^T \Phi_w^T(t, \tau) d\tau \quad (5.15)$$

where τ is the time integration variable, not the stochastic process correlation time. The resulting integral is:

$$Q_w = \int_{t_0}^t \begin{bmatrix} \tau(t-T) + \tau^2 (e^{-(t-T)/\tau} - 1) \\ \tau (e^{-(t-T)/\tau}) \\ e^{-(t-T)/\tau} \end{bmatrix} \begin{bmatrix} \tau(t-T) + \tau^2 (e^{-(t-T)/\tau} - 1) \\ \tau (e^{-(t-T)/\tau}) \\ e^{-(t-T)/\tau} \end{bmatrix}^T dT \quad (5.16)$$

where T is substituted for the time integration variable τ .

Evaluation of the integral in equation (5.16) results in:

$$Q_w = \begin{bmatrix} Q_{w(1,1)} & Q_{w(1,2)} & Q_{w(1,3)} \\ Q_{w(2,1)} & Q_{w(2,2)} & Q_{w(2,3)} \\ Q_{w(3,1)} & Q_{w(3,2)} & Q_{w(3,3)} \end{bmatrix} \quad (5.17)$$

where:

$$\begin{aligned} Q_{w(1,1)} &= \sigma_u^2 \left(\frac{1}{2} \tau^5 (1 - e^{-2\Delta t/\tau}) + \tau^4 \Delta t (1 - e^{-\Delta t/\tau}) - \tau^3 \Delta t^2 + \frac{1}{3} \tau^2 \Delta t^3 \right) \\ Q_{w(1,2)} &= Q_{w(2,1)} = \sigma_u^2 \left(\tau^4 \left(\frac{1}{2} - e^{-\Delta t/\tau} + \frac{1}{2} e^{-2\Delta t/\tau} \right) - \tau^3 \Delta t (1 - e^{-\Delta t/\tau}) + \frac{1}{2} \tau^2 \Delta t^2 \right) \\ Q_{w(2,2)} &= \sigma_u^2 \left(\tau^3 \left(-\frac{3}{2} + 2e^{-\Delta t/\tau} - \frac{1}{2} e^{-2\Delta t/\tau} \right) + \tau^2 \Delta t \right) \\ Q_{w(1,3)} &= Q_{w(3,1)} = \sigma_u^2 \left(\frac{1}{2} \tau^3 (1 - e^{-2\Delta t/\tau}) - \tau^2 \Delta t e^{-\Delta t/\tau} \right) \\ Q_{w(3,2)} &= Q_{w(2,3)} = \sigma_u^2 \tau^2 \left(\frac{1}{2} (1 + e^{-2\Delta t/\tau}) - e^{-\Delta t/\tau} \right) \\ Q_{w(3,3)} &= \frac{\sigma_u^2}{2} \tau (1 - e^{-2\Delta t/\tau}) \end{aligned} \quad (5.18)$$

Addition of the process noise covariance to an Extended Kalman Filter

(EKF) is rudimentary. The algorithm is unchanged except for the time update of the state error covariance \bar{P}_k [Born, 2000 #252]. The new formulation for \bar{P}_k is:

$$\bar{P}_{k+1} = \Phi(t_{k+1}, t_k) P_k \Phi^T(t_{k+1}, t_k) + Q_w \quad (5.19)$$

$\Delta t = t_{k+1} - t_k$ in the formulation of Q_w .

The application of DMC to a real-time satellite OD system using GPS is more complex since the state includes constants from the dynamic model, receiver clock bias and receiver clock drift terms. Therefore, the state transition matrix

and process noise covariance matrices explained above are updated in section 5.2 to include the additional terms.

5.2 XYZ DMC

The XYZ DMC derivation shown below follows closely the derivation in Cruickshank [9]. As shown in equation (5.6) the stochastic accelerations are modeled dynamically by a Langevin equation [9]. Now β in equation (5.6) becomes:

$$\beta = \begin{bmatrix} 1/\tau & 0 & 0 \\ 0 & 1/\tau & 0 \\ 0 & 0 & 1/\tau \end{bmatrix} \quad (5.20)$$

The Gaussian process, $u(t)$, is uncorrelated in time with zero mean but now has constant variance of:

$$q_u = \begin{bmatrix} \sigma_u^2 & 0 & 0 \\ 0 & \sigma_u^2 & 0 \\ 0 & 0 & \sigma_u^2 \end{bmatrix} \quad (5.21)$$

β and q_u are assumed diagonal for convenience only, indicating the accelerations in the three directions are uncorrelated with each other. τ and σ_u are also assumed equal in each of the three directions [9].

The state vector is augmented with the compensative accelerations, ω_x , ω_y , ω_z as shown in equation (5.22). The deterministic components augment the time propagation of the state as in equation (5.23).

The original
state vector in
GEODE

New state vector

New state augmented with deterministic portion of
compensative accelerations

$$\begin{aligned}
 X &= \begin{bmatrix} x \\ y \\ z \\ \dot{x} \\ \dot{y} \\ \dot{z} \\ C_D \\ C_R \\ b \\ \dot{b} \\ \omega_x \\ \omega_y \\ \omega_z \end{bmatrix}_{10 \times 1} & X &= \begin{bmatrix} x \\ y \\ z \\ \dot{x} \\ \dot{y} \\ \dot{z} \\ C_D \\ C_R \\ b \\ \dot{b} \\ \omega_x \\ \omega_y \\ \omega_z \end{bmatrix}_{13 \times 1} & (5.22) & X = \begin{bmatrix} x + \omega_x \tau \Delta t + \omega_x \tau^2 (e^{-\Delta t/\tau} - 1) \\ y + \omega_y \tau \Delta t + \omega_y \tau^2 (e^{-\Delta t/\tau} - 1) \\ z + \omega_z \tau \Delta t + \omega_z \tau^2 (e^{-\Delta t/\tau} - 1) \\ \dot{x} + \omega_x \tau (1 - e^{-\Delta t/\tau}) \\ \dot{y} + \omega_y \tau (1 - e^{-\Delta t/\tau}) \\ \dot{z} + \omega_z \tau (1 - e^{-\Delta t/\tau}) \\ C_D \\ C_R \\ b \\ \dot{b} \\ \omega_{x_{k-1}} e^{-\Delta t/\tau} \\ \omega_{y_{k-1}} e^{-\Delta t/\tau} \\ \omega_{z_{k-1}} e^{-\Delta t/\tau} \end{bmatrix}_{13 \times 1} & (5.23)
 \end{aligned}$$

5.2.1 XYZ DMC State Transition Matrix

The state transition matrix is also augmented to include the compensative acceleration terms.

$$\Phi = \begin{bmatrix} [\Phi_X]_{10 \times 10} & [\Phi_{\omega RV}]_{10 \times 3} \\ [0]_{3 \times 10} & [\Phi_\omega]_{3 \times 3} \end{bmatrix} \quad \Phi \equiv \frac{\partial X}{\partial X_0} \quad (5.24)$$

The state transition matrix of the original state is shown in equation (5.25) and is developed in Lee [37].

$$\Phi_x = \begin{bmatrix} \begin{bmatrix} \frac{\partial \bar{R}(t_k)}{\partial \bar{R}(t_{k-1})} \end{bmatrix}_{3 \times 3} & \begin{bmatrix} \frac{\partial \bar{R}(t_k)}{\partial \dot{\bar{R}}(t_{k-1})} \end{bmatrix}_{3 \times 3} & \begin{bmatrix} \frac{\partial \bar{R}(t_k)}{\partial \Delta C_D(t_{k-1})} \end{bmatrix}_{3 \times 1} & \begin{bmatrix} \frac{\partial \bar{R}(t_k)}{\partial \Delta C_R(t_{k-1})} \end{bmatrix}_{3 \times 1} & [0]_{3 \times 2} \\ \begin{bmatrix} \frac{\partial \dot{\bar{R}}(t_k)}{\partial \bar{R}(t_{k-1})} \end{bmatrix}_{3 \times 3} & \begin{bmatrix} \frac{\partial \dot{\bar{R}}(t_k)}{\partial \dot{\bar{R}}(t_{k-1})} \end{bmatrix}_{3 \times 3} & \begin{bmatrix} \frac{\partial \dot{\bar{R}}(t_k)}{\partial \Delta C_D(t_{k-1})} \end{bmatrix}_{3 \times 1} & \begin{bmatrix} \frac{\partial \dot{\bar{R}}(t_k)}{\partial \Delta C_R(t_{k-1})} \end{bmatrix}_{3 \times 1} & [0]_{3 \times 2} \\ [0]_{1 \times 3} & [0]_{1 \times 3} & \begin{bmatrix} \frac{\partial \Delta C_D(t_k)}{\partial \Delta C_D(t_{k-1})} \end{bmatrix}_{1 \times 1} & 0 & [0]_{1 \times 2} \\ [0]_{1 \times 3} & [0]_{1 \times 3} & 0 & \begin{bmatrix} \frac{\partial \Delta C_R(t_k)}{\partial \Delta C_R(t_{k-1})} \end{bmatrix}_{1 \times 1} & [0]_{1 \times 2} \\ [0]_{2 \times 3} & [0]_{2 \times 3} & [0]_{2 \times 1} & [0]_{2 \times 1} & \begin{bmatrix} \frac{\partial \Delta \bar{b}(t_k)}{\partial \Delta \bar{b}(t_{k-1})} \end{bmatrix}_{2 \times 2} \end{bmatrix}$$

(5.25)

The state transition matrix of the compensative accelerations with respect to themselves:

$$\Phi_\omega = \begin{bmatrix} \frac{\partial \omega_x}{\partial \omega_{x_0}} & \frac{\partial \omega_x}{\partial \omega_{y_0}} & \frac{\partial \omega_x}{\partial \omega_{c_0}} \\ \frac{\partial \omega_y}{\partial \omega_{x_0}} & \frac{\partial \omega_y}{\partial \omega_{y_0}} & \frac{\partial \omega_y}{\partial \omega_{c_0}} \\ \frac{\partial \omega_z}{\partial \omega_{x_0}} & \frac{\partial \omega_z}{\partial \omega_{y_0}} & \frac{\partial \omega_z}{\partial \omega_{c_0}} \end{bmatrix} = \begin{bmatrix} e^{-\Delta t/\tau} & 0 & 0 \\ 0 & e^{-\Delta t/\tau} & 0 \\ 0 & 0 & e^{-\Delta t/\tau} \end{bmatrix} \quad (5.26)$$

Again,

$$\Delta t = t_{k+1} - t_k$$

The state transition matrix of the compensative accelerations with respect to the original state is:

$$\Phi_{\omega RV} = \begin{bmatrix} \left[\frac{\partial \bar{\Gamma}}{\partial \bar{\omega}} \right]_{3 \times 3} \\ \left[\frac{\partial \dot{\bar{\Gamma}}}{\partial \bar{\omega}} \right]_{3 \times 3} \\ \left[\frac{\partial C_D}{\partial \bar{\omega}} \right]_{1 \times 3} \\ \left[\frac{\partial C_R}{\partial \bar{\omega}} \right]_{1 \times 3} \\ \left[\frac{\partial \bar{b}}{\partial \bar{\omega}} \right]_{1 \times 3} \\ \left[\frac{\partial \dot{\bar{b}}}{\partial \bar{\omega}} \right]_{1 \times 3} \end{bmatrix} = \begin{bmatrix} \left[\frac{\partial \bar{\Gamma}}{\partial \bar{\omega}} \right]_{3 \times 3} \\ \left[\frac{\partial \dot{\bar{\Gamma}}}{\partial \bar{\omega}} \right]_{3 \times 3} \\ [0]_{4 \times 3} \end{bmatrix} = \begin{bmatrix} [\Phi_{\omega R}]_{3 \times 3} \\ [\Phi_{\omega V}]_{3 \times 3} \\ [0]_{4 \times 3} \end{bmatrix} \quad (5.27)$$

$$[\Phi_{\omega R}] = \frac{\partial \bar{\Gamma}}{\partial \bar{\omega}_0} = \begin{bmatrix} \frac{\partial x}{\partial \omega_{x_0}} & \frac{\partial x}{\partial \omega_{y_0}} & \frac{\partial x}{\partial \omega_{z_0}} \\ \frac{\partial y}{\partial \omega_{x_0}} & \frac{\partial y}{\partial \omega_{y_0}} & \frac{\partial y}{\partial \omega_{z_0}} \\ \frac{\partial z}{\partial \omega_{x_0}} & \frac{\partial z}{\partial \omega_{y_0}} & \frac{\partial z}{\partial \omega_{z_0}} \end{bmatrix} \quad (5.28)$$

and

$$[\Phi_{\omega V}] = \frac{\partial \dot{\bar{\Gamma}}}{\partial \bar{\omega}_0} = \begin{bmatrix} \frac{\partial \dot{x}}{\partial \omega_{x_0}} & \frac{\partial \dot{x}}{\partial \omega_{y_0}} & \frac{\partial \dot{x}}{\partial \omega_{z_0}} \\ \frac{\partial \dot{y}}{\partial \omega_{x_0}} & \frac{\partial \dot{y}}{\partial \omega_{y_0}} & \frac{\partial \dot{y}}{\partial \omega_{z_0}} \\ \frac{\partial \dot{z}}{\partial \omega_{x_0}} & \frac{\partial \dot{z}}{\partial \omega_{y_0}} & \frac{\partial \dot{z}}{\partial \omega_{z_0}} \end{bmatrix} \quad (5.29)$$

Therefore,

$$\Phi_{\omega RV} = \begin{bmatrix} \Delta t \tau + \tau^2 (e^{-\Delta t/\tau} - 1) & 0 & 0 \\ 0 & \Delta t \tau + \tau^2 (e^{-\Delta t/\tau} - 1) & 0 \\ 0 & 0 & \Delta t \tau + \tau^2 (e^{-\Delta t/\tau} - 1) \\ \tau (1 - e^{-\Delta t/\tau}) & 0 & 0 \\ 0 & \tau (1 - e^{-\Delta t/\tau}) & 0 \\ 0 & 0 & \tau (1 - e^{-\Delta t/\tau}) \\ \begin{bmatrix} 0 & 0 & 0 \\ 0 & 0 & 0 \\ 0 & 0 & 0 \\ 0 & 0 & 0 \end{bmatrix} \end{bmatrix} \quad (5.30)$$

5.2.2 XYZ DMC Process Noise Covariance

The process noise covariance matrix, Q_{xyz} , is propagated over the time interval t_0 to t through evaluation of the integral in equation (5.31).

$$Q_{xyz} = \begin{bmatrix} \sigma_u^2 & 0 & 0 \\ 0 & \sigma_u^2 & 0 \\ 0 & 0 & \sigma_u^2 \end{bmatrix} \int_{t_0}^t \Phi(t, T) B B^T \Phi^T(t, T) dT \quad (5.31)$$

Here, B is a matrix of the form:

$$B = \begin{bmatrix} 0 & 0 & 0 & 0 & 0 & 0 & 0 & 0 & 0 & 0 & 1 & 0 & 0 \\ 0 & 0 & 0 & 0 & 0 & 0 & 0 & 0 & 0 & 0 & 0 & 1 & 0 \\ 0 & 0 & 0 & 0 & 0 & 0 & 0 & 0 & 0 & 0 & 0 & 0 & 1 \end{bmatrix}^T \quad (5.32)$$

Let

$$S = \begin{bmatrix} \sigma_u^2 & 0 & 0 \\ 0 & \sigma_u^2 & 0 \\ 0 & 0 & \sigma_u^2 \end{bmatrix} \quad (5.33)$$

Then the DMC contribution to Q_{xyz} becomes:

$$Q_{xyz} = S \int_{t_0}^t \begin{bmatrix} [\Phi_{\omega R}] [\Phi_{\omega R}]^T_{3 \times 3} & [\Phi_{\omega R}] [\Phi_{\omega V}]^T_{3 \times 3} & [0]_{3 \times 4} & [\Phi_{\omega R}] [\Phi_{\omega}]^T_{3 \times 3} \\ [\Phi_{\omega V}] [\Phi_{\omega R}]^T_{3 \times 3} & [\Phi_{\omega V}] [\Phi_{\omega V}]^T_{3 \times 3} & [0]_{3 \times 4} & [\Phi_{\omega V}] [\Phi_{\omega}]^T_{3 \times 3} \\ [0]_{4 \times 3} & [0]_{4 \times 3} & [0]_{4 \times 4} & [0]_{4 \times 3} \\ [\Phi_{\omega}] [\Phi_{\omega R}]^T_{3 \times 3} & [\Phi_{\omega}] [\Phi_{\omega V}]^T_{3 \times 3} & [0]_{3 \times 4} & [\Phi_{\omega}] [\Phi_{\omega}]^T_{3 \times 3} \end{bmatrix} dT$$

Now let

$$Q_{xyz} = \begin{bmatrix} Q_{xyz(1,1)} & Q_{xyz(1,2)} & [0]_{3 \times 4} & Q_{xyz(1,4)} \\ Q_{xyz(2,1)} & Q_{xyz(2,2)} & [0]_{3 \times 4} & Q_{xyz(2,4)} \\ [0]_{4 \times 3} & [0]_{4 \times 3} & Q_{other_{4 \times 4}} & [0]_{4 \times 3} \\ Q_{xyz(4,1)} & Q_{xyz(4,2)} & [0]_{3 \times 4} & Q_{xyz(4,4)} \end{bmatrix} \quad (5.34)$$

where the (3,3) sub-matrix Q_{other} , contains process noise contributions for C_D , C_R ,

b and \dot{b} . Also,

$$Q_{xyz(1,1)} = S \int_{t_0}^t [\Phi_{\omega R}] [\Phi_{\omega R}]^T_{3 \times 3} dT \quad (5.35)$$

The rest of Q_{xyz} is defined as in equation (5.35). Now

$$[\Phi_{\omega R}] [\Phi_{\omega R}]^T = [\Delta t \tau + \tau^2 (e^{-\Delta t/\tau} - 1)] [\Delta t \tau + \tau^2 (e^{-\Delta t/\tau} - 1)] I_{3 \times 3} \quad (5.36)$$

and the integral in equation (5.35) is evaluated yielding

$$Q_{xyz(1,1)} = \left(\frac{1}{2} \tau^5 (1 - e^{-2\Delta t/\tau}) + \tau^4 \Delta t (1 - e^{-\Delta t/\tau}) - \tau^3 \Delta t^2 + \frac{1}{3} \tau^2 \Delta t^3 \right) S \quad (5.37)$$

The other sub-matrices of equation (5.34) are determined in like fashion.

$$Q_{xyz(1,2)} = \left(\tau^4 \left(\frac{1}{2} - e^{-\Delta t/\tau} + \frac{1}{2} e^{-2\Delta t/\tau} \right) - \tau^3 \Delta t (1 - e^{-\Delta t/\tau}) + \frac{1}{2} \tau^2 \Delta t^2 \right) S \quad (5.38)$$

$$Q_{xyz(1,2)} = Q_{xyz(2,1)}$$

$$Q_{xyz(1,4)} = Q_{xyz(4,1)} = \left(\frac{1}{2} \tau^3 (1 - e^{-2\Delta t/\tau}) - \tau^2 \Delta t e^{-\Delta t/\tau} \right) S \quad (5.39)$$

$$Q_{xyz(2,2)} = \left(\tau_c^3 \left(-\frac{3}{2} + 2e^{-\Delta t/\tau} - \frac{1}{2} e^{-2\Delta t/\tau} \right) + \tau^2 \Delta t \right) S \quad (5.40)$$

$$Q_{xyz(2,4)} = Q_{xyz(4,2)} = \tau^2 \left(\frac{1}{2} (1 + e^{-2\Delta t/\tau}) - e^{-\Delta t/\tau} \right) S \quad (5.41)$$

$$Q_{xyz(4,4)} = \frac{1}{2} \tau (1 - e^{-2\Delta t/\tau}) S \quad (5.42)$$

The development of the Q_{other} matrix can be found in [37].

$$Q_{\text{other}} = \begin{bmatrix} \sigma_{\text{drag}}^2 \Delta t & 0 & 0 & 0 \\ 0 & \sigma_{\text{rad}}^2 \Delta t & 0 & 0 \\ 0 & 0 & \frac{\sigma_b^2 \Delta t^3}{3} + \sigma_b^2 \Delta t & \frac{\sigma_b^2 \Delta t^2}{2} \\ 0 & 0 & \frac{\sigma_b^2 \Delta t^2}{2} & \sigma_b^2 \Delta t \end{bmatrix} \quad (5.43)$$

5.3 Radial, In-track, Cross-track (RIC) DMC

The development that follows is motivated by the desire to estimate the compensative accelerations in the radial, in-track, and cross-track directions. RIC DMC also provides a more intuitive approach to tuning the time correlation coefficient (τ) and standard deviation of the forcing noise (σ_u). The state is, once again, augmented with the compensative accelerations as shown in equation (5.44). The deterministic portion of the compensative accelerations now must be rotated from the RIC frame to the XYZ frame to be added to the state. Equation

(5.46) shows the rotation of the position components and equation (5.47) shows the rotation of the velocity components.

The original state vector in GEODE

$$X = \begin{bmatrix} x \\ y \\ z \\ \dot{x} \\ \dot{y} \\ \dot{z} \\ C_D \\ C_R \\ b \\ \dot{b} \end{bmatrix}_{10 \times 1}$$

New state vector

$$X = \begin{bmatrix} x \\ y \\ z \\ \dot{x} \\ \dot{y} \\ \dot{z} \\ C_D \\ C_R \\ b \\ \dot{b} \\ \omega_R \\ \omega_I \\ \omega_C \end{bmatrix}_{13 \times 1} \quad (5.44)$$

New state augmented with deterministic portion of compensative accelerations

$$X = \begin{bmatrix} x + \Delta x \\ y + \Delta y \\ z + \Delta z \\ \dot{x} + \Delta \dot{x} \\ \dot{y} + \Delta \dot{y} \\ \dot{z} + \Delta \dot{z} \\ C_D \\ C_R \\ b \\ \dot{b} \\ \omega_{R_{k-1}} e^{-\Delta t / \tau_R} \\ \omega_{I_{k-1}} e^{-\Delta t / \tau_I} \\ \omega_{C_{k-1}} e^{-\Delta t / \tau_C} \end{bmatrix}_{13 \times 1} \quad (5.45)$$

$$\Delta \bar{r}_{xyz} = \begin{bmatrix} \Delta x \\ \Delta y \\ \Delta z \end{bmatrix} = T_{RIC \rightarrow xyz} \begin{bmatrix} \omega_R \tau_R \Delta t + \omega_R \tau_R^2 (e^{-\Delta t / \tau_R} - 1) \\ \omega_I \tau_I \Delta t + \omega_I \tau_I^2 (e^{-\Delta t / \tau_I} - 1) \\ \omega_C \tau_C \Delta t + \omega_C \tau_C^2 (e^{-\Delta t / \tau_C} - 1) \end{bmatrix} \quad (5.46)$$

$$\Delta \dot{\bar{r}}_{xyz} = \begin{bmatrix} \Delta \dot{x} \\ \Delta \dot{y} \\ \Delta \dot{z} \end{bmatrix} = T_{RIC \rightarrow xyz} \begin{bmatrix} \omega_R \tau_R (1 - e^{-\Delta t / \tau_R}) \\ \omega_I \tau_I (1 - e^{-\Delta t / \tau_I}) \\ \omega_C \tau_C (1 - e^{-\Delta t / \tau_C}) \end{bmatrix} \quad (5.47)$$

$T_{RIC \rightarrow xyz}$ is the transformation matrix from RIC coordinates to xyz coordinates.

The equations describing $T_{RIC \rightarrow xyz}$ can be found in Lee [37].

5.3.1 RIC DMC State Transition Matrix

The $[\Phi_x]$ and $[\Phi_\omega]$ matrices are the same for the XYZ and RIC versions of the state transition matrix. However, the state transition matrix of the compensative accelerations with respect to the original state must be rotated to RIC coordinates.

Here,

$$\Phi_{\omega RV} = \begin{bmatrix} \left[\frac{\partial \bar{\Gamma}}{\partial \bar{\omega}} \right]_{3 \times 3} \\ \left[\frac{\partial \dot{\bar{\Gamma}}}{\partial \bar{\omega}} \right]_{3 \times 3} \\ \left[\frac{\partial \bar{C}_D}{\partial \bar{\omega}} \right]_{1 \times 3} \\ \left[\frac{\partial \bar{C}_R}{\partial \bar{\omega}} \right]_{1 \times 3} \\ \left[\frac{\partial \bar{b}}{\partial \bar{\omega}} \right]_{1 \times 3} \\ \left[\frac{\partial \dot{\bar{b}}}{\partial \bar{\omega}} \right]_{1 \times 3} \end{bmatrix} = \begin{bmatrix} \left[\frac{\partial \bar{\Gamma}}{\partial \bar{\omega}} \right]_{3 \times 3} \\ \left[\frac{\partial \dot{\bar{\Gamma}}}{\partial \bar{\omega}} \right]_{3 \times 3} \\ [0]_{4 \times 3} \end{bmatrix} = \begin{bmatrix} [\Phi_{\omega R}]_{3 \times 3} \\ [\Phi_{\omega V}]_{3 \times 3} \\ [0]_{4 \times 3} \end{bmatrix} \quad (5.48)$$

$$\frac{\partial \bar{\Gamma}}{\partial \bar{\omega}} = \frac{\partial \bar{\Gamma}}{\partial \bar{r}_{RIC}} \frac{\partial \bar{r}_{RIC}}{\partial \bar{\omega}} \quad (5.49)$$

$$\frac{\partial \bar{\Gamma}}{\partial \bar{\omega}} = T_{RIC \rightarrow xyz} \frac{\partial \bar{r}_{RIC}}{\partial \bar{\omega}} \quad (5.50)$$

$$\frac{\partial \bar{\Gamma}}{\partial \bar{\omega}} = T_{RIC \leftarrow xyz}^T \frac{\partial \bar{r}_{RIC}}{\partial \bar{\omega}} \quad (5.51)$$

with a similar derivation

$$\frac{\partial \dot{\vec{r}}}{\partial \vec{\omega}} = T_{\text{RIC} \leftarrow \text{xyz}}^T \frac{\partial \dot{\vec{r}}_{\text{RIC}}}{\partial \vec{\omega}} \quad (5.52)$$

therefore $\Phi_{\omega \text{RV}}$ becomes,

$$\Phi_{\omega \text{RV}} = \begin{bmatrix} T_{\text{RIC} \leftarrow \text{xyz}}^T \begin{bmatrix} \Delta t \tau_R + \tau_R^2 (e^{-\Delta t / \tau_R} - 1) & 0 & 0 \\ 0 & \Delta t \tau_I + \tau_I^2 (e^{-\Delta t / \tau_I} - 1) & 0 \\ 0 & 0 & \Delta t \tau_C + \tau_C^2 (e^{-\Delta t / \tau_C} - 1) \end{bmatrix} \\ T_{\text{RIC} \leftarrow \text{xyz}}^T \begin{bmatrix} \tau_R (1 - e^{-\Delta t / \tau_R}) & 0 & 0 \\ 0 & \tau_I (1 - e^{-\Delta t / \tau_I}) & 0 \\ 0 & 0 & \tau_C (1 - e^{-\Delta t / \tau_C}) \end{bmatrix} \\ \begin{bmatrix} 0 & 0 & 0 \\ 0 & 0 & 0 \\ 0 & 0 & 0 \\ 0 & 0 & 0 \end{bmatrix} \end{bmatrix} \quad (5.53)$$

and in simplified form:

$$\Phi_{\omega \text{RV}} = \begin{bmatrix} T_{\text{RIC} \leftarrow \text{xyz}}^T \Phi_{\omega \text{R}_{\text{RIC}}} \\ T_{\text{RIC} \leftarrow \text{xyz}}^T \Phi_{\omega \text{V}_{\text{RIC}}} \\ [0]_{4 \times 3} \end{bmatrix} = \begin{bmatrix} \Phi_{\omega \text{R}} \\ \Phi_{\omega \text{V}} \\ [0]_{4 \times 3} \end{bmatrix} \quad (5.54)$$

5.3.2 RIC DMC Process Noise Covariance

In RIC DMC separate standard deviations of the forcing noise (σ_s) are used instead of equal values on the diagonal as in XYZ DMC. Therefore, the S matrix takes the form

$$S = \begin{bmatrix} \sigma_R^2 & 0 & 0 \\ 0 & \sigma_I^2 & 0 \\ 0 & 0 & \sigma_C^2 \end{bmatrix} \quad (5.55)$$

causing Q_{RIC} to keep the form of equation (5.56) since the S matrix cannot be factored out.

$$Q_{RIC} = \int_{t_0}^t \begin{bmatrix} [\Phi_{\omega r}]S[\Phi_{\omega r}]_{3 \times 3}^T & [\Phi_{\omega r}]S[\Phi_{\omega v}]_{3 \times 3}^T & [0]_{3 \times 4} & [\Phi_{\omega r}]S[\Phi_{\omega}]_{3 \times 3}^T \\ [\Phi_{\omega v}]S[\Phi_{\omega r}]_{3 \times 3}^T & [\Phi_{\omega v}]S[\Phi_{\omega v}]_{3 \times 3}^T & [0]_{3 \times 4} & [\Phi_{\omega v}]S[\Phi_{\omega}]_{3 \times 3}^T \\ [0]_{4 \times 3} & [0]_{4 \times 3} & [0]_{4 \times 4} & [0]_{4 \times 3} \\ [\Phi_{\omega}]S[\Phi_{\omega r}]_{3 \times 3}^T & [\Phi_{\omega}]S[\Phi_{\omega v}]_{3 \times 3}^T & [0]_{3 \times 4} & [\Phi_{\omega}]S[\Phi_{\omega}]_{3 \times 3}^T \end{bmatrix} dT \quad (5.56)$$

With the new formulation of the state transition matrix, the upper left 3×3 sub-matrix of Q_{RIC} becomes:

$$\begin{aligned} [\Phi_{\omega r}]S[\Phi_{\omega r}]_{3 \times 3}^T &= [T_{RIC \leftarrow xyz}^T \Phi_{\omega R_{RIC}}]S[T_{RIC \leftarrow xyz}^T \Phi_{\omega R_{RIC}}]^T \\ [\Phi_{\omega r}]S[\Phi_{\omega r}]_{3 \times 3}^T &= [T_{RIC \leftarrow xyz}^T \Phi_{\omega R_{RIC}}]S[\Phi_{\omega R_{RIC}}^T T_{RIC \leftarrow xyz}] \\ [\Phi_{\omega r}]S[\Phi_{\omega r}]_{3 \times 3}^T &= [T_{RIC \leftarrow xyz}^T \Phi_{\omega R_{RIC}} S \Phi_{\omega R_{RIC}}^T T_{RIC \leftarrow xyz}] \end{aligned} \quad (5.57)$$

Since $\Phi_{\omega R_{RIC}}$ (defined in equations (5.53) and (5.54)) and S are both diagonal

$$[\Phi_{\omega r}]S[\Phi_{\omega r}]_{3 \times 3}^T = [T_{RIC \leftarrow xyz}^T S \Phi_{\omega R_{RIC}} \Phi_{\omega R_{RIC}}^T T_{RIC \leftarrow xyz}]$$

The same development applies to the other members of the Q_{RIC} matrix.

With $T_{RIC} = T_{RIC \leftarrow xyz}$, $Q_{RIC(1,1)}$ becomes

$$Q_{RIC(1,1)} = \int_{t_0}^t [T_{RIC}^T S \Phi_{\omega R_{RIC}} \Phi_{\omega R_{RIC}}^T T_{RIC}]_{3 \times 3} dT \quad (5.58)$$

Since the transformation matrix T_{RIC} and S are both independent of the variable of integration T ,

$$Q_{RIC(1,1)} = T_{RIC}^T S \left[\int_{t_0}^t [\Phi_{\omega R_{RIC}} \Phi_{\omega R_{RIC}}^T]_{3 \times 3} dT \right] T_{RIC} \quad (5.59)$$

Now let

$$Q_{(1,1)} = S \int_{t_0}^t \left[\Phi_{\omega R_{RIC}} \Phi_{\omega R_{RIC}}^T \right]_{3 \times 3} dT$$

and define Q as

$$Q = \begin{bmatrix} Q_{(1,1)} & Q_{(1,2)} & [0]_{3 \times 4} & Q_{(1,4)} \\ Q_{(2,1)} & Q_{(2,2)} & [0]_{3 \times 4} & Q_{(2,4)} \\ [0]_{4 \times 3} & [0]_{4 \times 3} & [0]_{4 \times 4} & [0]_{4 \times 3} \\ Q_{(4,1)} & Q_{(4,2)} & [0]_{3 \times 4} & Q_{(4,4)} \end{bmatrix} \quad (5.60)$$

Now Q_{RIC} becomes,

$$Q_{RIC} = \begin{bmatrix} T_{RIC}^T Q_{(1,1)} T_{RIC} & T_{RIC}^T Q_{(1,2)} T_{RIC} & [0]_{3 \times 4} & T_{RIC}^T Q_{(1,4)} \\ T_{RIC}^T Q_{(2,1)} T_{RIC} & T_{RIC}^T Q_{(2,2)} T_{RIC} & [0]_{3 \times 4} & T_{RIC}^T Q_{(2,4)} \\ [0]_{4 \times 3} & [0]_{4 \times 3} & Q_{other} & [0]_{4 \times 3} \\ Q_{(4,1)} T_{RIC} & Q_{(4,2)} T_{RIC} & [0]_{3 \times 4} & Q_{(4,4)} \end{bmatrix} \quad (5.61)$$

The upper left term is shown as an example. The other terms are formulated in like fashion.

$$\Phi_{\omega R_{RIC}} \Phi_{\omega R_{RIC}}^T = \left[\Delta t \tau_X + \tau_X^2 (e^{-\Delta t / \tau_X} - 1) \right] \begin{bmatrix} 1 & 0 & 0 \\ 0 & 1 & 0 \\ 0 & 0 & 1 \end{bmatrix} \quad (5.62)$$

In the (1,1) term of $\Phi_{\omega R_{RIC}} \Phi_{\omega R_{RIC}}^T$ set $X \equiv R$, in the (2,2) term $X \equiv I$ and in the (3,3)

term $X \equiv C$. Now,

$$\begin{aligned} Q_{(1,1)_X} &= \int_{t_0}^t \left[\Delta t \tau_X + \tau_X^2 (e^{-\Delta t / \tau_X} - 1) \right] \left[\Delta t \tau_X + \tau_X^2 (e^{-\Delta t / \tau_X} - 1) \right] dT = \\ &= \int_{t_0}^t \left[\tau_X^4 (e^{-2(t-T)/\tau_X} - 2e^{-(t-T)/\tau_X} + 1) + \right. \\ &\quad \left. 2(t-T) \tau_X^3 (e^{-(t-T)/\tau_X} - 1) + (t^2 - 2tT + T^2) \tau_X^2 \right] dT = \\ &= \left(\frac{1}{2} \tau_X^5 (1 - e^{-2\Delta t / \tau_X}) + \tau_X^4 \Delta t (1 - e^{-\Delta t / \tau_X}) - \tau_X^3 \Delta t^2 + \frac{1}{3} \tau_X^2 \Delta t^3 \right) \end{aligned} \quad (5.63)$$

Again,

$$Q_{(1,1)} = \begin{bmatrix} Q_{(1,1)_R} & 0 & 0 \\ 0 & Q_{(1,1)_I} & 0 \\ 0 & 0 & Q_{(1,1)_C} \end{bmatrix}$$

Therefore, the Q matrix can be defined by the following.

$$\begin{aligned} Q_{(1,1)_R} &= \sigma_R^2 \left(\frac{1}{2} \tau_R^5 (1 - e^{-2\Delta t/\tau_R}) + \tau_R^4 \Delta t (1 - e^{-\Delta t/\tau_R}) - \tau_R^3 \Delta t^2 + \frac{1}{3} \tau_R^2 \Delta t^3 \right) \\ Q_{(1,1)_I} &= \sigma_I^2 \left(\frac{1}{2} \tau_I^5 (1 - e^{-2\Delta t/\tau_I}) + \tau_I^4 \Delta t (1 - e^{-\Delta t/\tau_I}) - \tau_I^3 \Delta t^2 + \frac{1}{3} \tau_I^2 \Delta t^3 \right) \\ Q_{(1,1)_C} &= \sigma_C^2 \left(\frac{1}{2} \tau_C^5 (1 - e^{-2\Delta t/\tau_C}) + \tau_C^4 \Delta t (1 - e^{-\Delta t/\tau_C}) - \tau_C^3 \Delta t^2 + \frac{1}{3} \tau_C^2 \Delta t^3 \right) \end{aligned} \quad (5.64)$$

$$Q_{(1,2)_R} = \sigma_R^2 \left(\tau_R^4 \left(\frac{1}{2} - e^{-\Delta t/\tau_R} + \frac{1}{2} e^{-2\Delta t/\tau_R} \right) - \tau_R^3 \Delta t (1 - e^{-\Delta t/\tau_R}) + \frac{1}{2} \tau_R^2 \Delta t^2 \right)$$

$$Q_{(1,2)_R} = Q_{(2,1)_R}$$

$$Q_{(1,2)_I} = \sigma_I^2 \left(\tau_I^4 \left(\frac{1}{2} - e^{-\Delta t/\tau_I} + \frac{1}{2} e^{-2\Delta t/\tau_I} \right) - \tau_I^3 \Delta t (1 - e^{-\Delta t/\tau_I}) + \frac{1}{2} \tau_I^2 \Delta t^2 \right)$$

$$Q_{(1,2)_I} = Q_{(2,1)_I}$$

$$Q_{(1,2)_C} = \sigma_C^2 \left(\tau_C^4 \left(\frac{1}{2} - e^{-\Delta t/\tau_C} + \frac{1}{2} e^{-2\Delta t/\tau_C} \right) - \tau_C^3 \Delta t (1 - e^{-\Delta t/\tau_C}) + \frac{1}{2} \tau_C^2 \Delta t^2 \right) \quad (5.65)$$

$$Q_{(1,2)_C} = Q_{(2,1)_C}$$

$$Q_{(1,4)_R} = Q_{(4,1)_R} = \sigma_R^2 \left(\frac{1}{2} \tau_R^3 (1 - e^{-2\Delta t/\tau_R}) - \tau_R^2 \Delta t e^{-\Delta t/\tau_R} \right)$$

$$\begin{aligned}
Q_{(1,4)_I} &= Q_{(4,1)_I} = \sigma_I^2 \left(\frac{1}{2} \tau_I^3 (1 - e^{-2\Delta t/\tau_I}) - \tau_I^2 \Delta t e^{-\Delta t/\tau_I} \right) \\
Q_{(1,4)_C} &= Q_{(4,1)_C} = \sigma_C^2 \left(\frac{1}{2} \tau_C^3 (1 - e^{-2\Delta t/\tau_C}) - \tau_C^2 \Delta t e^{-\Delta t/\tau_C} \right)
\end{aligned} \tag{5.66}$$

$$\begin{aligned}
Q_{(2,2)_R} &= \sigma_R^2 \left(\tau_R^3 \left(-\frac{3}{2} + 2e^{-\Delta t/\tau_R} - \frac{1}{2} e^{-2\Delta t/\tau_R} \right) + \tau_R^2 \Delta t \right) \\
Q_{(2,2)_I} &= \sigma_I^2 \left(\tau_I^3 \left(-\frac{3}{2} + 2e^{-\Delta t/\tau_I} - \frac{1}{2} e^{-2\Delta t/\tau_I} \right) + \tau_I^2 \Delta t \right) \\
Q_{(2,2)_C} &= \sigma_C^2 \left(\tau_C^3 \left(-\frac{3}{2} + 2e^{-\Delta t/\tau_C} - \frac{1}{2} e^{-2\Delta t/\tau_C} \right) + \tau_C^2 \Delta t \right)
\end{aligned} \tag{5.67}$$

$$\begin{aligned}
Q_{(2,4)_R} &= Q_{(4,2)_R} = \sigma_R^2 \tau_R^2 \left(\frac{1}{2} (1 + e^{-2\Delta t/\tau_R}) - e^{-\Delta t/\tau_R} \right) \\
Q_{(2,4)_I} &= Q_{(4,2)_I} = \sigma_I^2 \tau_I^2 \left(\frac{1}{2} (1 + e^{-2\Delta t/\tau_I}) - e^{-\Delta t/\tau_I} \right) \\
Q_{(2,4)_C} &= Q_{(4,2)_C} = \sigma_C^2 \tau_C^2 \left(\frac{1}{2} (1 + e^{-2\Delta t/\tau_C}) - e^{-\Delta t/\tau_C} \right)
\end{aligned} \tag{5.68}$$

$$\begin{aligned}
Q_{(4,4)_R} &= \frac{\sigma_R^2}{2} \tau_R (1 - e^{-2\Delta t/\tau_R}) \\
Q_{(4,4)_I} &= \frac{\sigma_I^2}{2} \tau_I (1 - e^{-2\Delta t/\tau_I}) \\
Q_{(4,4)_C} &= \frac{\sigma_C^2}{2} \tau_C (1 - e^{-2\Delta t/\tau_C})
\end{aligned} \tag{5.69}$$

And again,

$$Q_{\text{other}} = \begin{bmatrix} \sigma_{\text{drag}}^2 \Delta t & 0 & 0 & 0 \\ 0 & \sigma_{\text{rad}}^2 \Delta t & 0 & 0 \\ 0 & 0 & \frac{\sigma_b^2 \Delta t^3}{3} + \sigma_b^2 \Delta t & \frac{\sigma_b^2 \Delta t^2}{2} \\ 0 & 0 & \frac{\sigma_b^2 \Delta t^2}{2} & \sigma_b^2 \Delta t \end{bmatrix} \quad (5.70)$$

Finally,

$$Q_{\text{RIC}} = \begin{bmatrix} T_{\text{RIC}}^T Q_{(1,1)} T_{\text{RIC}} & T_{\text{RIC}}^T Q_{(1,2)} T_{\text{RIC}} & [0]_{3 \times 4} & T_{\text{RIC}}^T Q_{(1,4)} \\ T_{\text{RIC}}^T Q_{(2,1)} T_{\text{RIC}} & T_{\text{RIC}}^T Q_{(2,2)} T_{\text{RIC}} & [0]_{3 \times 4} & T_{\text{RIC}}^T Q_{(2,4)} \\ [0]_{4 \times 3} & [0]_{4 \times 3} & Q_{\text{other}} & [0]_{4 \times 3} \\ Q_{(4,1)} T_{\text{RIC}} & Q_{(4,2)} T_{\text{RIC}} & [0]_{3 \times 4} & Q_{(4,4)} \end{bmatrix} \quad (5.71)$$

5.4 Single Satellite Range and Range Rate Simulation (Simulation 1)

Two simulations are developed in Matlab to compare the results of XYZ DMC and RIC DMC. Both simulations consist of a user satellite in LEO (modeled after the QuikScat orbit). Satellite Toolkit (STK) is used to generate a “truth” trajectory using a 70x70 gravity model, atmospheric drag, solar pressure and third-body effects from the Sun and Moon. The trajectory is propagated over 20,000 seconds. Next, tracking satellites in geostationary orbits, with equally spaced longitudes, are used to generate simulated observations. The first simulation uses three “TrakSats”, each separated by 120° of longitude. Range and range rate measurements are taken at 20-second intervals with only one TrakSat measurement at each observation epoch. Then, zero mean, standard deviation 1 m Gaussian noise is added to the range measurements and zero mean,

standard deviation 0.1 m/s Gaussian noise is added to the range rate measurements.

An Extended Kalman Filter (EKF) is then implemented to process the range and range rate observations. The dynamic model used by the EKF consists of two-body and J2 gravity terms and an exponential drag model. The state transition matrix is integrated along with the position and velocity and includes two-body, J2 and exponential drag terms.

5.4.1 Simulation 1 No Process Noise

The initial EKF implementation did not include DMC nor did it include any form of process noise. Figure 5.2 shows the filter's estimated trajectory compared to the STK truth data. The standard deviation in the error plot is the square root of the estimated state error position variance term. The covariance approaches zero since no process noise is used.

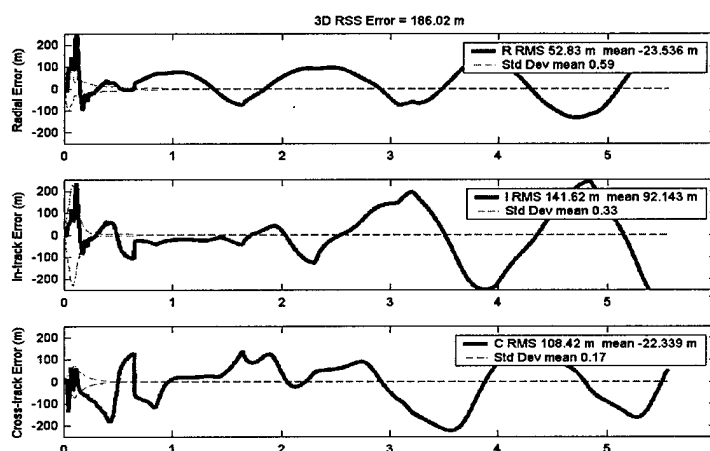


Figure 5.2 – Simulation 1 No Process Noise Results

5.4.2 Simulation 1 GEODE Process Noise

Next the process noise formulation used in GEODE is added to the simulation filter. τ and the σ s are tuned to minimize the 3D RSS error of the filtered solution when compared to the truth data. The error and standard deviation statistics are shown in Figure 5.3. Figure 5.3 shows that by adding process noise, precision and accuracy improved and the variances appear more reasonable.

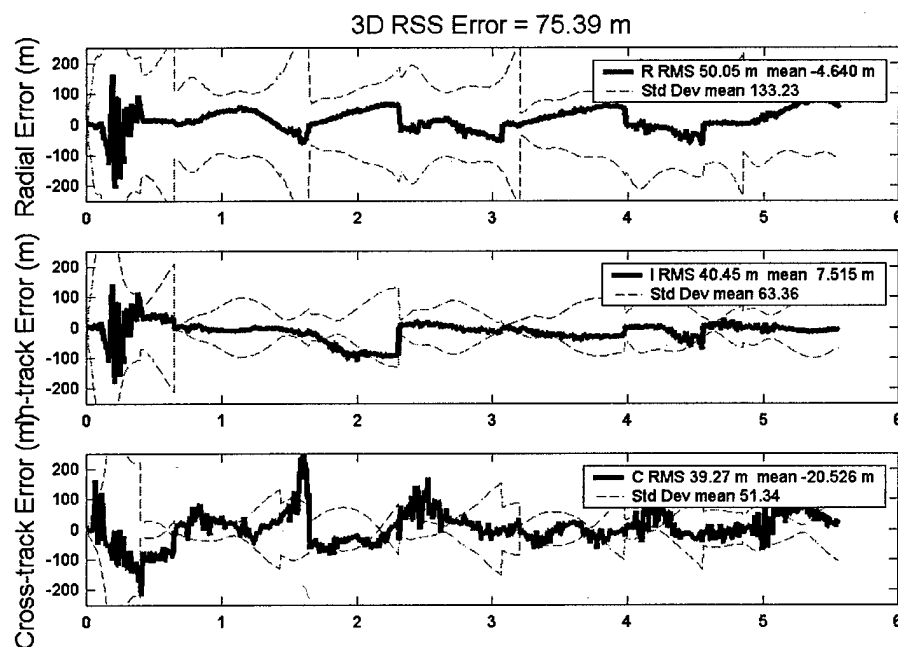


Figure 5.3 – Simulation 1 GEODE Process Noise Results

5.4.3 Simulation 1 XYZ DMC

Next the EKF is implemented with XYZ DMC and τ , σ_u , σ_μ , σ_{J2} and σ_{CD} are, again, tuned to produce the lowest 3D RSS error compared to the STK truth trajectory. Adding the estimation of the compensative accelerations and the DMC process noise significantly improved the filter's precision and accuracy. Figure 5.4 shows the error and standard deviation statistics for the XYZ DMC case.

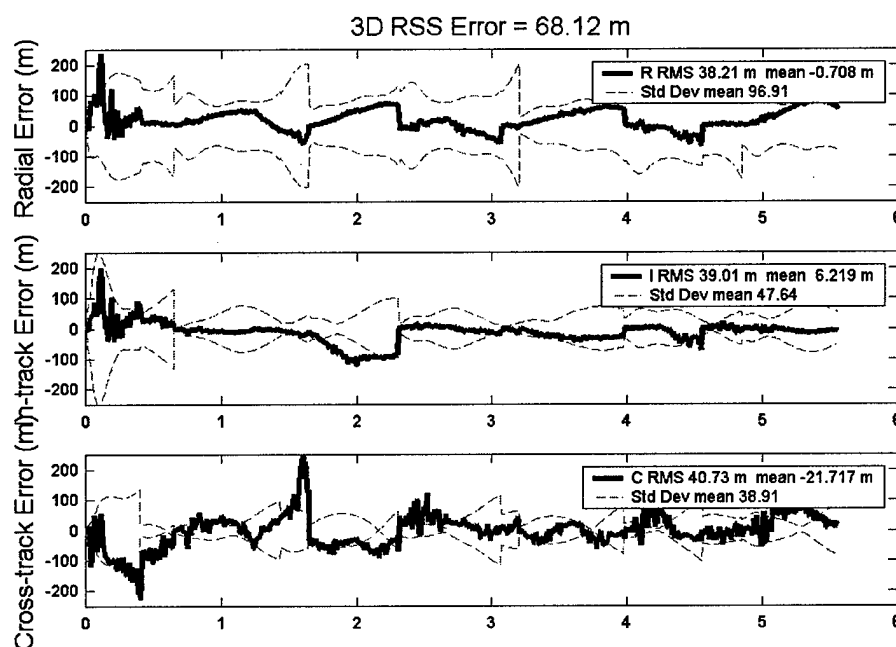


Figure 5.4 – Track Simulation 1 XYZ DMC Results

5.4.4 Simulation 1 RIC DMC

The final step in simulation 1 is to convert the compensative accelerations, state transition matrix and process noise covariance matrix to RIC coordinates and tune the τ s and σ s ($\tau_R, \tau_I, \tau_C, \sigma_R, \sigma_I, \sigma_C, \sigma_\mu, \sigma_{J2}$ and σ_{CD}). Results are shown in

Figure 5.5.

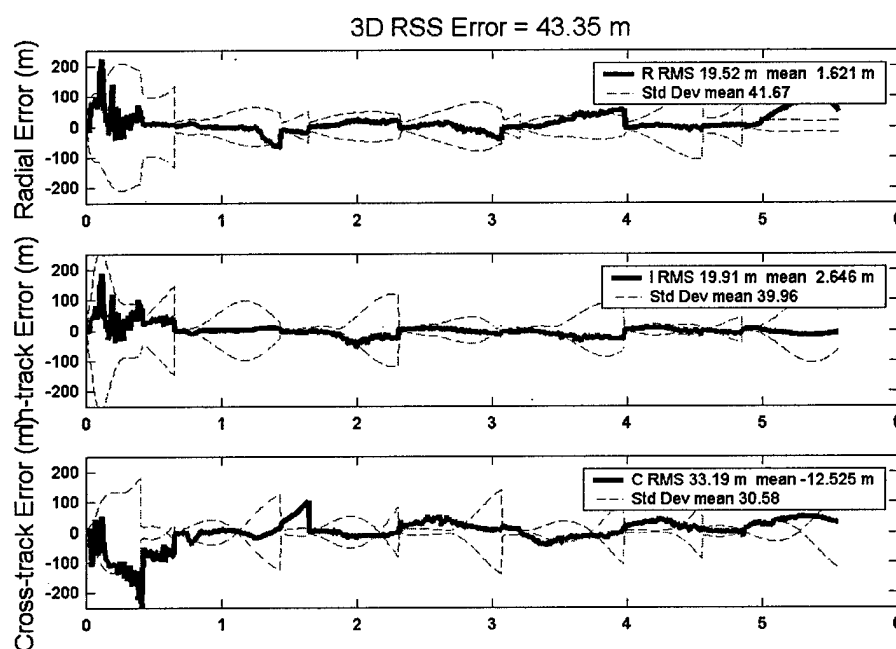


Figure 5.5 – Simulation 1 RIC DMC Results

Table 5.1 shows a summary of the results of simulation 1. Adding process noise to the filter's covariance matrix significantly improves its accuracy and precision. Additional accuracy and precision are gained by estimating

compensative accelerations and by applying RIC DMC. RIC DMC improved the filter's error RSS by 36.4% compared to XYZ DMC.

Table 5.1 – Summary of Results with 3 TrackSats and 1 m Noise on Range

Simulation 1	Error Mean (m)			Error RMS (m)			
	R	I	C	R	I	C	3D
No Process Noise	-23.5	92.1	-22.3	57.8	141.6	108.4	186.0
GEODE Process Noise	-4.6	7.5	-20.5	50.0	40.5	39.3	75.4
XYZ DMC	-0.7	6.2	-21.7	38.2	39.0	40.7	68.1
RIC DMC	1.6	2.7	-12.5	19.5	19.9	33.2	43.3

5.5 Multi-satellite Range Simulation (Simulation 2)

The second simulation uses the same STK trajectory as truth. However, in this simulation four TrakSats are used, each spaced 90° apart in longitude. Range measurements are then calculated artificially from all four satellites at 20-second intervals. In simulation 2 there are four range observations at each observation epoch and no range rate observations. Obviously, measuring range from all four satellites at once is not possible due to interference by the Earth. The additional satellite is added and measurements from all satellites at once are used to improve the simulation's observation geometry. The improved geometry allows a significant improvement in accuracy and precision. The 3D RSS error without DMC is 158 m. When RIC DMC is applied the 3D RSS error is 3.1 m. As shown in Table 5.1, the best result using RIC DMC in simulation 1 is 43.3 m, 3D. Since the objective of this simulation is to determine if transforming DMC to the RIC orientation improves solution accuracy, mean of zero, standard deviation 50 m Gaussian noise is added to the range measurements instead of 1 m noise. The

filter result without process noise is a 3D RSS error of 169 m but with GEODE's process noise formulation the best result is 50.3 m 3D. Figure 5.6 through Figure 5.9 show error plots for the various methods and Table 5.2 shows a summary of the error statistics for the various methods.

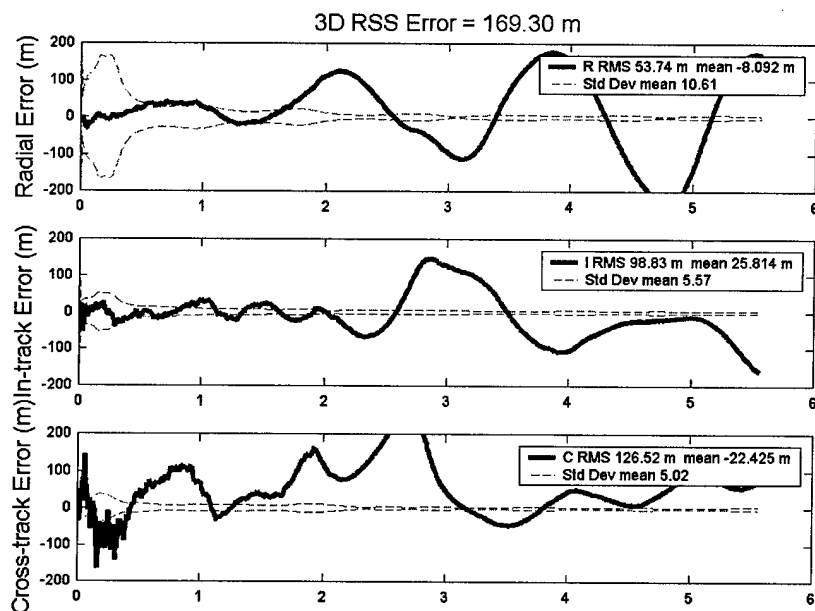


Figure 5.6 – Simulation 2 No Process Noise Results

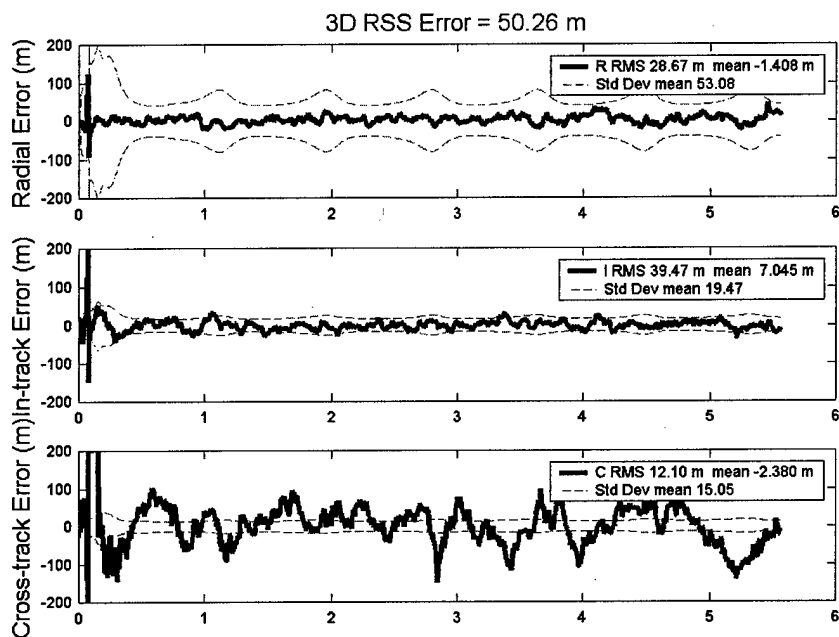


Figure 5.7 - Simulation 2 GEODE Process Noise Results

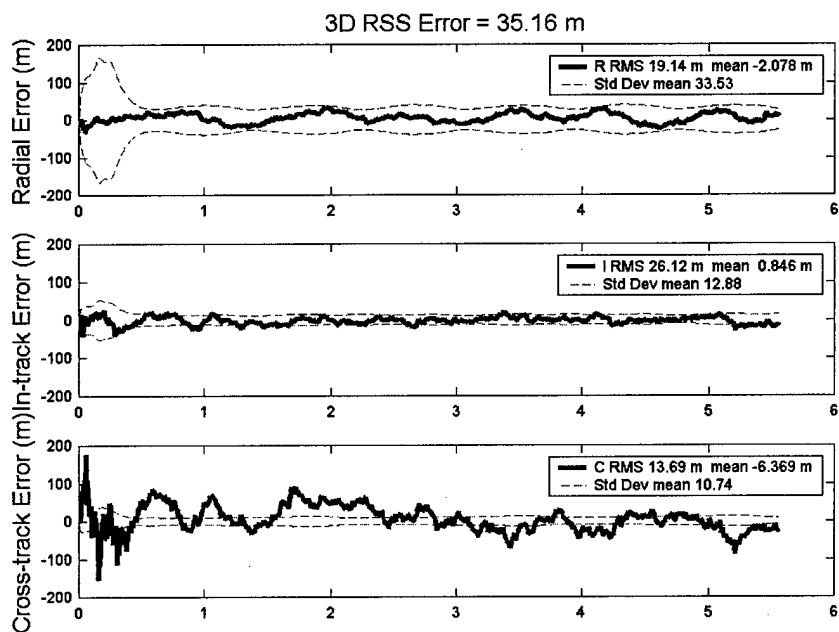


Figure 5.8 - Simulation 2 XYZ DMC Results

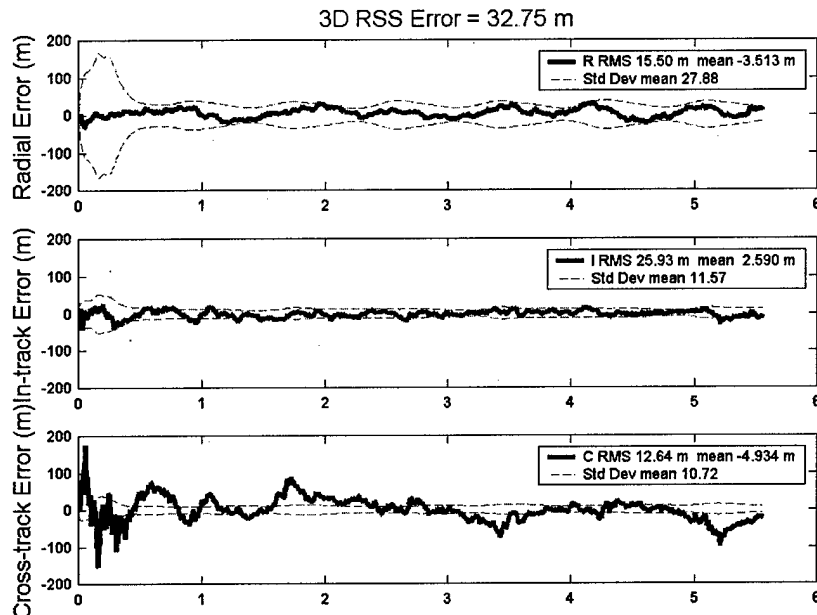


Figure 5.9 – Simulation 2 RIC DMC Results

Table 5.2 - Summary of Results with 4 TrakSats and 50 m Noise on Range

Simulation 2	Error Mean (m)			Error RMS (m)			
	R	I	C	R	I	C	3D
No Process Noise	-8.1	25.8	-22.4	53.7	98.8	126.5	169.3
GEODE Process Noise	-1.4	7.04	-2.9	28.7	39.5	12.1	50.3
XYZ DMC	-2.1	0.9	-6.4	19.1	26.1	13.7	35.2
RIC DMC	-3.5	2.6	-4.9	15.5	25.9	12.6	32.8

5.6 Simulation Conclusions

In both simulations the RIC implementation of DMC outperforms the XYZ version. The poor viewing geometry in the first simulation contributes to allowing RIC DMC to best XYZ DMC by over 36%. The second simulation shows that with better geometry and more observations (even though 50 m noise is added) RIC DMC does not outperform XYZ DMC as dramatically. The

improvement in the second simulation is slightly under 7%. The several meter 3D improvement is worth the difficulty of tuning 6 parameters rather than 2. The greater flexibility offered by RIC DMC in adjusting the process noise allowed a 19% improvement in the radial direction. Next results from DMC implementation in GEODE are presented.

5.7 XYZ DMC in GEODE

The XYZ implementation of DMC in GEODE is straightforward. The three compensative accelerations are added to the state and the deterministic portion of equation (5.6) (also shown in equation (5.23)) augments GEODE's time propagation of the state. The state transition matrix is augmented with three rows and three columns per equation (5.24). The process noise covariance formulation in equations (5.36) through (5.43) is implemented in the same manner as GEODE's process noise formulation. Finally, $\tau, \sigma_u, \sigma_b, \sigma_{\dot{b}}, \sigma_{C_D},$ and σ_{C_R} input variables are added to the uplink command file along with a switch to use DMC or GEODE's original process noise implementation.

5.7.1 XYZ DMC Tuning

Significant effort is involved in tuning the process noise τ and σ s in the application of DMC. The tuning process consists of incrementally changing each parameter and recording the error between the filter's estimate and the "truth" data. An example of a series of tuning runs for the 4 Feb 1997 GPS/MET data is

presented in Table 5.3. In Table 5.3 the bold items are the values being tuned.

The parameters that achieved optimal results are presented in Table 5.4. The results achieved with XYZ DMC are a significant improvement over GEODE's original process noise formulation.

Table 5.3 – GPS/MET XYZ DMC Parameter Tuning

τ	σ_u	σ_b	$\sigma_{\dot{b}}$	σ_{C_D}	σ_{C_R}	3D RSS
0.028	0.0001	11.0	0.001	0.0001	0.0001	8.33
0.03	0.0001	11.0	0.001	0.0001	0.0001	8.32
0.034	0.0001	11.0	0.001	0.0001	0.0001	8.33
0.03	0.00005	11.0	0.001	0.0001	0.0001	8.49
0.03	0.00013	11.0	0.001	0.0001	0.0001	8.35
0.03	0.0001	10.0	0.001	0.0001	0.0001	8.34
0.03	0.0001	12.0	0.001	0.0001	0.0001	8.34
0.03	0.0001	11.0	0.0001	0.0001	0.0001	8.32
0.03	0.0001	11.0	0.01	0.0001	0.0001	8.36
0.03	0.0001	11.0	0.001	0.00001	0.0001	8.32
0.03	0.0001	11.0	0.001	0.0002	0.0001	8.34
0.03	0.0001	11.0	0.001	0.0001	0.00001	8.32
0.03	0.0001	11.0	0.001	0.0001	0.0002	8.34

Table 5.4 – GPS/MET XYZ DMC “Optimal” Parameters

Parameter	Tuned Value
τ	0.03
σ_u	0.0001
σ_b	11.0
$\sigma_{\dot{b}}$	0.001
σ_{C_D}	0.0001
σ_{C_R}	0.0001

Optimal tuning results for GPS/MET data when JPL high rate GPS clock estimates are applied to attempt to remove SA affects are shown in Table 5.5.

Table 5.5 – GPS/MET With High Rate GPS Clocks XYZ DMC “Optimal”
Parameters

Parameter	Tuned Value
τ	0.03
σ_u	0.0001
σ_b	5.9
$\sigma_{\dot{b}}$	0.09
σ_{C_D}	0.0001
σ_{C_R}	0.0001

5.7.2 XYZ DMC GEODE Accuracy/Precision Results

XYZ DMC implementation significantly improves GEODE’s position estimates. Table 5.6 shows a comparison of the GPS/MET (no high rate clocks) results achieved with GEODE’s original process noise formulation and results with XYZ DMC in GEODE. Without DRVID XYZ DMC improves the error RSS by over 23.0% while DRVID XYZ DMC improves accuracy by over 28.2%. Both of the previous comparisons are with the original implementation of GEODE.

Table 5.6 - GEODE Results With and Without XYZ DMC

4 Feb 1997 GPS/MET	Mean of Error (m)			RMS Error of Filter Compared to Truth (m)			
Scheme	R	I	C	R	I	C	3D
Original Single	0.55	-0.99	-0.10	2.74	10.24	2.15	10.81
Original DRVID	0.24	-1.14	-0.11	2.63	9.72	2.23	10.32
XYZ DMC Single	-0.18	3.08	-0.14	1.74	7.77	2.41	8.32
XYZ DMC DRVID	-0.30	1.94	-0.14	1.93	7.07	2.56	7.76

To gauge the accuracy improvement gained using XYZ DMC with SA off, results are presented in Table 5.7 and Table 5.8. Table 5.7 shows DMC results

when JPL high rate GPS clock estimates are applied to GPS/MET data. Table 5.8 shows DMC results for the SA free TOPEX data. DRVID XYZ DMC provided a 19.6% improvement over the original implementation in GEODE while XYZ DMC without DRVID resulted in only a 16.7% improvement on the GPS/MET data. Also, DMC improves the SA free TOPEX 3D position RSS by 10.8% when precise GPS ephemerides are not used and 11.1% when precise GPS ephemerides are used.

Table 5.7 - GEODE Results With and Without XYZ DMC Using High Rate Clock Estimates to Correct for SA

4 Feb 1997 GPS/MET	Mean of Error (m)			RMS Error of Filter Compared to Truth (m)			
Scheme	R	I	C	R	I	C	3D
Original None	0.28	-3.59	-0.04	2.22	7.23	0.77	7.60
Original DRVID	-0.03	-3.54	-0.04	1.97	6.95	0.90	7.28
XYZ DMC None	-0.21	-0.52	-0.05	2.01	5.94	0.89	6.33
XYZ DMC DRVID	-0.31	-1.19	-0.06	1.95	5.70	1.03	6.11

Table 5.8 - SA Free TOPEX Results With and Without XYZ DMC

5 May 2000 TOPEX	Mean of Error (m)			RMS Error of Filter Compared to Truth (m)			
Scheme	R	I	C	R	I	C	3D
Original None	0.21	-0.04	0.01	0.35	1.06	0.44	1.20
XYZ DMC None	0.19	-0.03	0.02	0.33	0.91	0.45	1.07
Original Single with Precise GPS Ephemeris	0.22	-0.16	0.00	0.34	0.97	0.31	1.08
XYZ DMC Single with Precise GPS Ephemeris	0.20	-0.18	0.01	0.33	0.84	0.33	0.96

5.7.3 XYZ DMC GEODE Computational Burden Results

The computational burden of XYZ DMC is roughly equivalent to that of the original process noise implementation in GEODE.

5.8 RIC DMC in GEODE

The implementation of RIC DMC in GEODE involves the same implementation as XYZ DMC with the addition of the RIC variables to the uplink command file and appropriate application of the XYZ to RIC transformation matrices as in equations (5.46), (5.47), (5.54), and (5.71). It can be shown that by setting $\tau_R = \tau_I = \tau_C$ and $\sigma_R = \sigma_I = \sigma_C$ RIC DMC is the equivalent of XYZ DMC. The first line of data in Table 5.9 shows the XYZ DMC case applied to RIC DMC. Table 5.9 also shows the results achieved with GEODE through tuning of the RIC parameters for the case where single frequency GPS measurements are used and DRVID is not applied. Table 5.10 shows the optimal RIC DMC parameters found through tuning.

Table 5.9 – GPS/MET RIC DMC Parameter Tuning

τ_R	τ_I	τ_C	σ_R	σ_I	σ_C	3D RSS
0.03	0.03	0.03	0.0001	0.0001	0.0001	8.32
0.001	0.03	0.03	0.0001	0.0001	0.0001	8.32
0.1	0.03	0.03	0.0001	0.0001	0.0001	8.35
0.03	0.028	0.03	0.0001	0.0001	0.0001	8.33
0.03	0.032	0.03	0.0001	0.0001	0.0001	8.33
0.03	0.03	0.3	0.0001	0.0001	0.0001	8.10
0.03	0.03	0.4	0.0001	0.0001	0.0001	8.08
0.03	0.03	0.5	0.0001	0.0001	0.0001	8.08
0.03	0.03	0.6	0.0001	0.0001	0.0001	8.09
0.03	0.03	0.4	0.00005	0.0001	0.0001	8.07
0.03	0.03	0.4	0.0002	0.0001	0.0001	8.09
0.03	0.03	0.4	0.00005	0.00005	0.0001	8.07
0.03	0.03	0.4	0.00005	0.0002	0.0001	8.09
0.03	0.03	0.4	0.00005	0.0001	0.00005	8.07
0.03	0.03	0.4	0.00005	0.0001	0.0002	8.09

Table 5.10 – GPS/MET RIC DMC “Optimal” Parameters

Parameter	Tuned Value
τ_R	0.03
τ_I	0.03
τ_C	0.4
σ_R	0.00005
σ_I	0.0001
σ_C	0.0001
σ_b	11.0
$\sigma_{\dot{b}}$	0.001
σ_{C_D}	0.0001
σ_{C_R}	0.0001

5.8.1 RIC DMC GEODE Results

Table 5.11 shows a comparison of the RIC DMC results using the optimal values shown in Table 5.10 compared to the original process noise implementation in GEODE. The position error improved from 8.32 m 3D RSS

for XYZ DMC to 8.07 m 3D RSS for RIC DMC or 3% (case without DRVID).

The DRVID improvement is only 2.6%.

The accuracy improvements realized by RIC DMC in GEODE are much smaller than those gained by RIC DMC in the simulations previously described. The small improvement in accuracy is probably due to the exceptional observing geometry offered by GPS. As shown in the simulations, when the observing geometry improves, the utility of RIC DMC decreases. Although RIC DMC implementation only improves accuracy marginally for the processing of GPS pseudoranges, it may provide additional accuracy improvements when applied to different observation types, as in the case where GPS point solutions are used as measurements for a filter. Additionally, RIC DMC increased GEODE's computational burden by approximately 1%.

Table 5.11 - GEODE Results With and Without RIC DMC

4 Feb 1997 GPS/MET	Mean of Error (m)			RMS Error of Filter Compared to Truth (m)			
Scheme	R	I	C	R	I	C	3D
Original Single	0.55	-0.99	-0.10	2.74	10.24	2.15	10.81
Original DRVID	0.24	-1.14	-0.11	2.63	9.72	2.23	10.32
XYZ DMC Single	-0.18	3.08	-0.14	1.74	7.77	2.41	8.32
XYZ DMC DRVID	-0.30	1.94	-0.14	1.93	7.07	2.56	7.76
RIC DMC Single	-0.17	2.89	-0.17	1.70	7.55	2.30	8.07
RIC DMC DRVID	-0.29	1.75	-0.17	1.94	6.92	2.26	7.53

5.9 Summary

In this chapter Dynamic Model Compensation is first developed for a one-dimensional estimation problem. DMC is then extended to a satellite orbit

determination problem and the XYZ and RIC versions are developed. XYZ and RIC DMC are then employed in two simulations. In the first simulation, RIC DMC lowers the 3D error RSS by 36.4% compared to XYZ DMC. Both XYZ and RIC DMC improved accuracy considerably over GEODE's process noise implementation. In the second simulation, observing geometry is improved causing the RIC DMC accuracy to only improve 7% over XYZ DMC.

XYZ and RIC DMC are then implemented in GEODE. XYZ DMC improves GEODE's error RSS by 23.0% when applied to the processing GPS/MET data, 16.7% for GPS/MET data with high rate GPS clocks and 10.8% on SA free TOPEX data. XYZ DMC not only improves the position error RSS, it does not increase computational burden.

While RIC DMC significantly improves filter accuracy/precision in the simulations it only marginally improves GEODE's performance. The modest 3% improvement without DRVID and 2.6% improvement with DRVID (compared to XYZ DMC) may not be worth the overhead involved in tuning the additional parameters. Finally, RIC DMC increases GEODE's computational burden by roughly 1% compared to GEODE's original process noise formulation.

CHAPTER 6

Genetic Model Compensation (GMC)

Genetic Model Compensation (GMC) [9, 64] is an application of a Genetic Algorithm (GA) to the optimization of the correlation time of the exponential decay (τ) and standard deviation (σ_u , σ_b , $\sigma_{\dot{b}}$) of the forcing noise from DMC. As seen in Chapter 5 of this dissertation, the values chosen for τ and the σ s have a significant effect on filter performance. Normally, the σ s are considered constant and tuned through trial and error testing where the true states are available (as shown in Chapter 5). Since τ is included in the deterministic portion of the DMC augmentation of the state, it can be estimated as part of the state. Unfortunately, there are problems associated with estimating τ . The satellite OD EKF relies on linearization of the state trajectory and observation/state relationship. The state members (position, velocity, clock bias, clock bias drift rate, coefficient of drag and coefficient of radiation pressure) are known, a priori, with sufficient accuracy to guarantee linearity. However, there is no way to generate an a priori estimate of τ with accuracy to support the assumption of linearity. Without accurate a priori knowledge of τ , the filter may not be able to adjust τ to its optimum value and may even diverge [65]. If τ and the σ s are tuned, there is no guarantee their optimum value will be chosen or the

optimum tuned values will be optimum during actual implementation (flight on board a satellite, in this case). GMC was developed and implemented by Cruickshank to replace ad hoc tuning and estimation with the genetic estimation of σ_u , σ_b , $\sigma_{\dot{b}}$ and τ [9, 64, 65]. GMC adapts σ_u , σ_b , $\sigma_{\dot{b}}$ and τ as part of the OD process. Cruickshank suggests that GMC is perfectly suited for the autonomous satellite OD environment since no a priori knowledge of σ_u , σ_b , $\sigma_{\dot{b}}$ and τ is needed [9].

In this chapter the Genetic Algorithm (GA) is briefly described, the algorithm for the application of GMC in GEODE is presented and accuracy/precision and computational burden results of GMC are shown.

6.1 The Genetic Algorithm (GA)

A summary of the benefits of the GA and a brief description are presented here, more detailed information can be found in [66]. The GA is a model of machine learning derived from the theoretical mechanisms of evolution in nature. In the GA chromosomes represent a population of individuals. The chromosomes are a set of binary numbers representing values to be optimized. The individuals go through a process of simulated evolution to optimize their values based on a fitness function. There are many optimization techniques available however, the GA has several qualities that separate it from other search techniques. The GA:

- Operates on coding of the parameter set rather than on the parameters themselves

- Searches for the optimum from a population of points simultaneously rather than from a single point
- Uses payoff information from the values generated by a fitness function rather than the gradient or other auxiliary information to direct the search
- Uses probabilistic transition rules rather than deterministic transition rules [66]

The GA seeks a global maximum (or minimum) by optimally using exploration to investigate unknown areas of the search space and exploitation to make use of knowledge found at previously visited points [67]. The three operators reproduction, crossover and mutation act on the population allowing both exploration and exploitation of the search space.

6.1.1 Reproduction

In reproduction, parents are selected randomly from the population in a way that favors the most sought after individuals. The most sought after individuals may be selected more than once, while least sought after individuals may not be selected. The parents (chosen for their fitness for reproduction based on a fitness function) are then randomly arranged in pairs for mating.

6.1.2 Crossover

Crossover is the random exchange of chromosome strings between mating pairs. Crossover is not always performed on the entire population but on random pairs of individuals selected for mating. The probability of selection for crossover is between 50 and 100%. Random portions of the chromosomes from one

individual are exchanged for those from another. In this way the offspring may receive a selection of genes from each parent.

6.1.3 Mutation

Mutation is randomly applied to offspring after crossover. Here individual genes are randomly altered with very small probability (0.1 – 0.001). The traditional view is that crossover is more important for rapidly exploring the search space while mutation provides a small amount of random search, ensuring that no point in the search space has zero probability of examination [67].

6.1.4 GA Application

The GA is applied by, first, randomly selecting a population of individuals. These individuals are tested by a fitness function to determine which are most suitable for reproduction. Then, a probability of reproduction is calculated for individuals based on their suitability. Reproduction is accomplished by randomly selecting individuals based on their reproduction probability. In this way, the best individuals have the highest priority of being selected. Individuals may be selected more than once or not at all. Next, individuals are randomly paired for mating. Then, crossover of genes is performed if randomly decided. Finally, mutation is performed on offspring from crossover, again if randomly decided [64].

6.2 GMC Algorithm

The following GMC algorithm is extracted from Cruickshank [9] and applies to the pseudorange measurement only. The algorithm is modified to include σ_b .

1. Generate an initial gene pool (as base 10 numbers) of size n for σ_u , σ_b , $\sigma_{\dot{b}}$ and τ . Nominally, $n=10$. A sample distribution for the gene pool is [1, 50, 100, 500, 1000, 3300, 6600, 10000, 13000, 16383]. Scaling of the gene pool is discussed in section 6.3.
2. Encode the n base ten numbers (candidate values for σ_u , σ_b , $\sigma_{\dot{b}}$, τ) in each gene pool into n binary strings of length q (nominally, $q=14$).
3. Randomly group the candidate values into quadruplets $[\tau \ \sigma_u \ \sigma_b \ \sigma_{\dot{b}}]$.
4. Compute the propagated genetic position, velocity, and clock increments for each of the n candidate quadruplets $[\tau \ \sigma_u \ \sigma_b \ \sigma_{\dot{b}}]$ using:

$$\delta x_{\text{GMC}} = \int_{t_0}^t \left[\tau(t-T) + \tau^2 \left(e^{-(t-T)/\tau} - 1 \right) u(t) \right] dT \quad (6.1)$$

$$\delta b = \int_{t_0}^t (t-T) u_b(T) dT \quad (6.2)$$

$$\delta \dot{b}_u = \int_{t_0}^t u_b(T) dT \quad (6.3)$$

The stochastic integrals are evaluated by Riemann sums, i.e.:

$$\int_{t_0}^t g(u(T)) dT \cong \sum_{i=0}^m g(u(t_i)) (t_{i+1} - t_i) \quad (6.4)$$

$$\delta x_{\text{GMC}} = \sum_{j=1}^m \left(tks\tau + \tau^2 (eks - 1) \frac{\Delta t}{m} u_{u_j}(t) \sigma_u \right) \quad (6.5)$$

$$\delta b = \sum_{j=1}^m \left(tks \frac{\Delta t}{m} u_{b_j}(t) \sigma_b + \frac{\Delta t}{m} u_{b_j}(i) \sigma_{\dot{b}} \right) \quad (6.6)$$

$$\delta \dot{b} = \sum_{j=1}^m \left(\frac{\Delta t}{m} u_{b_j}(t) \sigma_{b_j} \right) \quad (6.7)$$

$$t_{ks} = \Delta t - \frac{(m-0.5)\Delta t}{m} \quad (6.8)$$

$$e_{ks} = e^{-t_{ks}/\tau} \quad (6.9)$$

where $t_i \leq t_i' \leq t_{i+1}$ and $u(t)$ represents the uncorrelated Gaussian random noise process.

5. Compute the predicted genetic pseudorange by

$$G_{pg} = \rho_g - b_g c + b_G c = \sqrt{(x_G - x_g)^2 - (y_G - y_g)^2 - (z_G - z_g)^2} - b_g c + b_G c \quad (6.10)$$

where

$$\begin{aligned} x_g &= x_u + \delta x_{GMC} \\ y_g &= y_u + \delta y_{GMC} \end{aligned} \quad (6.11)$$

$$z_g = z_u + \delta z_{GMC}$$

$$b_g = b_u + \delta b_{GMC} + \dot{b}_u \Delta t + \delta \dot{b}_{GMC} \Delta t$$

$b_G \equiv$ GPS satellite clock bias

x_u , y_u , and z_u are the best estimates of the user satellite at the current epoch and x_G , y_G , and z_G are the GPS satellite's coordinates.

6. Compute the genetic pseudorange residuals by

$$y_{pg_i} = \rho_i - G_{pg_i} \quad (6.12)$$

where ρ_i is the i^{th} pseudorange measurement.

7. Compute the fitness function value for each candidate quadruplet

$[\tau \quad \sigma_u \quad \sigma_b \quad \sigma_{\dot{b}}]$ by

$$f_i = \frac{a}{\varepsilon_{g_i} R^{-1} \varepsilon_{g_i}}; \quad i = 1, 2, \dots, n \quad (6.13)$$

where

$i \equiv$ the i^{th} genetic parameter quadruplet

$\varepsilon_{gi} \equiv$ the vector of genetic measurement residual for the i^{th} genetic parameter quadruplet

$R^{-1} \equiv$ a diagonal weighting matrix formed from the observed measurement residuals

$a \equiv$ the maximum value of $\varepsilon_{gi} R^{-1} \varepsilon_{gi}$ over all n genetic parameter quadruplets

8. Select the candidate quadruplet $\begin{bmatrix} \tau & \sigma_u & \sigma_b & \sigma_{\dot{b}} \end{bmatrix}_{\text{opt}}$ that yields the highest objective function value:

$$f_{\max} = f(\tau_{\text{opt}}, \sigma_{u_{\text{opt}}}, \sigma_{b_{\text{opt}}}, \sigma_{\dot{b}_{\text{opt}}}) \quad (6.14)$$

9. Update $\begin{bmatrix} \tau & \sigma_u & \sigma_b & \sigma_{\dot{b}} \end{bmatrix}_{\text{opt}}$ for the next formulation of the process noise covariance and state transition matrices.
10. Update the propagation equations for the acceleration, velocity, and position states so that τ_{opt} will be used in the next time update.
11. Compute the merit values (probability of reproduction) for the gene pool quadruplets:

$$v_i = \frac{f_i}{\sum_{j=1}^N f_j} \quad (6.15)$$

12. Compute the gene pool variances. For any particular gene pool, the gene pool variance is defined as:

$$\xi(\theta) = \frac{1}{n} \sum_{i=1}^n (\theta_i - \theta_{\text{opt}})^2 \quad (6.16)$$

where θ represents the gene pool parameter, e.g., σ or τ .

13. Perform the reproduction procedure. The probability of reproduction for the i^{th} gene pool quadruplet is given by v_i . Reproduction of σ_u , σ_b , $\sigma_{\dot{b}}$ and τ are done by quadruplets.
14. Perform the crossover procedure with the new gene pools. The crossover probability is a function of the gene pool variance:

$$\Psi(\theta) = 0.99 - 0.99 \left(\frac{\sqrt{\xi(\theta)}}{\kappa(\theta)} \right)$$

$$p_{\text{cross}}(\theta) = \Psi(\theta) \text{ if } \Psi(\theta) \geq 0.5$$

$$p_{\text{cross}}(\theta) = 0.5 \text{ if } \Psi(\theta) \leq 0.5$$
(6.17)

where $\kappa(\theta)$ is the crossover rate factor. Its value is chosen to be of the same order of magnitude as the anticipated maximum value of $\sqrt{\xi(\theta)}$. The probability floor of 0.5 is arbitrarily chosen. Crossover is performed on the $\sigma_u, \sigma_b, \sigma_{\hat{b}}, \tau$ strings separately, not on the quadruplets.

15. Perform the mutation procedure with the new gene pools. The probability of mutation for any particular bit is an input value (nominally set to 0.01). Mutation is performed on the $\sigma_u, \sigma_b, \sigma_{\hat{b}}, \tau$ strings separately.
16. Return to step 3 with the new $\sigma_u, \sigma_b, \sigma_{\hat{b}}, \tau$ gene pools. The new gene pools become the initial gene pools for the next update at t_{k+1} .

Figure 6.1 shows the entire GMC algorithm with respect to GEODE.

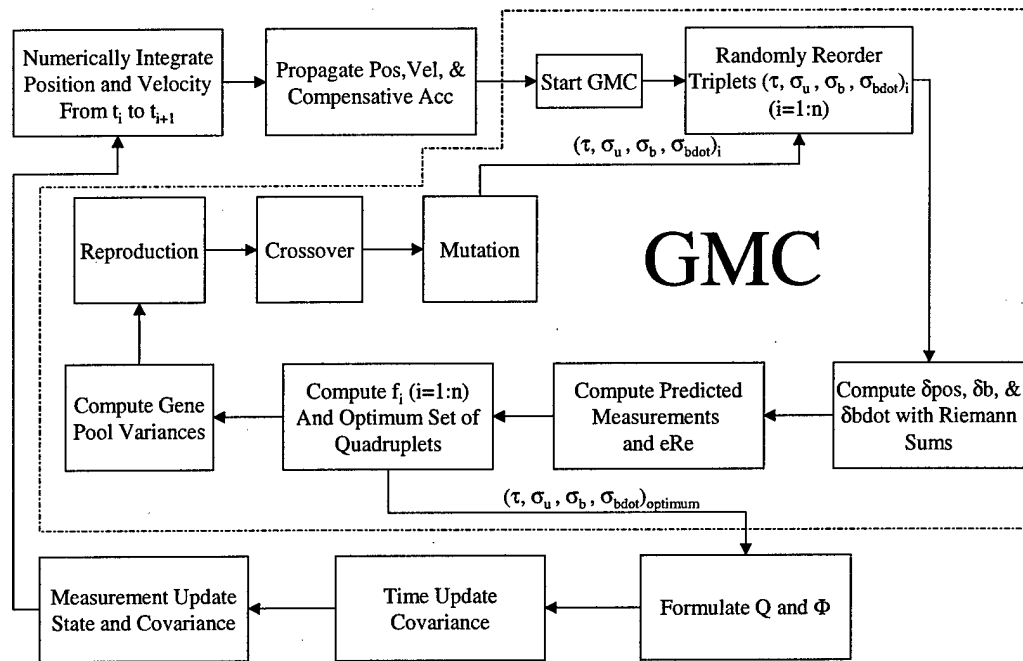


Figure 6.1 – GMC Algorithm

6.3 GMC in GEODE

GMC is implemented in GEODE using XYZ DMC only. The values for σ_{CD} and σ_{CR} are set at 0.0001, just as in XYZ DMC. The binary string length is set at 14 bits giving a range of values for each member of the design space from 0 to 16383 (2^{14}). Each τ and σ is scaled to allow the design space to more appropriately match the tuned DMC values. Additional information concerning the constraints placed on the design space for each τ and σ is presented in section 6.3.2. The size of the population of quadruplets is set to 10 ($n = 10$); therefore,

there are 40 members in the design space. Fifty intervals are used for the Riemann sum calculations shown in equations (6.5) through (6.7), i.e., $m = 50$. The population size and number of Riemann intervals are changeable parameters.

6.3.1 Implementation

The implementation of GMC in GEODE is very straightforward. The previous implementation of XYZ DMC is left untouched and the part of Figure 6.1 inside the dashed lines is added to GEODE. All of the GMC processes take place just after the time update of the state and just prior to the formulation of the state transition and process noise covariance matrices.

6.3.2 GMC Tuning

Although trial and error tuning is not supposed to be required in GMC [9], GMC results improve dramatically if the range of values allowed for each member of the design space is tightly constrained around the tuned DMC values. This “bracketing” of the design space is carried out when the binary strings are converted to real numbers. The values chosen to bracket the design space for both the GPS/MET data with high rate GPS clocks applied and SA free TOPEX data are shown in Table 6.1. Table 6.1 also shows the best-tuned DMC values.

Scaling of the Riemann sums is also performed to keep the genetic measurement residuals within reasonable values. Scaling of the Riemann sums is performed in a very straightforward and logical manner. Once accomplished, the

Riemann sum scaling values are used for all data sets processed with GEODE.

The δx , δy , and δz Riemann sums are scaled (multiplied) by $1e6$ and the δb and

the δb_{dot} sums are scaled by 100.

Table 6.1 – GMC Design Space Bracketing

Data Set	Best DMC Value	Lower Bound	Upper Bound
4 Feb 1997 GPS/MET with High Rate GPS Clock Estimates			
τ	0.03	0.001	0.05
σ_u	0.0001	0.00005	0.00015
σ_b	5.9	0.001	8.0
$\sigma_{b_{dot}}$	0.09	0.01	0.4
5 May 2000 TOPEX			
τ	0.01	0.001	0.05
σ_u	0.0001	0.00005	0.00015
σ_b	0.01	0.001	8.0
$\sigma_{b_{dot}}$	0.2	0.01	0.4

6.3.3 GMC in GEODE Results

The application of the GA in GMC necessitates the use of a significant quantity of random numbers. GMC relies on random numbers for decisions in reproduction, crossover and mutation as well as in the solution of the stochastic integrals using Riemann sums. Since the generation of random numbers depends on an initial “seed,” the results attained with GMC change whenever a different random number seed is used. Therefore, to gauge GMC’s performance against DMC, statistical hypothesis testing is implemented. Hypothesis testing is a procedure where the mean of a population can be compared against a specified value [53]. In this case, the position RIC RMS and RSS values achieved using

DMC and JPL high rate GPS clock estimates (GPS/MET data) are compared to the results of 30 similar GMC runs. The sample size of 30 runs is chosen to satisfy the Central Limit Theorem. The Central Limit Theorem states that if the sample size n is large ($n \geq 30$), the sampling distribution of the sample mean will be approximately normal, even if the probability distribution of the population is unknown [53]. GEODE is run using GMC 30 times with *random* random number seeds. The radial, in-track, cross-track position errors from the 30 runs are used in the hypothesis testing.

The hypothesis testing procedure as shown in [53] is set up below to compare GMC applied to the GPS/MET data with high rate GPS clock estimates against GEODE's original process noise formulation with high rate GPS clock estimates:

1. The parameter of interest is the mean of the position RSS of the 30 GMC runs, referred to as μ .
2. The null hypothesis is $H_0: \mu = 7.60$ m (3D position RSS of the original process noise implementation in GEODE)
3. The alternative hypothesis is $H_1: \mu < 7.60$ m (reject H_0 if the mean of the position RSS of the GMC runs is less than 7.60 m)
4. The type I error probability (the probability of rejecting the null hypothesis even when it is true) is set at $\alpha = 0.0001$.

5. The test statistic is
$$t_0 = \frac{\bar{x} - \mu_0}{s / \sqrt{n}} \quad (6.18)$$

6. Reject H_0 if $t_0 < t_{0.0001, 29} = 4.254$

7. Computations: Since $\bar{x} = 6.13$ m (sample mean), $s = 0.317$ (sample standard deviation), $\mu_0 = 7.60$ m and $n = 30$,

$$t_0 = \frac{6.13 - 7.6}{0.317 / \sqrt{30}} = -28.79 \quad (6.19)$$

8. Conclusions: Since $t_0 = -28.79 < 4.254$, we reject H_0 and conclude, at the 0.0001 significance level, the mean of the GMC position RSS is lower than the DMC position RSS. In other words, there is a 99.99% probability GMC produces a lower 3D position RSS than DMC.

Similar hypothesis tests are performed for the radial, in-track and cross-track RMS values with the result that, at the 0.0001 significance level, GMC produces lower radial and in-track errors than GEODE's original implementation. The original implementation performs better than GMC in the cross-track direction. Figure 6.2 shows a plot of mean GMC results and the original process noise implementation in GEODE with the JPL high rate GPS clock estimates applied. As reflected in the hypothesis testing mentioned previously, the plots in Figure 6.2 show that GMC significantly outperforms the original process noise implementation in GEODE in the radial and in-track directions. GMC also provides a less biased estimate in the in-track direction. Table 6.2 shows statistics of the results using the original version of GEODE, XYZ DMC in GEODE and GMC in GEODE when the JPL high rate GPS clock estimates are applied.

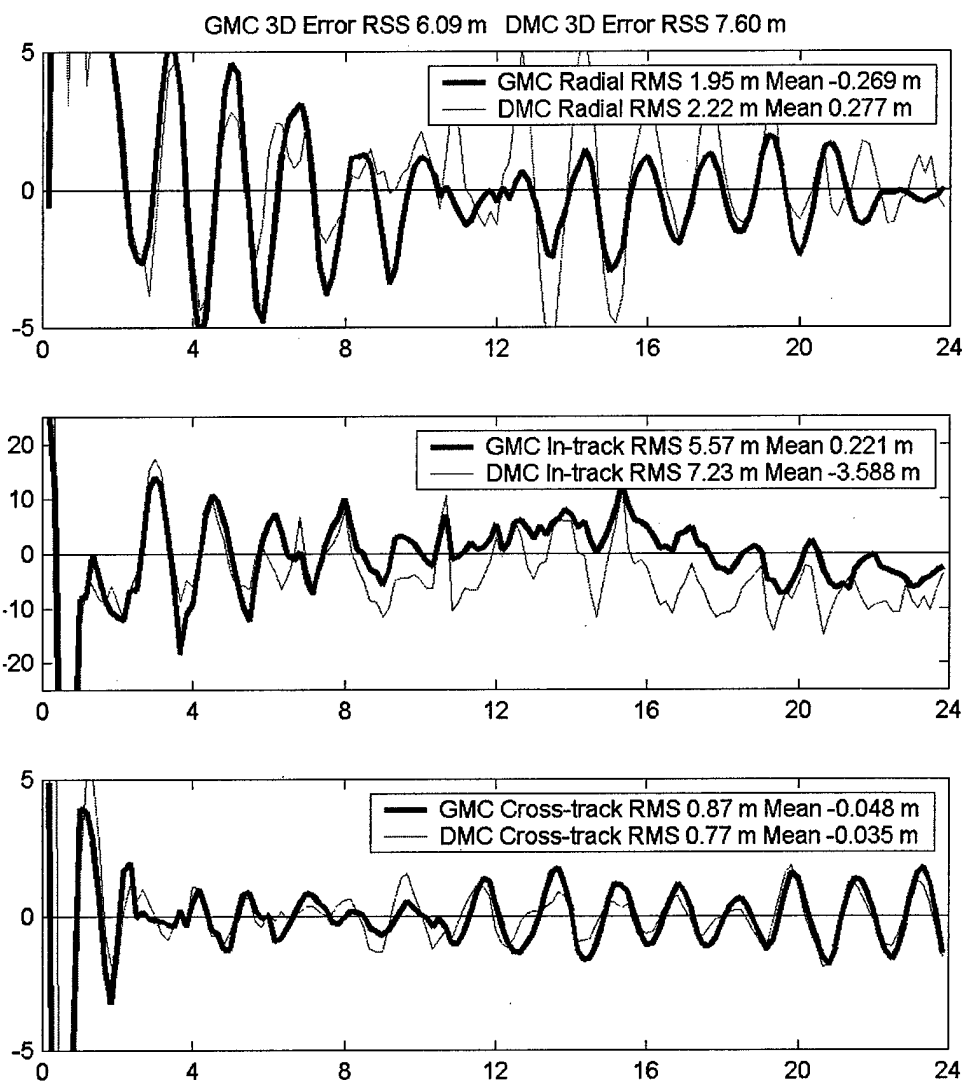


Figure 6.2 – GPS/MET High Rate GPS Clock GMC/DMC Comparison

Table 6.2 - GEODE GMC Results Comparison Using High Rate Clock Estimates to Correct for SA

4 Feb 1997 GPS/MET	Mean of Error (m)			RMS Error of Filter Compared to Truth (m)			
Scheme	R	I	C	R	I	C	3D
Original single	0.28	-3.59	-0.04	2.22	7.23	0.77	7.60
XYZ DMC single	-0.21	-0.52	-0.05	2.01	5.94	0.89	6.33
XYZ GMC single*	-0.28	0.42	-0.6	1.92	5.56	0.81	6.13

* Mean values for 30 runs

The mean τ and σ values chosen by GMC over the 30 runs are different than the optimal values found with DMC. Figure 6.3 shows plots of the mean DMC parameters determined with GMC over the 30 runs. The horizontal lines are the bracket values shown in Table 6.1. The upper bracket value for σ_b is off the plot. The mean values for τ , σ_u , and σ_b are close to the tuned DMC values. The mean value for σ_b is quite different and indicates that additional accuracy/precision gains may be attained with further DMC tuning.

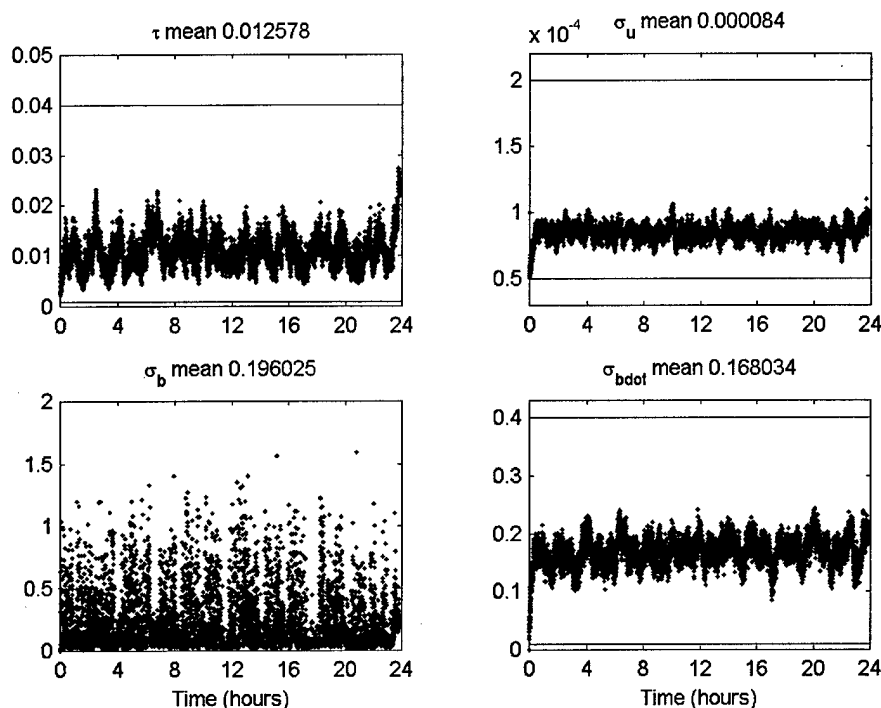


Figure 6.3 – GPS/MET Mean DMC Parameters from GMC

GEODE with GMC is also used to process the SA free TOPEX data. The mean results from the thirty GMC TOPEX runs are shown in Table 5.8 for comparison with the original version of GEODE and XYZ DMC in GEODE. Hypothesis testing results indicate that with 99.99% certainty, the means of the GMC RSS results are smaller than original GEODE. Hypothesis tests also indicate that GMC improves the radial and in-track position estimates, with 99.99% certainty. Again, the original GEODE implementation performed nearly the same as GMC in the cross-track direction. Figure 6.4 shows plots of the original GEODE implementation and mean GMC results in the radial, in-track

and cross-track directions. In the radial and cross-track directions the GMC results are nearly exactly the same as original GEODE results.

Table 6.3 - SA Free TOPEX GMC Results

5 May 2000 TOPEX	Mean of Error (m)			RMS Error of Filter Compared to Truth (m)			
Scheme	R	I	C	R	I	C	3D
Original Single	0.21	-0.04	0.01	0.35	1.06	0.44	1.20
XYZ DMC Single	0.19	-0.03	0.02	0.33	0.91	0.45	1.07
XYZ GMC Single*	0.19	-0.10	0.02	0.34	0.92	0.45	1.08

* Mean values for 30 runs

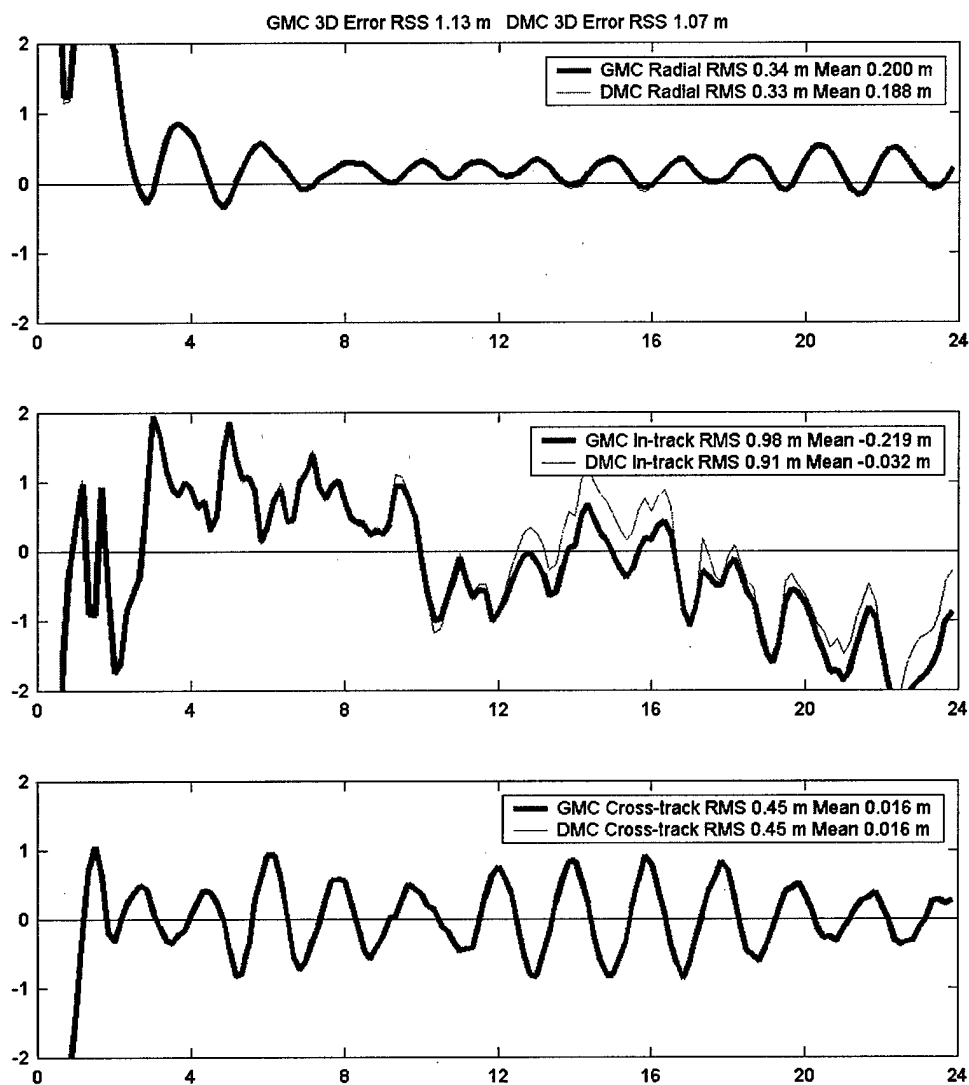


Figure 6.4 - TOPEX GMC/DMC Comparison

Figure 6.5 shows plots of the mean DMC parameters produced by GMC. In this case only the mean value of τ is significantly different from the best-tuned DMC value. Another interesting aspect of the plot is the spikes just after hours 8 and 16. The cause of the spikes is not known.

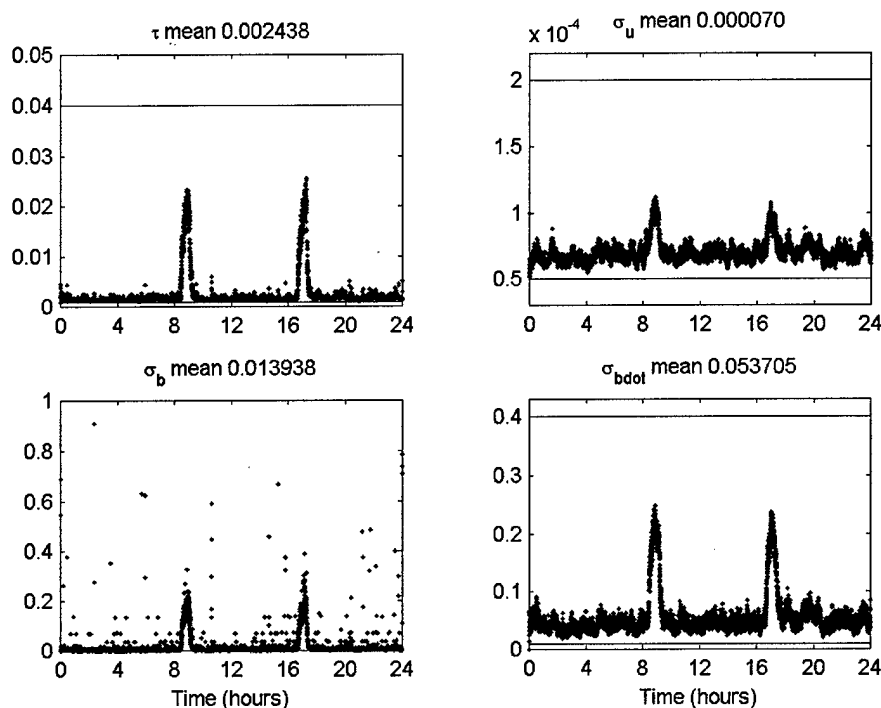


Figure 6.5 – TOPEX Mean DMC Parameters from GMC

The computational cost of using GMC to estimate the XYZ DMC parameters is significant. Run time increases by 86% when GMC is used instead of XYZ DMC. While the 86% increase is significant, the overall run time when processing 24 hours of data for GEODE with GMC is only 90-seconds on a 450 MHz Pentium II with 128 MB of RAM. Also, the 90-second execution time includes a significant amount of file i/o (reading in GPS observations, GPS ephemerides and POE and writing out state estimates, covariance matrices, error estimates and the Kalman gain).

6.4 Summary

In this chapter the Genetic Algorithm (GA) as applied to satellite orbit determination in the form of Genetic Model Compensation (GMC) is presented as an alternative to the DMC tuning process. While GMC does not necessarily improve GEODE's accuracy/precision compared to DMC, it does provide improvement compared to the original process noise implementation in GEODE. GMC also reduces the burden associated with DMC tuning. GMC does introduce a significant computational burden, however, it is not so significant that it prohibits GMC from potential deployment in a real-time satellite OD scenario. GMC is applied here with XYZ DMC but GMC could be extended to estimate RIC parameters associated with RIC DMC.

CHAPTER 7

Summary, Contributions, Future Work, and Conclusion

7.1 Summary

The differences between post-processing and real-time satellite orbit determination systems are presented in Chapter 1. Details regarding JPL's GOA-II, NRL's OCEAN and VMSI's MicroCosm® software suites are provided as examples of post-processing systems. Real-time GIPSY and an unnamed system from the University of Nottingham are described as real-time examples. The main differences between post-processing and real-time systems (with SA off) as stated in Chapter 1 are:

- Post-processing systems can use the best/largest gravity models available while real-time systems must use truncated models
- Post-processing systems estimate GPS ephemerides along with the satellite state or use precise GPS ephemerides while real-time systems use broadcast GPS ephemerides
- Post-processing systems use sophisticated ionospheric estimation models while real-time systems typically ignore ionospheric errors
- Post-processing systems use batch or batch sequential processors while real-time systems use EKF's

Chapter 2 includes a description of the OrbView-1 spacecraft and its secondary payload GPS/MET. Chapter 2 also provides a detailed description of

GEODE, details concerning the optimization of GEODE, a Lagrangian interpolation scheme applied to precise GPS ephemerides and a method for partially removing the effects of SA on the GPS/MET GPS observations. Baseline values of GEODE's performance when processing GPS/MET and T/P data are also established in Chapter 2. See Table 7.1.

Chapter 3 outlines the effect on accuracy of changing the degree and order of the gravity model used in propagating satellite ephemeris and in real-time satellite OD (see Table 7.1). It is important to again note that GEODE utilizes an EKF. Therefore, the OD results presented in Chapter 3 cannot be used to predict the effect of using truncated gravity models in a batch processing scenario.

At the GPS/MET altitude and inclination, there is a 4.5 m accuracy gain when a 30x30 truncation of the JGM-2 gravity model is used for a 24-hour propagation instead of a 20x20 truncation (both compared to a 70x70 model). However, there is only a 1 m 3D RSS improvement in GEODE's OD estimate when a 30x30 truncation is used as compared to a 20x20 truncation. While the OD accuracy difference is small, the computation time required for processing one day of GPS/MET observations is 11% less for the 20x20 truncation compared to the 30x30 truncation. Chapter 3 also shows there is no advantage to using different models (JGM-3 or EGM-96) than JGM-2 and that there is only a minor OD accuracy/precision improvement when truncations larger than 30x30 are used.

To reduce OD computational burden while maintaining accuracy/precision the Gravity Acceleration Approximation Function (GAAF) is also introduced in

Chapter 3. At the GPS/MET altitude and inclination it is found that a 20 km altitude range could be fit with 1st order polynomials to describe pseudocenter coefficients at various latitudes and longitudes. The 20 km - 1st order polynomial GAAF implementation requires only 1.88 MB of memory compared to the 4.9 MB required by the original implementation in [50]. 24-hour ephemeris propagation and GEODE OD results confirm that accuracy/precision are maintained when GAAF is used and that the computational burden of GAAF is equivalent to that of a 5x5 gravity model truncation.

Measurement errors due to the ionosphere are the topic of Chapter 4. The ionosphere is described and the Differenced Range Versus Integrated Doppler (DRVID) method of estimating ionospheric measurement errors is presented. Measurement errors from the ionosphere are highest when satellites are in sunlight and for GPS/MET were sometimes as high as 50 m in 1997. The RMS of the dual frequency ionospheric corrections for the 4 Feb 1997 GPS/MET data is 2.49 m (2.75 m in sunlight/1.84 m in darkness). Application of dual frequency ionospheric corrections to the GPS/MET data only marginally improved the 3D position RSS and introduced an in-track bias. The reason for the marginal RSS improvement is probably due to the dominating effects of SA errors.

DRVID utilizes the difference in the way the pseudorange and phase measurements are affected by the ionosphere. Since the ionosphere advances phase and delays range measurements, a linear combination of phase and range measurements can remove ionospheric errors to first order. Unfortunately, in

using the phase measurement, an unknown integer ambiguity is introduced. Since estimation of phase integer ambiguities in real-time is probably unrealistic and the level of interaction required to use an accurate model to predict the initial measurement error due to the ionosphere is probably unacceptable in real-time OD systems, the zero bias DRVID method is proposed. Zero bias DRVID takes advantage of the fact that the measurement error due to the ionosphere is smallest when the GPS satellite is at its highest elevation angle with respect to the user satellite. Since the minimum measurement error point can be easily determined in real-time, the measurement error due to the ionosphere at this point is assumed to be zero. All measurements prior to the maximum elevation point, in a given tracking arc, are not corrected with DRVID while all measurements taken after the maximum elevation point are corrected with DRVID. DRVID introduces a 12.1% computational burden increase to GEODE but improves the 3D position RSS when applied to the four different GPS/MET cases and to the T/P data as seen in Table 7.2.

Dynamic Model Compensation (DMC) is developed and applied in Chapter 5. DMC provides process noise formulation and estimation of accelerations not accounted for in GEODE's dynamic model. DMC is applied to two Matlab simulations with the result that the 3D position error RSS of the filtered solution compared to truth is significantly improved when XYZ DMC is applied and improved further when RIC DMC is applied. However, when the observation geometry is improved in the second simulation, RIC DMC does not

provide as significant an improvement as in the first simulation (when observation geometry is not as good).

XYZ DMC also improves GEODE's position estimates. DMC parameter tuning results are presented and it is shown that XYZ DMC improves GEODE's 3D position error RSS by 23.0% over GEODE's original process noise formulation on GPS/MET data when high rate GPS clock estimates are not applied, 16.7% when high rate GPS clock estimates are applied and 10.0% on SA free T/P data. RIC DMC further improves GEODE's position estimates by 3% over XYZ DMC. XYZ DMC does not increase GEODE's computational burden while RIC DMC increases the burden by roughly 1%.

Tuning of the DMC time correlation coefficient (τ) and the standard deviation of the forcing noise (σ) can be tedious and time consuming. Also, the pre-mission tuning process may yield optimum values that may not be optimum during the mission when "real" data is processed. Genetic Model Compensation (GMC) is described and GMC GEODE implementation results are presented in Chapter 6. GMC is an application of a Genetic Algorithm (GA) to optimize the τ and σ s used by DMC. GA's operate on strings of binary numbers and use random processes to arrive at optimum values through reproduction, crossover and mutation.

Since random numbers drive GMC, hypothesis testing is explained and applied to determining, with known probability, if GMC improves GEODE's position estimates compared to GEODE's original process noise implementation.

Thirty GEODE runs are performed using GMC on the GPS/MET data with high rate GPS clock estimates applied. The results of the 30 GMC runs are compared against results from original GEODE. Hypothesis testing concludes, with 99.99% probability, that GMC improves GEODE's position estimates. In fact, the mean GMC 3D position error RSS is 19.3% lower than original GEODE. Thirty GMC GEODE runs are also performed on the SA free T/P data. Hypothesis testing again concludes, with 99.99% probability, that GMC GEODE provides better position estimates than original GEODE. In this case, the GMC GEODE 3D position RSS is 10.0 % lower than original GEODE.

The improvements gained through the application of GMC do not come without computational cost. GMC increases GEODE's computational burden by approximately 86% but GEODE's relatively small overall burden, even with GMC, does not prohibit its use in a real-time OD system.

Table 7.1 – Chapter 2 through Chapter 4 Results Summary

Chapter 2	Error Mean (m)			Error RMS (m)			
	R	I	C	R	I	C	3D
GPSMET orig single	0.55	-0.99	-0.10	2.74	10.24	2.15	10.81
GPSMET orig dual	0.11	2.04	-0.11	2.48	9.68	2.12	10.21
GPSMET orig single PE	0.58	-1.05	-0.09	2.99	10.11	1.97	10.73
GPSMET orig dual PE	0.11	2.01	-0.11	2.48	9.22	2.03	9.76
GPSMET orig single hr	0.28	-3.59	-0.04	2.22	7.23	0.77	7.60
GPSMET orig dual hr	-0.08	-1.38	-0.04	2.10	6.14	0.86	6.55
GPSMET orig single hr PE	0.30	-3.56	-0.03	2.31	6.95	0.74	7.36
GPSMET orig dual hr PE	-0.06	-1.35	-0.03	1.91	5.43	1.04	5.85
T/P orig single	0.21	-0.04	0.01	0.35	1.06	0.44	1.20
T/P orig single PE	0.22	-0.16	0.00	0.34	0.97	0.31	1.08
Chapter 3							
GPSMET orig single							
JGM-2 05x05 (OD)	1.71	-5.57	-0.06	25.42	53.87	29.42	66.43
JGM-2 10x10	0.54	-2.03	0.62	7.66	18.16	7.15	20.96
JGM-2 20x20	0.52	-0.97	0.02	3.12	11.05	2.93	11.85
JGM-2 22x22	0.66	-1.14	0.05	2.90	10.53	2.26	11.15
JGM-2 24x24	0.58	-0.91	-0.07	2.77	10.56	2.56	11.21
JGM-2 25x25	0.58	-0.88	-0.07	2.78	10.36	2.03	10.92
JGM-2 26x26	0.60	-1.02	-0.06	2.69	10.18	2.06	10.73
JGM-2 27x27	0.57	-0.97	-0.06	2.72	10.26	2.13	10.82
JGM-2 28x28	0.56	-0.99	-0.06	2.74	10.31	2.26	10.91
JGM-2 30x30	0.55	-0.99	-0.10	2.74	10.24	2.15	10.81
JGM-2 40x40	0.52	-0.90	-0.07	2.71	10.14	2.29	10.75
JGM-2 50x50	0.52	-0.88	-0.05	2.71	10.12	2.41	10.75
JGM-2 70x70	0.52	-0.88	-0.05	2.70	10.11	2.38	10.74
GAAF	0.52	-0.88	-0.05	2.71	10.11	2.38	10.74
EGM-96 30x30	0.55	-0.97	-0.11	2.75	10.25	2.18	10.83
JGM-3 30x30	0.52	-0.91	-0.11	2.74	10.24	1.98	10.78
Chapter 4							
GPSMET orig DRVID	0.22	-0.86	-0.12	2.49	10.00	2.24	10.55
GPSMET orig DRVID PE	0.24	-0.92	-0.11	2.59	9.68	2.08	10.24
GPSMET orig DRVID hr	-0.03	-3.54	-0.04	1.97	6.95	0.90	7.28
GPSMET orig DRVID hr PE	0.00	-3.57	-0.04	1.92	6.46	0.81	6.78
T/P DRVID single	0.20	0.01	0.01	0.35	1.02	0.45	1.17

Table 7.2 – Chapter 5 and Chapter 6 Results Summary

Chapter 5	Error Mean (m)			Error RMS (m)			
XYZ DMC	R	I	C	R	I	C	3D
GPSMET DMC single	-0.18	3.08	-0.14	1.74	7.77	2.41	8.32
GPSMET DMC dual	-0.34	5.07	-0.14	1.84	8.44	2.38	8.96
GPSMET DMC DRVID	-0.30	1.94	-0.14	1.93	7.07	2.56	7.76
GPSMET DMC single PE	-0.16	3.09	-0.12	2.00	7.51	2.19	8.08
GPSMET DMC dual PE	-0.33	5.07	-0.12	1.76	7.92	2.22	8.41
GPSMET DMC DRVID PE	-0.26	2.11	-0.12	1.92	6.92	2.15	7.50
GPSMET DMC single hr	-0.21	-0.52	-0.05	2.01	5.94	0.89	6.33
GPSMET DMC dual hr	-0.35	0.87	-0.05	2.11	5.97	0.98	6.41
GPSMET DMC DRVID hr	-0.31	-1.19	-0.06	1.95	5.70	1.03	6.11
GPSMET DMC single hr PE	-0.19	-0.41	-0.04	2.00	5.23	0.84	5.66
GPSMET DMC dual hr PE	-0.33	0.98	-0.04	1.84	4.92	1.11	5.37
GPSMET DMC DRVID hr PE	-0.30	-1.22	-0.05	1.83	4.82	1.00	5.25
T/P DMC single	0.19	-0.03	0.02	0.33	0.91	0.45	1.07
T/P DMC DRVID	0.19	-0.20	0.02	0.34	0.89	0.46	1.06
T/P DMC single PE	0.20	-0.17	0.01	0.33	0.84	0.33	0.96
T/P DMC DRVID PE	0.20	-0.34	0.01	0.33	0.85	0.35	0.98
RIC DMC							
GPSMET RIC DMC single	-0.17	2.89	-0.17	1.70	7.55	2.30	8.07
GPSMET RIC DMC DRVID	-0.29	1.75	-0.17	1.94	6.92	2.26	7.53
Chapter 6							
GPSMET GMC single hr*	-0.28	0.42	-0.6	1.92	5.56	0.81	6.13
T/P GMC*	0.19	-0.10	0.02	0.34	0.92	0.45	1.08

* Mean value for 30 runs

Results for all GPS/MET and T/P GEODE runs, as described in Chapter 2 through Chapter 6, are presented in Table 7.1 and Table 7.2. The following definitions also apply to Table 7.1 and Table 7.2:

orig = Original GEODE process noise formulation
 single = No ionospheric correction applied
 PE = Precise GPS ephemerides used
 hr = High rate GPS clock estimates applied to remove SA

7.2 Research Contributions

This dissertation provides an extended evaluation of real-time satellite OD using GPS and offers several suggestions to improve the state-of-the-art. The affects on real-time OD of using precise GPS ephemerides rather than those broadcast, using dual-frequency ionospheric corrections instead of no corrections, using SA free GPS measurements, and using various gravity models and truncated gravity models are characterized in terms of accuracy/precision and computational burden. Also in this dissertation, GAAF is implemented in propagation and OD scenarios, zero bias DRVID is developed and implemented, DMC is implemented and extended to estimate accelerations in RIC coordinates and GMC is employed to reduce the burden associated with tuning DMC.

7.3 Recommendations for Future Work

7.3.1 GAAF Coefficient Estimation

Sophisticated OD filters can simultaneously estimate spherical harmonic gravitational coefficients along with the satellite state. It is recommended that the capability of estimating GAAF coefficients in an OD scheme be investigated. The advantage of estimating GAAF coefficients over spherical harmonic gravitational coefficients is that in GAAF, information from each measurement will only affect those coefficients whose latitude and longitude are near where the

measurement is taken. In estimating spherical harmonic gravitational coefficients the processing of each measurement affects all coefficients used in the expansion.

7.3.2 GMC RIC Extension

GMC has only been applied to XYZ DMC. An extension of GMC to RIC DMC is recommended where the RIC τ s and σ s ($\tau_R, \tau_I, \tau_C, \sigma_R, \sigma_I, \sigma_C$) are optimized. In this case, instead of optimizing quadruplets, GMC would optimize octuples. The Riemann summations would stay the same as the XYZ GMC implementation, only the τ s and σ s would be different for each of the three position summations. Additional reproduction, crossover and mutation procedures would also need to be added to take into account the extra four members included in each individual.

7.3.3 Automated DMC Tuning With the Genetic Algorithm

Another promising application of a GA is tuning of DMC parameters outside of GEODE. Here RMS and RSS statistics would be used to gauge GEODE's performance. GEODE would be run using all individuals from a given generation and the RMS and RSS statistics would be used to compute the merit of each individual. Again, each individual is made up of a different set of τ s and σ s. Then the GA procedures of reproduction, crossover and mutation would be performed based on the merit of each individual and the next generation would be used in GEODE again. This process would be repeated until the GA converges

on an optimal set of τ s and σ s. Figure 7.1 shows a diagram of the proposed application of the GA to DMC tuning.

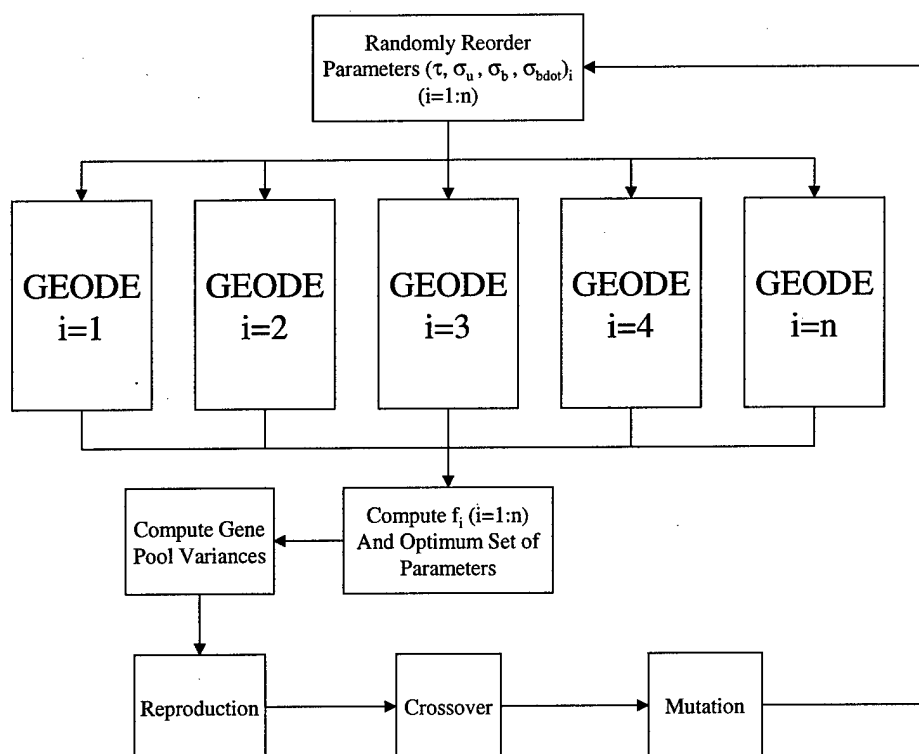


Figure 7.1 – GA for DMC Tuning

7.3.4 GPS Point Solution Measurement

There are several satellite missions (QuikScat and Picasso) where GPS receivers are flown but raw GPS pseudorange and phase measurements are not available in real-time and in the case of QuikScat not available for post-processing. In both of these cases more accurate satellite position knowledge is required than can be determined by the GPS receiver's point solution. Therefore, a modification to GEODE is suggested where GEODE would use the GPS

receiver's point solution (both position and velocity) as measurements for the filter. The modifications to GEODE would include removing the GPS receiver clock bias and clock bias drift rate terms from the state, reformulation of the state transition matrix and observation state relationship, and declaration of additional variable to support the input of the receiver's point solution.

7.4 Conclusion

A new era in real-time satellite orbit determination began when SA was turned off on 2 May 2000. Meter and sub-meter 3D position accuracy is now available in real-time on board a satellite. GSFC's GEODE is a powerful real-time satellite OD software suite that goes a long way to make meter level real-time OD possible. Part of GEODE's power is realized through GSFC's provision of GEODE source code. GEODE's modular nature and the relative ease of modification make it flexible and highly usable software.

This dissertation offers several suggested modifications to GEODE to increase its accuracy/precision and autonomy and to decrease its computational burden. Accuracy/precision improvements are demonstrated with the application of DRVID, DMC and GMC but each increases GEODE's computational burden. GMC improves GEODE's autonomy by allowing the on board filter to adapt to changes in the dynamic environment but imposes a significant computational burden. While GAAF reduces computational burden, it does not improve or degrade GEODE's accuracy/precision. Each suggested improvement provides its

own advantages and disadvantages and therefore, the implementation of each improvement must be balanced against mission requirements and hardware capabilities.

REFERENCES

- [1] Truong, S.H., K.R. Hartman, D.A. Weidow, D.L. Berry, D.H. Oza, A.C. Long, and T. Lee, *Modular Software for Spacecraft Navigation Using the Global Positioning System (GPS)*, A97-20826 04-32, Proceedings of ION GPS-96, Kansas City, MO, 17-20 September 1996.
- [2] Ashkenazi, V., W. Chen, C.J. Hill, T. Moore, D. Stanton, D. Fortune, and N. Shave, *Real-Time Autonomous Orbit Determination of LEO Satellites Using GPS*, Proceedings of ION GPS-97, Kansas City, MO, September 1997.
- [3] Gold, K., W. Bertiger, T. Yunck, S. Wu, R. Muellerschoen, G. Born, and K. Larson, *A Study of Real Time Orbit Determination for the Extreme Ultraviolet Explorer*, A95-22921 05-32, Navigating the Earth and Beyond; Proceedings of the Institute of Navigation's 1994 National Technical Meeting, San Diego, CA, 24-26 January 1994.
- [4] Hart, R.C., K.R. Hartman, A.C. Long, T. Lee, and D.H. Oza, *Global Positioning System (GPS) Enhanced Orbit Determination Experiment (GEODE) on the Small Satellite Technology Initiative (SSTI) Lewis spacecraft*, A97-20826 04-32, Proceedings of ION GPS-96, Kansas City, MO, 17-20 September 1996.
- [5] Lichten, S., R. Mullerschoen, J. Srinivasan, U. Lindqwister, T. Munson, S.-C. Wu, B. Haines, J. Guinn, and L. Young, *An Automated Low-Earth Orbit Determination System with High Accuracy Real-time Capability*, A95-41501 11-32, Proceedings of ION GPS-95, Anaheim, CA, 18-20 January 1995.
- [6] Pradines, D., J.P. Berthias, C. Jayles, and F. Nouel, *Real-time orbit determination with DORIS on-board of SPOT 4*, IAF, International Astronautical Congress, 44th, Graz, Austria, Oct. 16-22.
- [7] Spardley, L.H., *Real-time Differential GPS with 20 to 50 cm Accuracies*, A94-20628 04-32, Evolution Through Integration of Current and Emerging Systems; Proceedings of the Institute of Navigation's 1993 National Technical Meeting, San Francisco, CA, 20-22 January 1993.

- [8] Tu, K.-C., *Precise Real-time Orbit Determination for Application to GPS Differential Positioning*, Ph.D. Thesis, Aerospace Engineering Sciences, University of Colorado, Boulder, Colorado, 1990.
- [9] Cruickshank, D.R., *Genetic Model Compensation: Theory and Applications*, Ph.D. Thesis, Aerospace Engineering Sciences, University of Colorado, Boulder, CO, 1998.
- [10] Kaplan, E.D., *Understanding GPS : Principles and Applications*, Artech House, Boston, MA, 1996.
- [11] Lichten, S.M., Y. Bar-Sever, and W.I. Bertiger, *GIPSY-OASIS II: A High Precision GPS Data Processing System and General Satellite Analysis Tool*, Technical Report, Jet Propulsion Laboratory, Pasadena, CA, 1995.
- [12] Soyka, M.T., J.W. Middour, P.W. Binning, H. Pickard, and J. Fein, *The Naval Research Laboratory's Orbit/Covariance Estimation and Analysis Software: OCEAN*, A98-23960 05-12, *Advances in the Astronautical Sciences*, vol. 97, pt. 2, pp. 1567-1586, American Astronautical Society, 1997.
- [13] Hurst, K., *GIPSY - OASIS II*, 26 August 1998, <http://www.unavco.ucar.edu/processing/gipsy/>, June 2000
- [14] Wu, J.T., *Elimination of Clock Errors in a GPS Based Tracking System*, AIAA 84-2052, Proceedings of the AIAA/AAS Astrodynamics Conference, Seattle, WA, 20-22 August 1984.
- [15] Lough, M.F., B.J. Haines, S.M. Lichten, M.R. J., and Y. Vigue-Rodi, *Precise Orbit Determination for Low-Earth Orbiting Satellites using GPS Data: Recent Advances*, Proceedings of ION GPS-98, Denver, CO, 1-3 June 1998.
- [16] Bertiger, W., B. Haines, D. Kuang, M. Lough, S. Lichten, R.J. Muellerschoen, Y. Vigue, and S. Wu, *Precise Real-time Low Earth Orbiter Navigation with GPS*, Proceedings of the 11th International Technical Meeting of the Satellite Division of the Institute of Navigation, ION GPS-98, Nashville, TN, 15-18 September 1998.
- [17] Hofmann-Wellenhof, B., H. Lichtenegger, and J. Collins, *Global Positioning System: Theory and Practice*, Springer-Verlag, Wien, New York, 1993.
- [18] Martin, T., *MicroCosm System Description*, Van Martin Systems Inc., September 1997.

- [19] Schreiner, W.S., D.C. Hunt, C. Rocken, and S. Sokolovskiy, *Precise GPS Data Processing for the GPS/MET Radio Occultation Mission at UCAR*, Proceedings of the Institute of Navigation's National Technical Meeting: 'Navigation 2000', Long Beach, CA, 21-23 January 1998.
- [20] Collins, J.T. and R.T. Conger, *MANS - Autonomous Navigation and Orbit Control for Communications Satellites*, Proceedings of the 15th AIAA International Communications Satellite Systems Conference, San Diego, CA, 28 February - 3 March 1994.
- [21] Lopes, R.V. and H.K. Kuga, *ORBEST - A GPS Navigation Solution Algorithm Without DOP Analysis*, A97-35251 09-12, Proceedings of the AAS/AIAA Space Flight Mechanics Conference, Huntsville, AL, 10-12 February 1997.
- [22] Hart, R.C., S. Truong, A.C. Long, T. Lee, J. Chan, and D.H. Oza, *GPS Navigation Initiatives at Goddard Space Flight Center Flight Dynamics Division*, A97-35251 09-12, Proceedings of the AAS/AIAA Space Flight Mechanics Conference, Huntsville, AL, 10-12 February 1997.
- [23] Chen, W., University of Nottingham, Nottingham, UK, Personal Communication, 1998.
- [24] Zumberge, J.F. and W.I. Bertiger, *Ephemeris and Clock Navigation Message Accuracy, Global Positioning System: Theory and Applications*, vol. I, pp. 585-599, American Institute of Aeronautics and Astronautics, Washington D. C., 1996.
- [25] Hermann, B. and S. Malys, *Precise Absolute Navigation - An Evaluation of PPS Position Improvement*, A96-15026 02-17, Proceedings of the 8th International Technical Meeting of the Satellite Division of the Institute of Navigation; ION GPS-95, Palm Springs, CA, 12-15 September 1995.
- [26] Binning, P.W., *Satellite Orbit Determination Using GPS Pseudoranges Under SA*, A97-35251 09-12, Proceedings of the AAS/AIAA Space Flight Mechanics Conference, Huntsville, AL, 10-12 February 1997.
- [27] Smith, R.H., J.V. Langer, and W.A. Feess, *Direct Satellite Tracking Using GPS*, Proceedings of the Institute of Navigations 1994 National Technical Meeting, San Diego, CA, 24-26 January 1994.
- [28] Rim, H.J., B.E. Schutz, A.M. Abusali, and B.D. Tapley, *Effect of GPS Orbit Accuracy on GPS-determined Topex/Poseidon Orbit*, Proceedings of The 8th International Technical Meeting of the Satellite Division of the Institute of Navigation, Palm Springs, CA, 12-15 September 1995.

- [29] MacDoran, P.F. and W.L. Martin, *A First Principles Derivation of Differenced Range vs. Integrated Doppler (DRVID) Charged Particle Calibration Method*, JPL Space Programs Summary 37-62, Vol II, No. 4, Jet Propulsion Laboratory, Pasadena, CA, February 1970.
- [30] Yunck, T.P., S.C. Wu, J.T. Wu, and C.L. Thorton, *Precise Tracking of Remote Sensing Satellites With the GPS*, A90-26649, *IEEE Transactions on Geoscience and Remote Sensing*, 28, pp. 108-116, 1, 1990.
- [31] Schreiner, W.S., *Error Analysis of Real-time and Post-processed Orbit Determination for the Geosat Follow-on Altimetric Satellite using GPS Tracking*, Ph.D. Thesis, Aerospace Engineering Sciences, University of Colorado, Boulder, CO, 1993.
- [32] Cohen, C.E. and B.W. Parkinson, *Integer Ambiguity Resolution and the GPS Carrier for Spacecraft Attitude Determination*, A90-26649, *Advances in the Astronautical Sciences*, vol 92, pp. 107-118, 1992.
- [33] AGI, *AGI Spacecraft Digest for OrbView-1 Spacecraft*, 28 October 1998, <http://www.stk.com/resources/scdigest/>, June 2000
- [34] Hunt, D.C., *GPS/MET Preliminary Report*, <http://cosmic.cosmic.ucar.edu/gpsmet/over/septsumm1.html>, June 2000
- [35] Hart, R.C., A.C. Long, and T. Lee, *Autonomous Navigation of the SSTI/Lewis Spacecraft Using the Global Positioning System (GPS)*, A97-32176 08-18, Proceedings of The Flight Mechanics Symposium 1997, Greenbelt, MD, 19-21 May 1997.
- [36] TRW, *Small Spacecraft Technology Initiative (SSTI)*, 1998, <http://www.trw.com/seg/sats/SSTI.html>, June 2000
- [37] Lee, T. and A.C. Long, *GPS Enhanced Orbit Determination Experiment (GEODE) Mathematical Specifications Version 4*, CSC-96-932-05R0UD0, Goddard Space Flight Center, Flight Dynamics Division, Greenbelt, Maryland, January 1999.
- [38] Born, G.H., B.D. Tapley, and B.E. Schutz, *Satellite Orbit Determination: Fundamentals and Applications*, Department of Aerospace Engineering Sciences, University of Colorado, Boulder, CO, 2000.
- [39] Bierman, G.J., *Factorization Methods for Discrete Sequential Estimation*, Academic Press, New York, 1977.
- [40] Thornton, C.L., *Trinagular Covariance Factorizations for Kalman Filtering*, Jet Propulsion Laboratory, Pasadena, CA, 15 October 1976.

- [41] Maybeck, P.S., *Stochastic Models, Estimation and Control*, Academic Press, New York, 1979.
- [42] Wright, J., *Sequential Orbit Determination With Auto-Correlated Gravity Modeling Errors*, AIAA 80-0239R, *Journal of Guidance and Control*, vol 4, no. 3, pp. 304-309, May-June, 1981.
- [43] Klobuchar, J.A., *Ionospheric Effects on GPS, Global Positioning System: Theory and Applications*, vol. I, pp. 485-515, American Institute of Aeronautics and Astronautics, Washington D. C., 1996.
- [44] Yinger, C.H., W.A. Feess, R. Di Esposti, A. Chasko, B. Cosentino, D. Syse, B. Wilson, and B. Wheaton, *GPS Satellite Interfrequency Biases*, A00-18180 03-32, Proceedings of the Institute of Navigation's, 55th Annual Meeting, Cambridge, MA, 28-30 June 1999.
- [45] *The Astronomical Almanac for the Year 1998*, U.S. Government Printing Office / London H.M.S.O., Washington / London, 1998.
- [46] USNO, *What is Earth Orientation?*, 20 February 1998, <http://maia.usno.navy.mil/eo/whatiseop.html>, June 2000
- [47] Haines, B.J., Jet Propulsion Laboratory, Pasadena, CA, Personal Communication, 1999.
- [48] Stauch, J., Colorado Center for Astrodynamics Research, University of Colorado, Boulder, CO, Personal Communication, 2000.
- [49] Lundahl, J., Ball Aerospace Corporation, Boulder, CO, Personal Communication, 2000.
- [50] Hujsak, R.S., *Gravity Acceleration Approximation Functions*, A96-40059 11-12, *Advances in the Astronautical Sciences*, vol 93, pt. 1, pp. 335-349, 1996.
- [51] Bate, R.R., J.E. White, and D.D. Mueller, *Fundamentals of Astrodynamics*, Dover Publications, New York,, 1971.
- [52] Abramowitz, M. and I.A. Stegun, *Handbook of Mathematical Functions*, Dover Publications, New York, 1965.
- [53] Montgomery, D.C. and G.C. Runger, *Applied Statistics and Probability for Engineers*, John Wiley & Sons, New York, 1994.
- [54] Wells, D. and N. Beck, *Guide to GPS Positioning*, Canadian GPS Associates, Fredericton, New Brunswick, 1987.

- [55] Gold, K., G. Born, G. Davis, and J. Armstrong, *Final Report, Real Time GPS Orbit Determination Simulations with GIPSY-OASIS II.*, Colorado Center for Astrodynamics Research, Boulder, Colorado, 5 December 1997.
- [56] Gold, K., W. Bertiter, S. Wu, T. Yunck, R. Muellerschoen, and G. Born, *GPS Orbit Determination in the Presence of SA for EUVE*, A95-33201 08-17, Proceedings of the 7th International Technical Meeting of the Satellite Division of the Institute of Navigation, Salt Lake City, UT, 20-23 September 1994.
- [57] Meek, C., University of Colorado, Boulder, CO, Personal Communications, 2000.
- [58] MacDoran, P.F. and D.J. Spitzmesser, *Method and Apparatus for Deriving Pseudo Range from Earth Orbiting Satellites*, U.S. Patent No. 4,797,677 10 January 1989.
- [59] Gold, K., W. Bertiger, S. Wu, T. Yunck, R. Mullerschoen, and G. Born, *GPS Orbit Determination for the Extreme Ultraviolet Explorer, Navigation*, vol 41, no. 3, pp. 337-351, 0028-1522, 1994.
- [60] Yunck, T.P., *Coping With the Atmosphere and Ionosphere in Precise Satellite and Ground Positioning, Environmental Effects on Spacecraft Positioning and Trajectories*, pp. 1-16, 1993.
- [61] Kubitschek, D.G. and M.C. Meek, *Precision Orbit Determination (POD) System Specifications Report*, CCAR Technical Memorandum, Colorado Center for Astrodynamics Research, University of Colorado, Boulder, Colorado, 2000.
- [62] Wu, S.C., T.P. Yunck, and C.L. Thorton, *Reduced-Dynamic Technique for Precise Orbit Determination of Low Earth Satellites*, *Journal of Guidance, Control and Dynamics*, vol. 14, no. 1, pp. 24-30, 1991.
- [63] Ingram, D.S., *Orbit Determination in the Presence of Unmodeled Accelerations*, Ph.D. Thesis, Aerospace Engineering, University of Texas, Austin, TX, 1970.
- [64] Cruickshank, D.R., *Algorithms for Autonomous Satellite Navigation using GPS Measurements*, M.S. Thesis, Aerospace Engineering Sciences, University of Colorado, Boulder, CO, 1994.
- [65] Cruickshank, D.R. and G.H. Born, *A New Class of Adaptive, Extended Kalman Filter*, A96-40059 11-12, Proceedings of the 6th AAS/AIAA Spaceflight Mechanics Conference, Austin, TX, 12-15 February 1996.

- [66] Goldberg, D.E., *Genetic Algorithms in Search, Optimization, and Machine Learning*, Addison-Wesley, Massachusetts, 1989.
- [67] Beasley, D., D.R. Bull, and R.R. Martin, *An Overview of Genetic Algorithms: Part 1, Fundamentals*, *University Computing*, vol. 15, no. 2, pp. 58-69, 1993.